

DTIC FILE COPY

2

WRDC-TR-89-2056



**MODIFICATION AND IMPROVEMENT OF SOFTWARE FOR
MODELING MULTIDIMENSIONAL REACTING FUEL FLOWS**

Dr. David E. Keyes
Mr. Dennis J. Philbin
Dr. Mitchell D. Smooke

Scientific Computing Associates, Inc.
246 Church Street, Suite 307
New Haven, Connecticut 06510

July 1989

DTIC
ELECTE
FEB 08 1990
S D D
CD

Final Report for Period November 1986 - January 1989

Approved for public release; distribution is unlimited.

AERO PROPULSION AND POWER LABORATORY
WRIGHT RESEARCH AND DEVELOPMENT CENTER
AIR FORCE SYSTEMS COMMAND
WRIGHT-PATTERSON AIR FORCE BASE, OHIO 45433-6563

90 02 07 064

NOTICE

When Government drawings, specifications, or other data are used for any purpose other than in connection with a definitely related Government procurement operation, the United States Government thereby incurs no responsibility nor any obligation whatsoever; and the fact that the government may have formulated, furnished, or in any way supplied the said drawings, specifications, or other data, is not to be regarded by implication or otherwise as in any manner licensing the holder or any other person or corporation, or conveying any rights or permission to manufacture, use, or sell any patented invention that may in any way be related thereto.

This report has been reviewed by the Office of Public Affairs (ASD/PA) and is releasable to the National Technical Information Service (NTIS). At NTIS, it will be available to the general public, including foreign nations.

This technical report has been reviewed and is approved for publication.



JEFFREY S. STUTRUD
Fuels Branch
Fuels and Lubrication Division
Aero Propulsion and Power Laboratory



CHARLES L. DELANEY, CHIEF
Fuels Branch
Fuels and Lubrication Division
Aero Propulsion and Power Laboratory

FOR THE COMMANDER



BENITO P. BOTTERI, CHIEF
Fuels and Lubrication Division
Aero Propulsion and Power Laboratory

If your address has changed, if you wish to be removed from our mailing list, or if the addressee is no longer employed by your organization, please notify WRDC/POSF, Wright-Patterson AFB, Ohio 45433-6563 to help us maintain a current mailing list .

Copies of this report should not be returned unless return is required by security considerations, contractual obligations, or notice on a specific document.

Unclassified

SECURITY CLASSIFICATION OF THIS PAGE

REPORT DOCUMENTATION PAGE

Form Approved
OMB No. 0704-0188

1a. REPORT SECURITY CLASSIFICATION Unclassified		1b. RESTRICTIVE MARKINGS	
2a. SECURITY CLASSIFICATION AUTHORITY		3. DISTRIBUTION / AVAILABILITY OF REPORT	
2b. DECLASSIFICATION / DOWNGRADING SCHEDULE		Approved for public release, distribution is unlimited.	
4. PERFORMING ORGANIZATION REPORT NUMBER(S) SCA 142		5. MONITORING ORGANIZATION REPORT NUMBER(S) WRDC-TR-89-2056	
6a. NAME OF PERFORMING ORGANIZATION Scientific Computing Assoc., Inc.	6b. OFFICE SYMBOL <i>(if applicable)</i>	7a. NAME OF MONITORING ORGANIZATION Wright Research and Development Center Aero Propulsion and Power Laboratory	
6c. ADDRESS (City, State, and ZIP Code) 246 Church Street, Suite 307 New Haven CT 06510		7b. ADDRESS (City, State, and ZIP Code) Wright-Patterson AFB OH 45433-6563	
8a. NAME OF FUNDING / SPONSORING ORGANIZATION	8b. OFFICE SYMBOL <i>(if applicable)</i>	9. PROCUREMENT INSTRUMENT IDENTIFICATION NUMBER F33615-86-C-2694	
8c. ADDRESS (City, State, and ZIP Code)		10. SOURCE OF FUNDING NUMBERS	
		PROGRAM ELEMENT NO. 65502F	PROJECT NO. 3005
		TASK NO. 20	WORK UNIT ACCESSION NO. 69
11. TITLE (Include Security Classification) Modification and Improvement of Software for Modeling Multidimensional Reacting Fuel Flows			
12. PERSONAL AUTHOR(S) Dr. David Keyes, Mr. Dennis Philbin, Dr. Mitchell Smooke			
13a. TYPE OF REPORT FINAL	13b. TIME COVERED FROM 11/01/86 TO 01/31/89	14. DATE OF REPORT (Year, Month, Day) July 1989	15. PAGE COUNT 97
16. SUPPLEMENTARY NOTATION <i>Cont'd Requirements</i>			
17. COSATI CODES		18. SUBJECT TERMS (Continue on reverse if necessary and identify by block number)	
FIELD 21	GROUP 02	diffusion flame, coupled chemistry and fluid dynamics, flame sheet model, time integration and Newton's method.	
21	05		
19. ABSTRACT (Continue on reverse if necessary and identify by block number) The flame type of most practical combustion devices is the diffusion flame. These flames are important in the interaction of heat and mass transfer with chemical reactions in ramjets, jet turbines and commercial burners. Three-dimensional models that couple the effects of fluid flow with detailed chemical reaction are as yet computationally infeasible. We can, however, obtain important information in practical systems by considering two-dimensional configurations.			
In this report we focus our attention on axisymmetric laminar and turbulent diffusion flames in which a cylindrical fuel stream is surrounded by a coflowing oxidizer jet. In this configuration we can study the interaction of fluid flow with chemical reactions while obtaining a computationally feasible problem. The work centers on the development and application of accurate and efficient computational methods for the solution of the two-dimensional nonlinear boundary value problems describing the reacting systems. In particular, our goals involve the generalization of our (continued on reverse)			
20. DISTRIBUTION / AVAILABILITY OF ABSTRACT <input type="checkbox"/> UNCLASSIFIED/UNLIMITED <input checked="" type="checkbox"/> SAME AS RPT. <input type="checkbox"/> DTC USERS		21. ABSTRACT SECURITY CLASSIFICATION Unclassified	
22a. NAME OF RESPONSIBLE INDIVIDUAL Jeffrey S. Stutrud		22b. TELEPHONE (Include Area Code) (513) 255-7461	22c. OFFICE SYMBOL WRDC/POSE

Unclassified

19. ABSTRACT (continued)

one-dimensional fluid-chemistry model to two dimensions.

We also focus on the use of two-dimensional flame sheet models as starting estimates for the nonlinear equation solver. The highly nonlinear finite rate chemistry-fluid equations are solved by a combination of time integration and a modified Newton's method. The final objective of the research is the incorporation of a "ke" turbulence model into the finite rate chemistry formulation. Both confined and free methane-air flames have been studied. The results of the research are applicable to problems in 1) turbulent reacting flows, 2) engine efficiency, 3) commercial power generation units and 4) pollutant formation.

12.1

Unclassified

Table of Contents

1 Project Summary	1
2 Identification and Significance of the Problem	1
3 Phase II Technical Objectives	1
4 Phase II Work Plan	2
4.1 Laminar Flames	2
4.1.1 Problem Formulation	2
4.1.2 Transport and Chemistry Model	8
4.1.3 Flame Sheet Starting Estimates	10
4.1.4 Computational Approach	15
4.1.5 Numerical Results — Laminar Flames	18
4.2 Turbulent Flames	23
4.2.1 Problem Formulation	24
4.2.2 Transport and Chemistry Model	29
4.2.3 Boundary Conditions and Wall Functions	30
4.2.3.1 Wall Boundaries	31
4.2.3.2 Inflow Boundaries	32
4.2.3.3 Outflow Boundaries	34
4.2.3.4 Symmetry Boundaries	34
4.2.4 Initial Conditions	35
4.2.5 Computational Approach	35
4.2.6 Computational Results	38
Appendix A	83
5.1 Introduction	83
5.2 Numerical Evaluation of Turbulent State Relations	85
5.3 Example and Discussion	87
References	89

<div style="text-align: center; font-size: 2em;">A</div> <div style="display: flex; justify-content: center; gap: 10px;"> <div style="width: 10px; height: 10px; border: 1px solid black;"></div> <div style="width: 10px; height: 10px; border: 1px solid black;"></div> </div>	
--	--



Availability Codes	
Dist	Avail and/or Special
A-1	

1. Project Summary

The flame type of most practical combustion devices is the diffusion flame. These flames are important in the interaction of heat and mass transfer with chemical reactions in ram jets, jet turbines and commercial burners. Three-dimensional models that couple the effects of fluid flow with detailed chemical reactions are as yet computationally infeasible. We can, however, obtain important information in practical systems by considering two-dimensional configurations. In particular, in this report we focus our attention on axisymmetric laminar and turbulent diffusion flames in which a cylindrical fuel stream is surrounded by a coflowing oxidizer jet. In this configuration we can study the interaction of fluid flow with chemical reactions while obtaining a computationally feasible problem. The work centers on the development and application of accurate and efficient computational methods for the solution of the two-dimensional nonlinear boundary value problems describing the reacting systems. In particular, our goals involve the generalization of our one-dimensional fluid chemistry model to two dimensions. We also focus on the use of two-dimensional flame sheet models as starting estimates for the nonlinear equation solver. The highly nonlinear finite rate chemistry-fluid equations are solved by a combination of time integration and a modified Newton method. The final object of the research is the incorporation of a $k - \epsilon$ turbulence model into the finite rate chemistry formulation. Both confined and unconfined methane-air flames have been studied. The results of the research are applicable to problems in 1) turbulent reacting flows, 2) engine efficiency, 3) commercial power generation units, and 4) pollutant formation.

2. Identification and Significance of the Problem

The ability to predict the coupled effects of complex transport phenomena with detailed chemical kinetics is critical in an understanding of turbulent reacting flows, in improving engine efficiency and in the study of pollutant formation. Since three-dimensional models combining both fluid dynamical effects with finite rate chemistry are as yet computationally infeasible, the modeling of chemically reacting flows generally proceeds along two independent paths. In one case chemistry is given priority over fluid mechanical effects and these models are used to assess the important elementary reaction paths, for example, in hydrocarbon fuels. In the other case, multidimensional fluid dynamical effects are emphasized with chemistry receiving little or no priority. The goal in reacting flow computations, however, is to be able to combine the effects of detailed chemistry with complex fluid mechanics.

3. Phase II Technical Objectives

We have investigated the coupled effects of fluid flow with finite rate kinetic models in two-dimensional axisymmetric diffusion flames. The work centered on the development and application of accurate and efficient computational methods for the solution of the two-dimensional nonlinear boundary value problems describing the reacting systems. In particular, our goals involved the generalization of our one-dimensional fluid-chemistry model to two dimensions. We considered a stream function-vorticity formulation with

detailed kinetic theory transport and finite rate chemistry. The Phase II research plan focused on the use of two-dimensional flame sheet models as starting estimates for the nonlinear equation solver. The highly nonlinear finite rate chemistry-fluid equations are solved by a combination of time integration and a modified Newton method. The final objective of the research was the incorporation of a $k - \epsilon$ turbulence model into the finite rate chemistry formulation. The two-dimensional model and solution procedure represent a generalization of our Phase I initiative. The work proposed in Phase II has allowed the investigation of the effects of detailed chemistry and transport on the structure and extinction of hydrocarbon flames. The researcher now has the ability to predict the temperature, major and minor species as well as the velocities in axisymmetric diffusion flames. This level of predictive capability is useful to both the Federal Government and the commercial sector in 1) determining flame extinction limits, in 2) predicting the effect of higher hydrocarbons in the onset of soot formation and in 3) an understanding of flame shape, height, and width.

4. Phase II Work Plan

The modeling of axisymmetric diffusion flames can be reduced to the solution of a set of coupled nonlinear boundary value problems. In these problems we desire solution profiles to as many as several dozen species concentrations in addition to the temperature and the velocity fields. Although axisymmetric flames are important in combustion applications, they have received relatively little attention in theoretical flame studies. Part of this neglect is due to the two-dimensional nature of the problem coupled with the complexities associated with the combined effects of transport phenomena and chemical processes. In the axisymmetric diffusion flame we consider, a fuel jet discharges into a laminar air stream. The flames can be either confined or unconfined. In both cases the tubes through which the fuel and the oxidizer flow are concentric and have radii R_I and R_O , respectively. The two gases make contact at the outlet of the inner tube and a flame that resembles a candle is produced.

Our work plan is divided into five sections. In the first part we consider the formulation of the governing axisymmetric equations. We consider a stream function-vorticity formulation. We next incorporate detailed transport phenomena with finite rate chemistry into the model. This involves the use of kinetic theory expressions for the diffusion coefficients, the viscosity and the thermal conductivity. The reaction mechanism is be inputted via CHEMKIN, the chemical kinetics package developed at Sandia National Laboratories in Livermore, CA [1]. In the third stage, multi-dimensional flame sheet models are used to provide starting estimates for the nonlinear equation solver. In part four we employ a combination of time-stepping and a modified Newton method in solving the large system of highly nonlinear equations. The Newton equations are be solved by a generalized minimum residual method for nonsymmetric systems of linear equations. Finally, we incorporate a $k - \epsilon$ turbulence model into our fluid dynamic-thermochemistry model.

4.1. Laminar Flames

4.1.1. Problem Formulation

Conclusions derived from studies of laminar flames are important in characterizing the combustion processes occurring in turbulent flames, in improving engine efficiency and in

understanding the formation of combustion based pollutants. By studying laminar flames, we can identify the important reactions controlling extinction and we can identify the important species involved in pollutant formation while providing information on the fluid mechanics of the flames. One of the simplest two-dimensional flame configurations with practical importance is the axisymmetric diffusion flame. Although axisymmetric flames are important in combustion applications, they have received relatively little attention in theoretical flame studies. Part of this neglect is due to the two-dimensional nature of the problem coupled with the complexities associated with the combined effects of transport phenomena and chemical processes. In this report we consider two axisymmetric diffusion flame configurations—an unconfined and a confined flame. In the unconfined case a fuel jet discharges into a laminar air stream. The tubes through which the fuel and the oxidizer flow are concentric and have radii R_I and R_O , respectively. The two gases make contact at the outlet of the inner tube and a flame that resembles a candle results (see Figure 1). In the confined problem a cylindrical shield surrounds the fuel and oxidizer tubes (see Figure 2). Our model of axisymmetric laminar diffusion flames considers the full set of two-dimensional governing equations. In primitive variables (r and z denote the radial and axial coordinates, respectively) the governing equations can be written in the form

Continuity:

$$\frac{1}{r} \frac{\partial}{\partial r} (r \rho v_r) + \frac{\partial (\rho v_z)}{\partial z} = 0, \quad (4.1)$$

Radial Momentum:

$$\begin{aligned} & \left[r \rho v_r \frac{\partial v_r}{\partial r} + r \rho v_z \frac{\partial v_r}{\partial z} \right] - 2 \frac{\partial}{\partial r} \left(r \mu \frac{\partial v_r}{\partial r} \right) - \frac{\partial}{\partial z} \left(r \mu \frac{\partial v_r}{\partial z} \right) \\ & + \frac{2}{3} \frac{\partial}{\partial r} \left(\mu \frac{\partial (r v_r)}{\partial r} \right) + \frac{2}{3} \frac{\partial}{\partial r} \left(r \mu \frac{\partial v_z}{\partial z} \right) - \frac{\partial}{\partial z} \left(r \mu \frac{\partial v_z}{\partial r} \right) \\ & + 2 \mu \frac{v_r}{r} - \frac{2 \mu}{3 r} \frac{\partial}{\partial r} (r v_r) - \frac{2}{3} \mu \frac{\partial v_z}{\partial z} + r \frac{\partial p}{\partial r} = 0, \end{aligned} \quad (4.2)$$

Axial Momentum:

$$\begin{aligned} & \left[r \rho v_r \frac{\partial v_z}{\partial r} + r \rho v_z \frac{\partial v_z}{\partial z} \right] - \frac{\partial}{\partial r} \left(r \mu \frac{\partial v_z}{\partial r} \right) - 2 \frac{\partial}{\partial z} \left(r \mu \frac{\partial v_z}{\partial z} \right) \\ & + \frac{2}{3} \frac{\partial}{\partial z} \left(\mu \frac{\partial (r v_r)}{\partial r} \right) + \frac{2}{3} \frac{\partial}{\partial z} \left(r \mu \frac{\partial v_z}{\partial z} \right) - \frac{\partial}{\partial r} \left(r \mu \frac{\partial v_r}{\partial z} \right) + r \frac{\partial p}{\partial z} - r \rho g = 0, \end{aligned} \quad (4.3)$$

Species:

$$\left[r \rho v_r \frac{\partial Y_k}{\partial r} + r \rho v_z \frac{\partial Y_k}{\partial z} \right] + \frac{\partial}{\partial r} (r \rho Y_k V_{k_r}) + \frac{\partial}{\partial z} (r \rho Y_k V_{k_z}) - r W_k \dot{w}_k = 0, \quad k = 1, 2, \dots, K, \quad (4.4)$$

Energy:

$$c_p \left[r \rho v_r \frac{\partial T}{\partial r} + r \rho v_z \frac{\partial T}{\partial z} \right] - \frac{\partial}{\partial r} \left(r \lambda \frac{\partial T}{\partial r} \right) - \frac{\partial}{\partial z} \left(r \lambda \frac{\partial T}{\partial z} \right) + r \sum_{k=1}^K \left\{ \rho c_{pk} Y_k \left(V_{kr} \frac{\partial T}{\partial r} + V_{kz} \frac{\partial T}{\partial z} \right) \right\} + r \sum_{k=1}^K h_k W_k \dot{w}_k = 0. \quad (4.5)$$

Equation of State:

$$\rho = \frac{p \bar{W}}{RT}. \quad (4.6)$$

The system is closed with appropriate boundary conditions on each side of the computational domain. For the unconfined flame we have

Axis of Symmetry ($r = 0$):

$$\frac{\partial \rho}{\partial r} = v_r = \frac{\partial v_z}{\partial r} = \frac{\partial Y_k}{\partial r} = \frac{\partial T}{\partial r} = 0, \quad k = 1, 2, \dots, K, \quad (4.7)$$

Exit ($z \rightarrow \infty$):

$$\frac{\partial v_r}{\partial z} = \frac{\partial v_z}{\partial z} = \frac{\partial Y_k}{\partial z} = \frac{\partial T}{\partial z} = 0, \quad k = 1, 2, \dots, K, \quad (4.8)$$

Inlet ($z = 0$):
 $r < R_I$

$$\rho = \rho_I,$$

$$v_r = 0,$$

$$v_z = v_I, \quad (4.9)$$

$$Y_k = Y_{kI}, \quad k = 1, 2, \dots, K,$$

$$T = T_I,$$

$R_I < r < R_O$

$$\rho = \rho_O,$$

$$v_r = 0,$$

$$v_z = v_O, \quad (4.10)$$

$$Y_k = Y_{kO}, \quad k = 1, 2, \dots, K,$$

$$T = T_O,$$

Outer Zone ($r = R_O$):

$$\frac{\partial v_r}{\partial r} = \frac{\partial v_z}{\partial r} = \frac{\partial Y_k}{\partial r} = \frac{\partial T}{\partial r} = 0, \quad k = 1, 2, \dots, K. \quad (4.11)$$

Identical boundary conditions are employed in the confined flame except for the outer zone. On the shield's surface we have

Outer Zone ($r = R_O$):

$$\begin{aligned} v_r &= v_z = 0, \\ \frac{\partial Y_k}{\partial r} &= 0, \quad k = 1, 2, \dots, K, \\ T &= T_{wall}. \end{aligned} \quad (4.12)$$

The subscripts I and O refer to the inner jet and the outer jet, respectively, and $\rho_I, \rho_O, v_I, v_O, Y_{kI}, Y_{kO}, T_I, T_O$ and T_{wall} are specified quantities.

We can reduce the size of the system to be solved by introducing the vorticity and the stream function [2]. The vorticity is a measure of the counterclockwise rotation in the flow. In particular, formulation of the vorticity transport equation serves to eliminate the pressure as one of the dependent variables. We define the vorticity such that

$$\omega = \frac{\partial v_r}{\partial z} - \frac{\partial v_z}{\partial r}. \quad (4.13)$$

The stream function ψ is used to replace the radial and axial components of the velocity vector by a single function. It is defined in such a way that the continuity equation is satisfied identically. We have

$$\rho r v_r = -\frac{\partial \psi}{\partial z}, \quad (4.14)$$

$$\rho r v_z = \frac{\partial \psi}{\partial r}. \quad (4.15)$$

With the definitions in (4.13)–(4.15), the governing equations become

Stream Function:

$$\frac{\partial}{\partial z} \left(\frac{1}{r\rho} \frac{\partial \psi}{\partial z} \right) + \frac{\partial}{\partial r} \left(\frac{1}{r\rho} \frac{\partial \psi}{\partial r} \right) + \omega = 0, \quad (4.16)$$

Vorticity:

$$\begin{aligned} & r^2 \left[\frac{\partial}{\partial z} \left(\frac{\omega}{r} \frac{\partial \psi}{\partial r} \right) - \frac{\partial}{\partial r} \left(\frac{\omega}{r} \frac{\partial \psi}{\partial z} \right) \right] \\ & - \frac{\partial}{\partial z} \left(r^3 \frac{\partial}{\partial z} \left(\frac{\mu}{r} \omega \right) \right) - \frac{\partial}{\partial r} \left(r^3 \frac{\partial}{\partial r} \left(\frac{\mu}{r} \omega \right) \right) + r^2 g \frac{\partial \rho}{\partial r} + r^2 \nabla \left(\frac{v_r^2 + v_z^2}{2} \right) \cdot \text{iso } \rho = 0, \end{aligned} \quad (4.17)$$

Species Conservation:

$$\left[\frac{\partial}{\partial z} \left(Y_k \frac{\partial \psi}{\partial r} \right) - \frac{\partial}{\partial r} \left(Y_k \frac{\partial \psi}{\partial z} \right) \right] + \frac{\partial}{\partial r} (r \rho Y_k V_{k_r}) + \frac{\partial}{\partial z} (r \rho Y_k V_{k_z}) - r W_k \dot{\omega}_k = 0, \quad k = 1, 2, \dots, K, \quad (4.18)$$

Energy:

$$c_p \left[\frac{\partial}{\partial z} \left(T \frac{\partial \psi}{\partial r} \right) - \frac{\partial}{\partial r} \left(T \frac{\partial \psi}{\partial z} \right) \right] - \frac{\partial}{\partial r} \left(r \lambda \frac{\partial T}{\partial r} \right) - \frac{\partial}{\partial z} \left(r \lambda \frac{\partial T}{\partial z} \right) + r \sum_{k=1}^K \left\{ \rho c_{pk} Y_k \left(V_{k_r} \frac{\partial T}{\partial r} + V_{k_z} \frac{\partial T}{\partial z} \right) \right\} + r \sum_{k=1}^K h_k W_k \dot{\omega}_k = 0, \quad (4.19)$$

where the components of the iso operator are given by $(\partial \rho \partial z, -\partial \rho \partial r)$. The boundary conditions for the unconfined flame in the stream function-vorticity formulation are written in the form

Axis of Symmetry ($r = 0$):

$$\psi = \omega = \frac{\partial Y_k}{\partial r} = \frac{\partial T}{\partial r} = 0, \quad k = 1, 2, \dots, K, \quad (4.20)$$

Exit ($z \rightarrow \infty$):

$$\frac{\partial \psi}{\partial z} = \frac{\partial \omega}{\partial z} = \frac{\partial Y_k}{\partial z} = \frac{\partial T}{\partial z} = 0, \quad k = 1, 2, \dots, K, \quad (4.21)$$

Inlet ($z = 0$):
 $r < R_I$

$$\begin{aligned} \psi &= \rho_I v_I r^2 / 2, \\ \omega &= 0, \\ Y_k &= Y_{k_I}, \quad k = 1, 2, \dots, K, \\ T &= T_I, \end{aligned} \quad (4.22)$$

$R_I < r < R_O$

$$\begin{aligned} \psi &= \frac{1}{2} \rho_I v_I R_I^2 + \frac{1}{2} \rho_O v_O (r^2 - R_I^2), \\ \omega &= 0, \\ Y_k &= Y_{k_O}, \quad k = 1, 2, \dots, K, \\ T &= T_O, \end{aligned} \quad (4.23)$$

Outer Zone ($r = R_O$):

$$\begin{aligned}\psi &= \frac{1}{2}\rho_I v_I R_I^2 + \frac{1}{2}\rho_O v_O (R_O^2 - R_I^2), \\ \frac{\partial \omega}{\partial r} &= 0, \\ \frac{\partial Y_k}{\partial r} &= 0, \quad k = 1, 2, \dots, K, \\ \frac{\partial T}{\partial r} &= 0.\end{aligned}\tag{4.24}$$

The boundary conditions on the shield must again be modified for the confined flame. We have

Outer Zone ($r = R_O$):

$$\begin{aligned}\psi &= \frac{1}{2}\rho_I v_I R_I^2 + \frac{1}{2}\rho_O v_O (R_O^2 - R_I^2), \\ \omega &= \frac{3}{R_O \rho_I} \frac{\psi_I - \psi_{I-1}}{(R_O - R_{I-1})^2} - \frac{\omega_{I-1}}{2}, \\ \frac{\partial Y_k}{\partial r} &= 0, \quad k = 1, 2, \dots, K, \\ T &= T_{wall},\end{aligned}\tag{4.25}$$

where quantities with the subscript $I-1$ in the vorticity boundary condition are evaluated at the grid points next to the shield.

In addition to the variables already defined, T , denotes the temperature; Y_k , the mass fraction of the k^{th} species; p , the pressure; v_r and v_z , the velocities of the fluid mixture in the radial and axial directions, respectively; ρ , the mass density; W_k , the molecular weight of the k^{th} species; \bar{W} , the mean molecular weight of the mixture; R , the universal gas constant; λ , the thermal conductivity of the mixture; c_p , the constant pressure heat capacity of the mixture; c_{pk} , the constant pressure heat capacity of the k^{th} species; \dot{w}_k , the molar rate of production of the k^{th} species per unit volume; h_k , the specific enthalpy of the k^{th} species; g , the gravitational constant; μ the viscosity of the mixture and V_{k_r} and V_{k_z} , the diffusion velocities of the k^{th} species in the radial and axial directions, respectively. Specifically, we write

$$V_{k_r} = -(1/X_k) D_k \frac{\partial X_k}{\partial r}, \quad k = 1, 2, \dots, K,\tag{4.26}$$

$$V_{k_z} = -(1/X_k) D_k \frac{\partial X_k}{\partial z}, \quad k = 1, 2, \dots, K,\tag{4.27}$$

where X_k is the mole fraction of the k^{th} species and D_k is related to the binary diffusion coefficients through the relation (see, e.g., [3])

$$D_k = \frac{(1 - Y_k)}{\sum_{j \neq k}^K X_j / D_{jk}}. \quad (4.28)$$

4.1.2. Transport and Chemistry Model

The transport of momentum, species mass fractions and energy in a chemically reacting flow requires the evaluation of the mixture viscosity, the thermal conductivity of the mixture and the diffusion coefficients of the species. Accurate and efficient evaluation of these quantities is an important aspect of combustion calculations. We have modeled the given transport coefficients by the following procedures.

Diffusion Velocity

The binary diffusion coefficients D_{jk} can be written as functions of the temperature and the pressure [4]. We have

$$D_{jk} = \frac{3}{16} \frac{\sqrt{2\pi k_B^3 T^3 / M_{jk}}}{p\pi\sigma_{jk}^2 \Omega(1,1)^*}. \quad (4.29)$$

In the above formula M_{jk} denotes the reduced mass (molecular) for the (j, k) species pair

$$M_{jk} = \frac{2M_j M_k}{M_j + M_k}, \quad (4.30)$$

σ_{jk} is the averaged collision diameter, $\Omega(1,1)^*$ is a collision integral and k_B denotes Boltzmann's constant. A similar expression can be written for V_{k_s} .

Viscosity

The single component viscosities can be written in the form [4].

$$\mu_k = \frac{5}{16} \frac{\sqrt{\pi M_k k_B T}}{\pi\sigma_k^2 \Omega(2,2)^*}, \quad (4.31)$$

where M_k is the mass of the molecule, σ_k is the Lennard-Jones collision diameter and $\Omega(2,2)^*$ is a collision integral.

Given the single component viscosities, we evaluate the mixture viscosity using the averaging formula recommended by Mathur et. al. [5]. We have

$$\mu = \frac{1}{2} \left(\sum_{k=1}^K X_k \mu_k + \frac{1}{\sum_{k=1}^K X_k / \mu_k} \right). \quad (4.32)$$

Thermal Conductivity

The single component thermal conductivities can be written in the form [6]

$$\lambda_k = \frac{\mu_k}{W_k} (f_{trans} C_{v,trans} + f_{rot} C_{v,rot} + f_{vib} C_{v,vib}), \quad (4.33)$$

where the quantities f_{trans} , f_{rot} and f_{vib} are given by

$$f_{trans} = \frac{5}{2} \left(1 - \frac{2}{\pi} \frac{C_{v,rot}}{C_{v,trans}} \frac{A}{B} \right), \quad (4.34)$$

$$f_{rot} = \frac{\rho D_{kk}}{\mu_k} \left(1 + \frac{2}{\pi} \frac{A}{B} \right), \quad (4.35)$$

$$f_{vib} = \frac{\rho D_{kk}}{\mu_k}, \quad (4.36)$$

$$A = \frac{5}{2} - \frac{\rho D_{kk}}{\mu_k}, \quad (4.37)$$

$$B = Z_{rot} + \frac{2}{\pi} \left(\frac{5}{3} \frac{C_{v,rot}}{R} + \frac{\rho D_{kk}}{\mu_k} \right). \quad (4.38)$$

The specific heats for the case of a linear molecule take the familiar forms. We have

$$\frac{C_{v,rot}}{C_{v,trans}} = \frac{2}{3}, \quad (4.39)$$

$$\frac{C_{v,rot}}{R} = 1, \quad (4.40)$$

and

$$C_{v,vib} = C_v - \frac{5}{2} R. \quad (4.41)$$

The rotational relaxation collision number is available from Parker [7] and Brau and Jonkman [8].

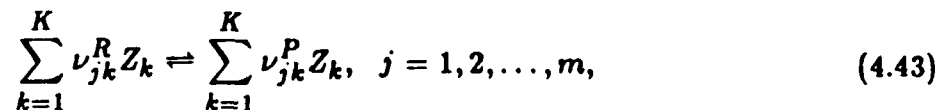
The mixture conductivity is evaluated from the averaging formula of Mathur et. al. [5]. We have

$$\lambda = \frac{1}{2} \left(\sum_{k=1}^K X_k \lambda_k + \frac{1}{\sum_{k=1}^K X_k / \lambda_k} \right). \quad (4.42)$$

Kinetics Model

The burning of hydrocarbon fuels proceeds through a complex sequence of elementary reversible reactions. The intermediate species in such mechanisms are of extreme importance. They are involved in the chain initiation, chain propagation, chain inhibition and chain breaking reactions that describe the oxidation of a given fuel. We model the kinetic aspects of axisymmetric diffusion flames by allowing the chemical production and

destruction of a species to occur through a sequence of m reversible elementary chemical reactions. We can represent these reactions in the form



where ν_{jk}^R (ν_{jk}^P) is the stoichiometric coefficient of species k appearing as a reactant (product) in reversible reaction $j = 1, 2, \dots, m$ and where Z_k represents the chemical symbol for the k^{th} species.

The production rate \dot{w}_k for the k^{th} species can be written in the form

$$\dot{w}_k = \sum_{j=1}^m (\nu_{jk}^P - \nu_{jk}^R) \left[k_j^f(T) \prod_{n=1}^K \left(\frac{\rho Y_n}{W_k} \right)^{\nu_{jn}^R} - k_j^r(T) \prod_{n=1}^K \left(\frac{\rho Y_n}{W_k} \right)^{\nu_{jn}^P} \right]. \quad (4.44)$$

The function k_j^f (k_j^r) is the rate constant for the forward (reverse) path of reaction j . We assume k_j^f has the following modified Arrhenius temperature dependence

$$k_j^f = A_j^f T^{\beta_j^f} \exp(-E_j^f / RT), \quad (4.45)$$

with a similar expression for k_j^r . The reverse rate constant can be written in terms of the forward rate constant and the equilibrium constants K_j^c by

$$k_j^r = k_j^f / K_j^c. \quad (4.46)$$

The pre-exponential factor A_j^f , the temperature exponent β_j^f and the activation energy E_j^f can be compiled from published experimental work. A typical mechanism for the burning of methane in air is included in Appendix I.

4.1.3. Flame Sheet Starting Estimates

The governing equations in (4.1)–(4.12) or (4.16)–(4.25) are highly nonlinear and require a starting estimate for the finite difference method described in the next section. The determination of a sufficiently “good” initial solution estimate in two-dimensional problems can be difficult. The difficulty is due to the exponential dependence of the chemistry terms on the temperature and to the multidimensional nonlinear coupling of the fluid and the thermochemistry solution fields. In previous work, we focused our efforts on the solution of adiabatic and nonadiabatic premixed laminar flames by adaptive finite difference methods [9, 10, 11, 12]. In these problems the governing differential equations were discretized and the resulting nonlinear difference equations were solved by Newton’s method. Cubic polynomials and Gaussian shaped profiles were used as starting estimates for the major and minor species on an initial coarse grid. In adiabatic and nonadiabatic premixed laminar flame problems the conservation of mass and momentum reduced to

the specification of a constant mass flow rate and a constant thermodynamic pressure. Hence, thermochemical considerations played a more important role in these problems than did fluid dynamical aspects. This is not the case in axisymmetric laminar diffusion flames. There is a strong coupling between the fluid dynamic and the thermochemistry solution fields in these flames. We have found that the solution procedure used in premixed laminar flame problems does not provide a sufficiently robust or efficient starting estimate from which Newton's method will converge. In addition, the relaxation of these starting estimates by time-dependent methods to steady-state (or at least until the solution is within the convergence domain of Newton's method) is extremely slow. The importance of these flames in combustion modeling, however, necessitates the development of an efficient starting procedure.

The burning rate in a diffusion flame is controlled by the rate at which the fuel and the oxidizer are brought together in the proper proportions. This is in distinction to premixed flames where the burning rate is controlled by chemical reactions. In the limit of infinitely fast kinetics, the fuel and the oxidizer are separated by a thin exothermic reaction zone. In this zone the fuel and the oxidizer are in stoichiometric proportion and the temperature and products of combustion are maximized. In such an ideal situation, no oxidizer is present on the fuel side and no fuel is present on the oxidizer side. The fuel and oxidizer diffuse towards the reaction zone as a result of concentration gradients in the flow. In diffusion flames of practical interest, the oxidation of the fuel to form intermediates and products proceeds through a detailed kinetics mechanism. In these problems combustion takes place at a finite rate and some fuel and oxidizer co-exist on either side of the reaction zone. Nevertheless, the use of a thin, infinitely fast, global reaction model is a natural starting point for the determination of a "good" initial solution estimate for our finite rate axisymmetric model (see also Burke and Schumann [13], Mitchell [2], Mitchell et al. [14], Smooke et al. [15], and Keyes and Smooke [16]).

We assume that the fuel and the oxidizer obey a single overall irreversible reaction of the type



in the presence of an inert gas (N). We have



where ν_F, ν_X and ν_P are the stoichiometric coefficients of the fuel, the oxidizer and the product, respectively. In addition, we neglect thermal diffusion and assume that c_p and c_{p_k} are constant and that the ordinary mass diffusion velocities can be written in terms of Fick's law. With these approximations we can write

Stream Function:

$$\frac{\partial}{\partial z} \left(\frac{1}{r\rho} \frac{\partial \psi}{\partial z} \right) + \frac{\partial}{\partial r} \left(\frac{1}{r\rho} \frac{\partial \psi}{\partial r} \right) + \omega = 0, \quad (4.49)$$

Vorticity:

$$r^2 \left[\frac{\partial}{\partial z} \left(\frac{\omega}{r} \frac{\partial \psi}{\partial r} \right) - \frac{\partial}{\partial r} \left(\frac{\omega}{r} \frac{\partial \psi}{\partial z} \right) \right]$$

$$-\frac{\partial}{\partial z} \left(r^3 \frac{\partial}{\partial z} \left(\frac{\mu}{r} \omega \right) \right) - \frac{\partial}{\partial r} \left(r^3 \frac{\partial}{\partial r} \left(\frac{\mu}{r} \omega \right) \right) + r^2 g \frac{\partial \rho}{\partial r} + r^2 \nabla \left(\frac{v_r^2 + v_z^2}{2} \right) \cdot \text{iso } \rho = 0, \quad (4.50)$$

Species:

$$\begin{aligned} & - \left[\frac{\partial}{\partial r} \left(Y_F \frac{\partial \psi}{\partial z} \right) + \frac{\partial}{\partial z} \left(Y_F \frac{\partial \psi}{\partial r} \right) \right] - \frac{\partial}{\partial r} \left(r \rho D_F \frac{\partial Y_F}{\partial r} \right) \\ & \quad - \frac{\partial}{\partial z} \left(r \rho D_F \frac{\partial Y_F}{\partial z} \right) - r W_F \nu_F \dot{\omega} = 0, \end{aligned} \quad (4.51)$$

$$\begin{aligned} & - \left[\frac{\partial}{\partial r} \left(Y_X \frac{\partial \psi}{\partial z} \right) + \frac{\partial}{\partial z} \left(Y_X \frac{\partial \psi}{\partial r} \right) \right] - \frac{\partial}{\partial r} \left(r \rho D_X \frac{\partial Y_X}{\partial r} \right) \\ & \quad - \frac{\partial}{\partial z} \left(r \rho D_X \frac{\partial Y_X}{\partial z} \right) - r W_X \nu_X \dot{\omega} = 0, \end{aligned} \quad (4.52)$$

$$\begin{aligned} & - \left[\frac{\partial}{\partial r} \left(Y_P \frac{\partial \psi}{\partial z} \right) + \frac{\partial}{\partial z} \left(Y_P \frac{\partial \psi}{\partial r} \right) \right] - \frac{\partial}{\partial r} \left(r \rho D_P \frac{\partial Y_P}{\partial r} \right) \\ & \quad - \frac{\partial}{\partial z} \left(r \rho D_P \frac{\partial Y_P}{\partial z} \right) + r W_P \nu_P \dot{\omega} = 0, \end{aligned} \quad (4.53)$$

$$\begin{aligned} & - \left[\frac{\partial}{\partial r} \left(Y_N \frac{\partial \psi}{\partial z} \right) + \frac{\partial}{\partial z} \left(Y_N \frac{\partial \psi}{\partial r} \right) \right] - \frac{\partial}{\partial r} \left(r \rho D_N \frac{\partial Y_N}{\partial r} \right) \\ & \quad - \frac{\partial}{\partial z} \left(r \rho D_N \frac{\partial Y_N}{\partial z} \right) = 0, \end{aligned} \quad (4.54)$$

and

Energy:

$$\begin{aligned} & c_p \left[\frac{\partial}{\partial z} \left(T \frac{\partial \psi}{\partial r} \right) - \frac{\partial}{\partial r} \left(T \frac{\partial \psi}{\partial z} \right) \right] - \frac{\partial}{\partial r} \left(r \lambda \frac{\partial T}{\partial r} \right) - \frac{\partial}{\partial z} \left(r \lambda \frac{\partial T}{\partial z} \right) \\ & \quad - r \frac{W_F \nu_F h_F + W_X \nu_X h_X - W_P \nu_P h_P}{c_p} \dot{\omega} = 0, \end{aligned} \quad (4.55)$$

where

$$\dot{\omega} = -\frac{\dot{w}_F}{\nu_F} = -\frac{\dot{w}_X}{\nu_X} = \frac{\dot{w}_P}{\nu_P}, \quad (4.56)$$

is the rate of progress of the reaction.

If we introduce the heat release per unit mass of the fuel Q where

$$Q = h_F + \frac{W_X \nu_X}{W_F \nu_F} h_X - \frac{W_P \nu_P}{W_F \nu_F} h_P, \quad (4.57)$$

and if we assume that the Lewis numbers

$$\text{Le}_F = \frac{\lambda}{\rho D_F c_p}, \quad \text{Le}_X = \frac{\lambda}{\rho D_X c_p}, \quad (4.58a)$$

$$Le_P = \frac{\lambda}{\rho D_P c_p}, \quad Le_N = \frac{\lambda}{\rho D_N c_p}, \quad (4.59)b$$

are all equal to one, then each of the Shvab-Zeldovich variables

$$Z_F = Y_F - Y_{F_0} + \frac{c_p}{Q}(T - T_0), \quad (4.60)$$

$$Z_X = Y_X - Y_{X_0} + \frac{c_p}{Q} \frac{W_{X\nu X}}{W_{F\nu F}}(T - T_0), \quad (4.61)$$

$$Z_P = Y_P - Y_{P_0} - \frac{c_p}{Q} \frac{W_{P\nu P}}{W_{F\nu F}}(T - T_0), \quad (4.62)$$

$$Z_N = Y_N - Y_{N_0}, \quad (4.63)$$

satisfies the differential equation

$$\begin{aligned} & \left[-\frac{\partial}{\partial r} \left(Z_k \frac{\partial \psi}{\partial z} \right) + \frac{\partial}{\partial z} \left(Z_k \frac{\partial \psi}{\partial r} \right) \right] - \frac{\partial}{\partial r} \left(r \rho D_k \frac{\partial Z_k}{\partial r} \right) \\ & - \frac{\partial}{\partial z} \left(r \rho D_k \frac{\partial Z_k}{\partial z} \right) = 0, \quad k = F, X, P, N. \end{aligned} \quad (4.64)$$

One can show that all of the Z_k are proportional to each other and to a conserved scalar S which satisfies an equation similar in form to (4.64).

To complete the specification of the starting estimate, we must be able to recover the temperature and the major species profiles from the conserved scalar. Of critical importance to this procedure is an estimate of the location of the flame front. In the Shvab-Zeldovich formulation fuel and oxidizer cannot co-exist. Hence, on the fuel side of the flame $Y_X = 0$ and on the oxidizer side $Y_F = 0$. If we denote variables at the flame front with the subscript f , then it can be shown (see also Keyes and Smooke [16]) that, for a fixed value of the axial coordinate z , the location of the flame front is defined such that

$$S(r_f)|_{fixed z} = S_f = \frac{Y_{X_0}}{Y_{X_0} + \frac{W_{X\nu X}}{W_{F\nu F}} Y_{F_0}}. \quad (4.65)$$

The location of the flame front can be obtained by solving (4.65) at each axial coordinate level.

If we utilize the proportionality of the Z_k 's to S along with the expressions in (4.49)–(4.63), we can derive expressions for the temperature and species on the fuel and oxidizer sides of the flame. On the fuel side, we have

$$T = T_I S + \left[T_0 + Y_{X_0} \frac{Q}{c_p} \frac{W_{F\nu F}}{W_{X\nu X}} \right] (1 - S), \quad (4.66)$$

$$Y_F = Y_{F_I} S + Y_{X_0} \frac{W_{F\nu F}}{W_{X\nu X}} (S - 1), \quad (4.67)$$

$$Y_X = 0, \quad (4.68)$$

$$Y_P = Y_{XO} \frac{W_{P\nu P}}{W_{X\nu X}} (1 - S), \quad (4.69)$$

and

$$Y_N = Y_{NO} (1 - S) + Y_{NI} S. \quad (4.70)$$

On the oxidizer side, we have

$$T = T_O (1 - S) + \left[\frac{Q}{c_p} Y_{FI} + T_I \right] S, \quad (4.71)$$

$$Y_F = 0, \quad (4.72)$$

$$Y_X = Y_{XO} (1 - S) - Y_{FI} \frac{W_{X\nu X}}{W_{F\nu F}} S, \quad (4.73)$$

$$Y_P = \frac{W_{P\nu P}}{W_{F\nu F}} Y_{FI} S, \quad (4.74)$$

and

$$Y_N = Y_{NO} (1 - S) + Y_{NI} S. \quad (4.75)$$

The equations in (4.49), (4.50) and (4.64) are solved for the stream function, the vorticity, the temperature and the major species in the flame. For a given profile of the conserved scalar, we solve (4.65) for the location of the flame front on each axial level. We then utilize the relations in (4.66)-(4.75) to obtain expressions for T , Y_F , Y_O , Y_P and Y_N . The recovered temperature profile is used in the ideal gas law to evaluate the density. The temperature is also needed in forming the viscosity and the diffusion coefficient (D_k is replaced by D). If we introduce the Prandtl number

$$\text{Pr} = \frac{\mu c_p}{\lambda}, \quad (4.76)$$

and recall that all of the Lewis numbers are equal to one, we can write

$$\rho D = \frac{\lambda}{c_p} = \frac{\mu}{(\text{Pr})_{ref}}, \quad (4.77)$$

where $(\text{Pr})_{ref}$ is a reference Prandtl number. Specifically, we use an approximate value for air, $(\text{Pr})_{ref} = 0.75$. Hence, determination of ρD is reduced to the specification of a transport relation for the viscosity. We use the simple power law

$$\mu = \mu_0 \left(\frac{T}{T_0} \right)^r, \quad (4.78)$$

where $r = 0.7$, $T_0 = 298$ K and $\mu_0 = 1.85 \times 10^{-4}$ gm/cm-sec is again a reference value for air [17]. The temperature exponent was determined by fitting the equation in (4.78) to the mixture viscosity and temperature data of a representative one-dimensional finite

rate chemistry calculation. The scaled heat release parameter Q/c_p can be determined from an estimate of the peak temperature (e.g., from an experiment) or from the heat of combustion of the system under consideration and a representative heat capacity.

4.1.4. Computational Approach

Most of the detailed chemistry, computational combustion studies that have appeared in the literature have focused on essentially one-dimensional configurations, i.e., freely propagating or burner-stabilized premixed flames and counterflow premixed or diffusion flames (Spalding [18], Adams and Cook [19], Dixon-Lewis [20, 21], Spalding et al. [22], Wilde [23], Bledjian [24], Margolis [25], Warnatz [26, 27, 28], Westbrook and Dryer [29, 30], Coffee and Heimerl [31, 32], Miller et al. [9, 10, 33], Smooke [11], Smooke et al. [34, 12, 35, 36], Hahn and Wendt [37], Sato and Tsuji [38], Dixon-Lewis et al. [39], Giovangigli and Smooke [40]). The interaction of heat and mass transfer and chemical reaction in practical combustion systems, however, requires a multidimensional study.

Our goal is to obtain a discrete solution of the governing equations in two dimensions on the mesh \mathcal{M}_z the initial nodes of which are formed by the intersection of the lines of the mesh \mathcal{M}_r

$$\mathcal{M}_r = \{0 = r_0 < r_1 < \dots < r_i \dots < r_{M_r} = R_0\}, \quad (4.79)$$

and the mesh \mathcal{M}_z

$$\mathcal{M}_z = \{0 = z_0 < z_1 < \dots < z_j \dots < z_{M_z} = Z\}. \quad (4.80)$$

Computationally, we combine a steady-state and a time-dependent solution method. A time-dependent approach is used to help obtain a converged numerical solution on an initial coarse grid using the flame sheet starting estimate. Grid points are then inserted adaptively and the steady-state solution procedure is used to complete the problem.

Newton's Method

We approximate the spatial operators in the governing partial differential equations by finite difference expressions. Diffusion terms are approximated by centered differences and convective terms by upwind approximations. The problem of finding an analytic solution of the equations is then converted into one of finding an approximation to this solution at each point (r_i, z_j) of the mesh in two dimensions. With the difference equations written in residual form, we seek the solution U^* of the system of nonlinear equations

$$F(U) = 0. \quad (4.81)$$

For an initial solution estimate U^0 which is sufficiently close to U^* , the system of nonlinear equations in (4.81) can be solved by Newton's method. This leads to the iteration

$$J(U^n)(U^{n+1} - U^n) = -\lambda^n F(U^n), \quad n = 0, 1, 2, \dots \quad (4.82)$$

$J(U^n) = \partial F(U^n)/\partial U$ is the Jacobian matrix and λ^n ($0 < \lambda \leq 1$) is the n^{th} damping parameter [41].

We point out that with the spatial discretizations used in forming (4.81), the Jacobian matrix in (4.82) can be written in block nine diagonal form. For problems involving

detailed transport and complex chemistry, it is often more efficient to evaluate the Jacobian matrix numerically as opposed to analytically. The numerical procedure we implement extends the ideas outlined by Curtis, Powell and Reid [42]. We form several columns of the Jacobian simultaneously using vector function evaluations and the Jacobian's given sparsity structure. If to each column of the Jacobian we associate the i and j values of the node corresponding to the column's diagonal block, then all columns of the Jacobian having the same value of the parameter

$$\alpha = (i + 3j) \bmod 9, \quad (4.83)$$

can be evaluated simultaneously. Ideas along these lines have also been explored by Newsam and Ramsdell [43] and Coleman and More [44]. Once the Jacobian is formed we solve the Newton equations with a block-line SOR method. The Newton iteration continues until the size of $\|U^{n+1} - U^n\|_2$ is reduced appropriately.

Adaptive Gridding

The solutions of the governing equations in the axisymmetric problems contain regions in each coordinate direction in which the dependent variables exhibit high spatial activity (steep fronts and sharp peaks). Efficient solution of these problems requires that the high activity regions be resolved adaptively. Techniques that attempt to equidistribute positive weight functions have been used with a great deal of success in premixed and counterflow flame problems. Flames with 30 to 40 chemical species and over 100 chemical reactions can be solved efficiently by adaptively placing grid points in the high activity regions. We follow a similar approach in the axisymmetric problem.

Adaptive mesh refinement in two dimensions can proceed along several different paths. The simplest procedure involves determining the grid points of the mesh M_z by equidistributing positive weight functions over mesh intervals in both the r and z directions (see, e.g., Kautsky and Nichols [45] and Russell [46]). Specifically, we attempt to equidistribute the mesh M_r with respect to the non-negative function W_r and constant C_r for each of the $M_z + 1$ horizontal grid lines. We write

$$\int_{r_i}^{r_{i+1}} W_r \, dr < C_r, \quad i = 0, 1, \dots, M_r - 1, \quad (4.84)$$

for $j = 0, 1, \dots, M_z$. Similarly, we attempt to equidistribute the mesh M_z with respect to the non-negative function W_z and constant C_z for each of the $M_r + 1$ vertical grid lines. We have

$$\int_{z_j}^{z_{j+1}} W_z \, dz < C_z, \quad j = 0, 1, \dots, M_z - 1, \quad (4.85)$$

for $i = 0, 1, \dots, M_r$.

In implementing the two-dimensional adaptive grid strategy, we first solve the boundary value problem on an initial coarse grid. We then test the inequality in (4.84) one r subinterval at a time for all the j grid lines and all the dependent solution components. If the inequality is not satisfied, a grid point is inserted at the midpoint of the r subinterval in question for $j = 0, 1, \dots, M_z$. Once this procedure has been carried out in the r direction,

we reverse the process and begin again in the z direction. This procedure produces an orthogonal tensor product grid in which the coordinate lines connect opposite boundaries of the computational domain. The weight functions in the equidistribution procedure are chosen such that the grid points are placed in regions of high spatial activity with the goal of reducing the local discretization error. We use a combination of first and second derivatives of the solution profiles (see also Smooke [11, 47], Giovangigli and Smooke [40]). The particular combinations of function and slope and the values of C_r and C_x can be changed to produce a solution to a desired level of accuracy.

Coarse to Fine Grid Methodology

The formation of the Jacobian and its partial factorization in the block-line SOR method accounts for a substantial part of the cost of the diffusion flame calculation. As a result, the use of a modified Newton method in which the Jacobian is re-evaluated periodically is indicated. The immediate implication of applying the modified Newton method is that the partial factorization of the Jacobian can be stored and each modified Newton iteration can be obtained by performing relatively inexpensive block-line SOR back substitutions. The problem one faces when applying the modified method is how to determine whether the rate of convergence is fast enough. If the rate is too slow we want to change back to a full Newton method and make use of new Jacobian information. If the rate of convergence is acceptable, we want to continue performing modified Newton iterations.

In our adaptive grid strategy, the equidistribution condition is checked one mesh interval at a time and grid points are added appropriately. The coarse grid solution is then interpolated linearly onto the new finer grid. The interpolated result serves as an initial solution estimate for the iteration procedure on the finer grid. The process is continued on successively finer and finer grids until several termination criteria are satisfied. We anticipate that as the size of the mesh spacing gets smaller, the interpolated solution should become a better starting estimate for Newton's method on the next finer grid. For a class of nonlinear boundary value problems, Smooke and Mattheij [48] have shown that there exists a critical mesh spacing such that the interpolated solution lies in the domain of convergence of Newton's method on the next grid. As a result, the hypotheses of the Kantorovich theorem [49] are satisfied and the sequence of successive modified Newton iterates can be shown to satisfy a recurrence relation scaled by the first Newton step [50]. As a result, if in the course of a calculation, we determine that the size of the $(n+1)^{\text{st}}$ modified Newton step is larger than the value predicted by the theorem, we form a new Jacobian and restart the iteration count.

Time-Dependent Starting Estimates

The coarse to fine grid strategy and the flame sheet starting estimate helps eliminate many of the convergence difficulties associated with solving the governing equations directly. Nevertheless, to obtain a starting estimate on the initial grid that lies in the convergence domain of Newton's method we apply a time-dependent iteration to the flame sheet solution. We remark that fundamentally there are two mathematical approaches for solving flame problems - one uses a transient method and the other solves the steady-state boundary value problems directly. Generally speaking, the transient methods are robust

but computationally inefficient compared to the boundary value methods, which are efficient but have less desirable convergence properties. Most of the numerical techniques that have been used to solve one-dimensional flame problems have employed a time-dependent method. Variations of this approach have been considered by a variety of researchers (see, *e.g.*, Spalding [18], Adams and Cook [19], Dixon-Lewis [20, 21], Spalding et al. [22], Bledjian [24], Margolis [25], Warnatz [26, 27, 28], Westbrook and Dryer [29, 30], Coffee and Heimerl [31, 32]). In these methods, the original nonlinear two-point boundary value problem is converted into a nonlinear parabolic mixed initial-boundary value problem. This is accomplished by appending the term $\partial(\bullet)/\partial t$ to the left-hand side of the conservation equations. This same procedure can be employed in our two-dimensional calculations. We obtain

$$\frac{\partial U}{\partial t} = F(U), \quad (4.86)$$

with appropriate initial conditions. If the time derivative is replaced, for example, by a backward Euler approximation, the governing equations can be written in the form

$$\mathcal{F}(U^{n+1}) = F(U^{n+1}) - \frac{(U^{n+1} - U^n)}{\tau^{n+1}} = 0, \quad (4.87)$$

where for a function $g(t)$ we define $g^n = g(t^n)$ and where the time step $\tau^{n+1} = t^{n+1} - t^n$. At each time level we must solve a system of nonlinear equations that look very similar to the nonlinear equations in (4.81). Newton's method can again be used to solve this system. The important difference between the system in (4.81) and (4.87) is that the diagonal of the steady-state Jacobian is weighted by the quantity $1/\tau^{n+1}$. This produces a better conditioned system and the solution from the n^{th} time step ordinarily provides an excellent starting guess to the solution at the $(n+1)^{\text{st}}$ time level. The work per time step is similar to that for the modified Newton iteration, but the timelike continuation of the numerical solution produces an iteration strategy that will, in general, be less sensitive to the initial starting estimate than if Newton's method were applied to (4.81) directly. As a result, when we ultimately implement Newton's method on the steady-state equations directly, we obtain a converged numerical solution with only a few additional iterations. This time-dependent starting procedure can also be used on grids other than the initial one. The size of the time steps are chosen by monitoring the local truncation error of the time discretization process (see also, Smooke et al. [35]).

4.1.5. Numerical Results — Laminar Flames

In this section we apply the flame sheet starting estimate and the computational method discussed in the previous section to both a confined and an unconfined methane-air, axisymmetric laminar diffusion flame. Detailed transport coefficients and a 42 reaction, fifteen species reaction mechanism (see Table I, Miller et al. [33] and Smooke et al. [36] were used in the calculations.

Confined Flame

The first flame we consider is a confined methane-air diffusion flame studied experimentally by Mitchell [2]. The experimental configuration is such that the radius of the inner fuel jet $R_f = 0.635$ cm, the radius of the outer oxidizer jet $R_o = 2.54$ cm and the

length of the tubular pyrex shield $Z = 30.0$ cm. Fuel is introduced through the center tube and air through the outer coflow. The boundary conditions at the inlet are given by

Inlet ($z = 0$):
 $r < R_I$

$$\begin{aligned} T &= 298 \text{ K}, \\ Y_{CH_4} &= 1.0, Y_k = 0, k \neq CH_4, \\ v_r &= 0.0 \text{ cm/sec}, \\ v_z &= 4.5 \text{ cm/sec}, \end{aligned} \quad (4.88)$$

$R_I < r < R_O$

$$\begin{aligned} T &= 298 \text{ K}, \\ Y_{O_2} &= .232, Y_{N_2} = .768, Y_k = 0, k \neq O_2, N_2, \\ v_r &= 0.0 \text{ cm/sec}, \\ v_z &= 9.88 \text{ cm/sec}. \end{aligned} \quad (4.89)$$

The appropriate boundary conditions for the stream function-vorticity system can be formed using the definition in (4.13) along with (4.22)–(4.23). The shield temperature is kept constant at 298 K.

The flame sheet model provided initial solution profiles for the stream function, the vorticity, the temperature and the major species, *i.e.*, CH_4 , O_2 , N_2 , CO_2 and H_2O . The starting estimates for the minor species in the full chemistry solution were approximated by Gaussian profiles that were centered at the location of the flame sheet on each axial level. They had peak heights of at most a few percent. To conserve mass in the starting estimate, the N_2 mass fraction was reduced accordingly. The flame sheet starting estimate required approximately 150 adaptive time steps and five Newton iterations to converge. Once the flame sheet estimate was calculated, we solved the full set of governing equations in a two-step procedure. We first determined a solution to the stream function, vorticity and species equations (4.16)–(4.18) based on the flame sheet temperature profile. This fixed flame sheet temperature solution (T_{OUT}) was then used as input to the full fluid dynamic-thermochemistry model (4.16)–(4.19) in which the energy equation was included (T_{IN}). This procedure helped to reduce both convergence difficulties and the total CPU time and is similar to the two-pass solution method used in the solution of adiabatic premixed laminar flames [12] and counterflow diffusion flames [16].

The flame sheet and the first T_{OUT} calculation were performed on a 40×28 tensor product grid. One hundred fifty-five adaptive time steps were required to reduce the norm of the T_{OUT} steady-state residuals below 1.0×10^{-3} . This was sufficient to bring the numerical solution within the convergence domain of Newton's method. After the time steps, Newton's method converged with only seven iterations. Once this solution was obtained, the mesh was refined and a solution was calculated on a finer grid. This procedure was continued until a refined 75×41 grid was obtained. The refined fixed

temperature solution was then used as the starting estimate for the complete fluid dynamic-thermochemistry solution. As the computational mesh was refined, Newton's method typically converged with a smaller number of time steps than on the coarser grids. The mesh spacing was such that 32000 equispaced points would have been needed to obtain comparable accuracy. The total CPU time for the entire procedure was approximately 150 hours on an FPS-264 which is consistent with a single one-dimensional counterflow diffusion flame calculation that requires between 2-3 hours on the same machine.

Mitchell [2] has measured radial temperature profiles at several heights above the burner using three mil Pt vs. Pt-13% Rh thermocouples. The measurements were corrected for radiative losses. Major species were sampled with quartz microprobes and then analyzed with a gas chromatograph. The probe had a maximum outside diameter of 0.75 mm and was tapered to 0.15 mm at the tip. The inner diameter was approximately 50μ . In Figure 3 we compare the radial experimental and calculated temperature profiles at a height of 1.2 cm above the burner. We observe excellent agreement between the two profiles from the axis of symmetry to the low temperature coflow region. In Figures 4 and 5 we compare radial experimental and computational profiles for the major species in the flame (CH_4 , O_2 , N_2 , H_2O , CO_2 , CO and H_2) at a height of 1.2 cm above the burner. The agreement among all the computational and experimental profiles is very good. Several features in Figures 4 and 5 are worth noting, however. From Figure 4 it is clear that the methane diffuses to the reaction zone where it is completely consumed. The oxygen concentration outside the flame region is near its inlet value and then drops nearly to zero in the reaction zone. It then slightly increases as the symmetric axis is approached. This type of oxygen profile results near the flame base because the temperatures are low enough to allow some oxygen to penetrate the flame. In the radial direction water and carbon dioxide maximize in the region of the peak temperature. In the lower regions of the flame the carbon monoxide and hydrogen profiles first increase with distance from the symmetric axis then proceed through a maximum and finally decrease to zero in the reaction zone. Similar profiles for the temperature and major species are illustrated in Figures 6-8 at a height of 2.4 cm above the burner. We note that the experimental temperature profile is somewhat narrower than the computed one but the peak values and the trend in the major species profiles is again excellent. Experimentally, temperature profiles were not obtained from 2.5 cm to 5.0 cm above the burner due to the tendency of carbon particles to collect on the thermocouple bead.

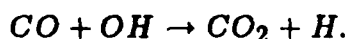
A more global picture of this flame can be obtained by plotting the temperature and species contours versus the independent spatial coordinates. In Figures 9-11 we illustrate the temperature isotherms and the methane and oxygen isopleths, respectively, as functions of the axial and radial coordinates. We note immediately the high temperature region extending from the boundary of the fuel and oxidizer jets to the axis of symmetry. The figure also points out the extremely high temperature gradients directly above the burner inlet. The temperature rises from 298 K to nearly 2000 K in approximately 0.8 mm. It is in this region that the fuel and the oxidizer first meet in stoichiometric proportion. In particular, it is clear from these figures that combustion occurs only in a thin region above the inlet. The methane and oxygen co-exist in only a very small region. Most of the methane disappears within 1.0 cm of the fuel jet. The resulting heat release produces an

extremely rapid rise in the temperature. As one moves in the direction of increasing r , we observe that the temperature rapidly decreases and ultimately approaches its inlet value. In addition, if we define the flame height as the first axial location where the maximum temperature occurs on the axis of symmetry, we obtain a flame height of approximately 7.0 cm.

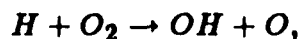
From a structural viewpoint, methane is the simplest hydrocarbon—it is the only hydrocarbon without a carbon-carbon bond. As a result, its oxidation differs significantly from other hydrocarbon fuels. Westbrook and Dryer [51] and Warnatz [52] have postulated that the oxidation of methane occurs through roughly two parallel paths. In one path carbon-hydrogen bonds are broken to form methyl radicals. The methyl radicals are then oxidized to methoxy radicals and/or formaldehyde. This is followed by the formation of the formal group which is then oxidized to form carbon monoxide. In the second path, methyl radical recombination is followed by the oxidation of the resulting C_2 species. In our calculations, the former path was chosen and the latter path was neglected.

In Figures 12-15 we illustrate isopleths for H_2O , CO , H_2 and CO_2 , respectively. Similar plots for CH_3 , OH and CH_2O are illustrated in Figures 16-18. It is clear from these figures that large quantities of H_2O , CO and H_2 are produced soon after the methane has been consumed. It is in this region that the methane is attacked by O , H and OH radicals and CH_3 is formed. In this region only small amounts of OH , H and O exist (see, e.g., Figure 17) due to the high affinity of methane for these radicals. The peak values of both CH_3 and CH_2O also occur after the methane has disappeared. The oxidation of CH_2O to HCO and the subsequent formation of CO occurs in regions of high methyl and formaldehyde concentrations.

The oxidation of CO to CO_2 proceeds primarily via the reaction



Hence, the rate of CO oxidation depends on the availability of OH radicals. However, as Westbrook and Dryer point out [51] the presence of most hydrocarbon species inhibits the oxidation of CO . This can be attributed to the fact that the rate of the reaction



is considerably smaller than the reaction rates of H atoms with hydrocarbon species and the rate of the CO oxidation reaction is also smaller than the reaction rates of hydrocarbon species with OH . As a result, small quantities of hydrocarbons can effectively restrict the oxidation of CO to CO_2 . Although carbon monoxide and hydrogen are found during the oxidation of the hydrocarbon species, it is not until after the hydrocarbons and the hydrocarbon fragments have been consumed that the OH level rises and CO_2 is formed. In Figure 17 we observe that in the axial direction the OH radical pool increases after the disappearance of the methane and the formation of CO . The CO is then oxidized to form CO_2 . Hence, in Figure 15 we observe that carbon dioxide forms downstream of the regions of high CH_3 , CH_2O and CO concentration.

From a fluid dynamic viewpoint, we find the velocities along the centerline to be higher than the values one would expect due to the effects of natural convection. In particular,

the stream function isopleths in Figure 19 illustrate two large recirculation cells that are established between the hot surface of the flame and the cooler shield. Air is entrained into the system at the shield outlet to balance the momentum of the inlet fuel and air streams along with the frictional losses at the shield wall. The presence of these recirculation cells reduces the total area available for the flow of the combustion gases and hence the velocities are increased due to the combined effects of natural convection and a reduced flow area.

It is worthwhile to reconsider Figure 8 in light of the recirculation cells. We note that the water vapor profile in Figure 8 asymptotes to a value of about one mole percent. (At a height of 5.0 cm above the burner this value asymptotes to about three mole percent). This is due to the fact that moist air was entrained into the system at the shield outlet. The moisture content of the air in the exit region of the shield was higher than in other portions of the laboratory. As a result, following Mitchell's [2] measurements, the inflow boundary conditions at the top of the shield in the recirculation zone were adjusted to account for the higher water vapor concentrations in the entrained air.

Unconfined Flame

The second flame we consider is an unconfined methane-air diffusion flame. The experimental configuration is such that the radius of the inner fuel jet $R_I = 0.2$ cm and the radius of the outer oxidizer jet $R_O = 2.54$ cm. Fuel is introduced through the center tube and air through the outer coflow. The boundary conditions at the inlet are given by

Inlet ($z = 0$):
 $r < R_I$

$$\begin{aligned} T &= 298 \text{ K}, \\ Y_{CH_4} &= 1.0, Y_k = 0, k \neq CH_4, \\ v_r &= 0.0 \text{ cm/sec}, \\ v_z &= 5.0 \text{ cm/sec}, \end{aligned} \tag{4.90}$$

$R_I < r < R_O$

$$\begin{aligned} T &= 298 \text{ K}, \\ Y_{O_2} &= .232, Y_{N_2} = .768, Y_k = 0, k \neq O_2, N_2, \\ v_r &= 0.0 \text{ cm/sec}, \\ v_z &= 25.0 \text{ cm/sec}. \end{aligned} \tag{4.91}$$

The appropriate boundary conditions for the stream function-vorticity system can be formed using the definition in (4.13) along with (4.22)-(4.23).

The flame sheet model again provided initial solution profiles for the stream function, the vorticity, the temperature and the major species, i.e., CH_4 , O_2 , N_2 , CO_2 and H_2O and the starting estimates for the minor species in the full chemistry solution were also approximated by Gaussian profiles that were centered at the location of the flame sheet on each axial level. The two-step solution procedure described in the confined flame problem

was used in solving the complete set of governing equations. The flame sheet and the first T_{OUT} calculation were performed on a 31×25 tensor product grid. The T_{OUT} solution was refined four times until a solution was obtained on a 65×38 grid. The total CPU time was comparable to the time required to obtain a solution for the confined flame.

From a chemical viewpoint, the flame is structurally similar to the confined flame discussed previously. In Figure 20 we illustrate the temperature isotherms for this system. We again observe extremely high temperature gradients directly above the burner inlet. The methane and oxygen co-exist in only a very small region. Most of the methane disappears within 1.0 mm of the fuel jet. Similarly, water, carbon monoxide and hydrogen are produced soon after the methane has been consumed. The oxidation of CO to CO_2 again proceeds primarily via the CO oxidation reaction and once the OH radical pool increases after the disappearance of the methane the CO is then oxidized to form CO_2 . The carbon dioxide forms downstream of the regions of high CH_3 , CH_2O and CO concentration.

In the confined flame the acceleration of the gases along the symmetric axis helped to produce a flame several cm in length. Without the additional acceleration near the axis of symmetry we obtain a much shorter flame. We compute a flame with a height of approximately 1.25 cm. Aside from the height of the two flames, the most dramatic difference between the confined and unconfined flames is in the fluid dynamic solution fields. In Figure 21 we illustrate the stream function for the unconfined flame. We observe that the streamlines indicate a bowing out of the flame above the inlet with a gradual movement of the flow towards the symmetric axis. No recirculation cell occurs in this configuration. Also, we observe in Figure 22 that there are two large vorticity cells that begin approximately 4.0 cm above the inlet and are centered approximately 0.5 cm from the axis of symmetry. These are the regions of highest counterclockwise rotation in the flame. Here the flow has a strong velocity component towards the axis of symmetry. This is in contrast to the region directly above the inlet where the vorticity is negative and the flow direction is such that there is a substantial radial component of the velocity causing the flame to "bow out". The negative vorticity region is limited to the area directly above the jets. At a height of approximately 1.0 mm above the inlet, the vorticity changes sign and the inward radial component of the velocity begins to increase. In the confined flame, due to the recirculation cells, the high vorticity region is located much closer to the symmetric axis.

4.2. Turbulent Flames

The final objective of our Phase II work plan is the incorporation of a $k - \epsilon$ turbulence model in our fluid dynamic-thermochemistry equations. The turbulent modeling capabilities of AXIJET lag behind the laminar modeling capabilities in terms of physical realism and robustness of the computational algorithm, even though they are close to the state of the engineering art. This is because: (a) turbulence is inherently a three-dimensional time-dependent phenomenon, with multiple space and time scales that are likely to remain computationally unresolvable for many years, even with optimistic extrapolations of computing power, and (b) two-dimensional time-averaged models of turbulent flows contain extra forms of coupling not found in laminar flow models which force Newton's method to proceed at such small implicit time-steps that less implicitly coupled techniques, when tameable, seem preferable, to date, in terms of computing resources.

A simple reminder of the inaccessibility of turbulent flow computations from first principles comes from a spatial scale argument. Let L be an integral length scale for a turbulent flow, say the diameter of a pipe bounding the flow, and let l be the scale of the smallest turbulent eddies requiring resolution (the Kolmogorov scale) in a direct Navier-Stokes simulation of the flow. Then $L/l = O(\text{Re}^{3/4})$, where Re is a Reynolds number based on the RMS of the fluctuating velocity components and the integral length scale. This can be related to a conventional pipe flow Reynolds number upon division by an average turbulence intensity, typically 1 to 10 percent. The number of mesh points required is $O((L/l)^3) = O(\text{Re}^{9/4})$. For a Reynolds number of 10^4 , this amounts to a billion grid points. The only satisfactory direct simulations of turbulent flows performed to date have been for Reynolds numbers of $O(10^2)$.

4.2.1. Problem Formulation

Given the general inadequacy of computational methods in the face of turbulence, it is preferable to modify the governing equation model to account in an approximate manner for the enhanced mixing that occurs in turbulent reacting flows, and its effects on the reaction, than to neglect turbulence completely. AXIJET-T incorporates a standard Favre-averaged $k - \epsilon$ flow model and a standard mixture-fraction-covariance model for the chemical reaction. The $k - \epsilon$ model reduces the evaluation of the turbulent stresses to a pair of fields which satisfy transport equations similar to those governing steady laminar flows. These are combined to generate local time and length scales for the turbulence. The mixture-fraction-covariance model reduces the evaluation of the local thermodynamic state of the flow to another pair of fields, denoted f and g herein, which also satisfy steady transport equations. Within AXIJET-T's $k - \epsilon - f - g$ formulation there are three main sub-hypotheses: an isotropic eddy viscosity, a β -function probability density function for the mixing of the fuel and oxidizer streams, and the laminar flamelet hypothesis. Discussion of these submodels is postponed until the following section.

Since AXIJET-T represents the flow field in terms of steady, time-averaged quantities, precise definition of the averaging employed is in order. For constant density flows, turbulence modeling is based on the decomposition introduced by O. Reynolds (1895) of a time-dependent field $\phi(\mathbf{x}, t)$ into a steady time-averaged part (denoted with an overbar) and a fluctuating part with zero mean (denoted with a prime):

$$\phi(\mathbf{x}, t) = \bar{\phi}(\mathbf{x}) + \phi'(\mathbf{x}, t)$$

where

$$\bar{\phi}(\mathbf{x}) = \lim_{T \rightarrow \infty} \frac{1}{T} \int_0^T \phi(\mathbf{x}, t) dt$$

For variable density flows, Reynolds averaging of the governing equations is inconvenient in that many correlations between density and other fields emerge. In combustion applications, the density may vary by an order of magnitude over the flow domain, so that these terms are non-negligible. The density-weighted time averaging introduced by Favre (1969) [53] overcomes this inconvenience for variable density flows (although it still requires modeling of triple correlations in the turbulent stress terms). The Favre decomposition

is written in terms of a density-weighted average (denoted with a tilde) and a fluctuating part with zero density-weighted mean (denoted with a double prime):

$$\phi(\mathbf{x}, t) = \tilde{\phi}(\mathbf{x}) + \phi''(\mathbf{x}, t)$$

where

$$\tilde{\phi}(\mathbf{x}) = \frac{1}{\bar{\rho}} \times \lim_{T \rightarrow \infty} \frac{1}{T} \int_0^T \rho \phi(\mathbf{x}, t) dt$$

The following simple relationship between Reynolds and Favre averages shows that they reduce to the same decomposition when density is constant:

$$\tilde{\phi} = \bar{\phi}(\mathbf{x}) + \overline{\rho' \phi'} / \bar{\rho}$$

In terms of Favre averages, the primitive variable governing equations in two-dimensional axisymmetry, and in the subsonic regime for which AXIJET is designed, are given by:
Continuity:

$$\frac{\partial}{\partial z}(\bar{\rho} \tilde{u}) + \frac{1}{r} \frac{\partial}{\partial r}(r \bar{\rho} \tilde{v}) = 0$$

Axial Momentum:

$$\frac{\partial}{\partial z}(\bar{\rho} \tilde{u} \tilde{u} + \overline{\rho u'' u''}) + \frac{1}{r} \frac{\partial}{\partial r}(r \bar{\rho} \tilde{v} \tilde{u} + \overline{r \rho v'' u''}) + \frac{\partial \bar{p}}{\partial z} + \frac{\partial \tau_{zz}}{\partial z} + \frac{1}{r} \frac{\partial}{\partial r}(r \tau_{zr}) = 0$$

Radial Momentum:

$$\frac{\partial}{\partial z}(\bar{\rho} \tilde{u} \tilde{v} + \overline{\rho u'' v''}) + \frac{1}{r} \frac{\partial}{\partial r}(r \bar{\rho} \tilde{v} \tilde{v} + \overline{r \rho v'' v''}) + \frac{\partial \bar{p}}{\partial r} + \frac{1}{r} \frac{\partial}{\partial r}(r \tau_{rr}) - \frac{\tau_{\theta\theta}}{r} + \frac{\partial \tau_{rz}}{\partial z} = 0$$

No gravity body force term is retained in the momentum equations because the large forced convective flow velocities and short convective time scales typical of turbulent applications render it insignificant.

The time-averaged molecular stress terms τ_{ij} are modeled by the usual Newtonian formulae in terms of time-averaged velocity gradients:

$$\begin{aligned} \tau_{zz} &= -\mu \left[2 \frac{\partial u}{\partial z} - \frac{2}{3} \nabla \cdot \mathbf{u} \right] \\ \tau_{rr} &= -\mu \left[2 \frac{\partial v}{\partial r} - \frac{2}{3} \nabla \cdot \mathbf{u} \right] \\ \tau_{\theta\theta} &= -\mu \left[2 \frac{v}{r} - \frac{2}{3} \nabla \cdot \mathbf{u} \right] \\ \tau_{rz} = \tau_{zr} &= -\mu \left[\frac{\partial u}{\partial r} + \frac{\partial v}{\partial z} \right] \end{aligned}$$

The triple-correlation turbulent stress terms are modeled by the usual Boussinesq hypothesis in analogy to the molecular stresses above:

$$\begin{aligned}\overline{\rho u'' u''} &= -\mu_t \left[2 \frac{\partial \bar{u}}{\partial z} \right] + \frac{2}{3} \bar{\rho} k \\ \overline{\rho v'' v''} &= -\mu_t \left[2 \frac{\partial \bar{v}}{\partial r} \right] + \frac{2}{3} \bar{\rho} k \\ \overline{\rho u'' v''} &= -\mu_t \left[\frac{\partial \bar{u}}{\partial r} + \frac{\partial \bar{v}}{\partial z} \right]\end{aligned}$$

The turbulent stress terms introduce a turbulent (or eddy) viscosity μ_t in analogy with the laminar (or molecular) viscosity μ . We note that the u and v required in the molecular stress terms are not available without additional modeling assumptions. However, the molecular stresses will be generally negligible in comparison with the turbulent stresses except near walls, since $\mu \ll \mu_t$. Therefore, we may use \bar{u} and \bar{v} in place of u and v in the molecular terms and sum the two stresses away from walls. In wall regions, the small errors thus committed are acceptable in view of our reliance upon standard constant density wall function approximations, themselves.

In terms of the Favre velocity fluctuations, we may define a specific turbulent kinetic energy

$$k = \frac{1}{2} (\widetilde{u''^2} + \widetilde{v''^2}) \quad [\text{units: } l^2 t^{-2}]$$

and a specific turbulent kinetic energy dissipation rate

$$\epsilon = \nu \left\{ 2 \left[\left(\frac{\partial \widetilde{u''}}{\partial z} \right)^2 + \left(\frac{\partial \widetilde{v''}}{\partial r} \right)^2 + \left(\frac{\widetilde{v''}}{r} \right)^2 \right] + \left(\frac{\partial \widetilde{v''}}{\partial z} + \frac{\partial \widetilde{u''}}{\partial r} \right)^2 \right\} \quad [\text{units: } l^2 t^{-3}]$$

The eddy viscosity will be specified in terms of k and ϵ , so the non-reacting turbulence model is closed by the following two transport equations:

Turbulent Kinetic Energy:

$$\frac{\partial}{\partial z} (\bar{\rho} \bar{u} k) + \frac{1}{r} \frac{\partial}{\partial r} (r \bar{\rho} \bar{v} k) - \frac{\partial}{\partial z} \left(\frac{\mu_e}{\sigma_k} \frac{\partial k}{\partial z} \right) - \frac{1}{r} \frac{\partial}{\partial r} \left(r \frac{\mu_e}{\sigma_k} \frac{\partial k}{\partial r} \right) = \Phi - \bar{\rho} \epsilon$$

Turbulent Kinetic Energy Dissipation Rate:

$$\frac{\partial}{\partial z} (\bar{\rho} \bar{u} \epsilon) + \frac{1}{r} \frac{\partial}{\partial r} (r \bar{\rho} \bar{v} \epsilon) - \frac{\partial}{\partial z} \left(\frac{\mu_e}{\sigma_\epsilon} \frac{\partial \epsilon}{\partial z} \right) - \frac{1}{r} \frac{\partial}{\partial r} \left(r \frac{\mu_e}{\sigma_\epsilon} \frac{\partial \epsilon}{\partial r} \right) = C_{\epsilon 1} \frac{\Phi \epsilon}{k} - C_{\epsilon 2} \frac{\bar{\rho} \epsilon^2}{k}$$

These equations require definition of diffusive transport coefficients in terms of the effective viscosity

$$\mu_e = \mu + \mu_t$$

and k and ϵ "Prandtl" numbers σ_k and σ_ϵ , which we take as standard fits from constant density wall-bounded shear flow experience with the model:

$$\sigma_k = 1.0$$

$$\sigma_\epsilon = 1.3$$

Each equation has a source term based on the local dissipation of the mean flow:

$$\Phi = \mu_t \left\{ 2 \left[\left(\frac{\partial \bar{u}}{\partial z} \right)^2 + \left(\frac{\partial \bar{v}}{\partial r} \right)^2 + \left(\frac{\bar{v}}{r} \right)^2 \right] + \left(\frac{\partial \bar{v}}{\partial z} + \frac{\partial \bar{u}}{\partial r} \right)^2 \right\} \quad [\text{units: } ml^{-1}t^{-3}]$$

and a corresponding sink term. Whereas the derivation of the k -equation rests on good theoretical grounds (at least for isotropic turbulence), the derivation of the ϵ -equation is weaker and relies on dimensional analysis and empirical fitting. The constants we employ in the source and sink term are again standard fits from the literature:

$$C_{\epsilon 1} = 1.47$$

$$C_{\epsilon 2} = 1.92$$

Note that ratio k/ϵ provides a characteristic temporal scale for the turbulence and $k^{3/2}/\epsilon$ a characteristic spatial scale.

We model the chemical composition of the reacting flow by means of a Favre-averaged mixture fraction, \tilde{f} , where $f(\mathbf{x})$ is defined as the fraction of the mixture at \mathbf{x} originating from the fuel stream, and hence varies from a value of 0 at the oxidizer inlet to 1 at the fuel inlet. An unambiguous definition of f can be made in terms of the local molecular composition, the molecular weight, and the atomic composition of each molecule involved in the reaction mechanism. For concreteness, an example based on a pure methane fuel stream and an oxygen/nitrogen oxidizer stream follows. Let there be K molecular species in a reaction mechanism, with molecular masses M_k and local mass fractions Y_k . Let $a_{k,C}$ denote the number of carbon atoms in the k^{th} molecule and $a_{k,H}$ the number of hydrogen atoms. Finally, let M_C and M_H denote the atomic masses of carbon and hydrogen. Then

$$f(\mathbf{x}) = \frac{\sum_{k=1}^K (a_{k,C} M_C Y_k(\mathbf{x}) / M_k) + \sum_{k=1}^K (a_{k,H} M_H Y_k(\mathbf{x}) / M_k)}{Y_{CH_4}}$$

Two particular values of f are of special interest, the asymptotic exit plane value

$$f_{\text{exit}} = \frac{1}{1 + \dot{m}_O / \dot{m}_F}$$

and the stoichiometric value

$$f_{St} = \frac{1}{1 + (\nu_O M_O / \nu_F M_F)}$$

where \dot{m}_F and \dot{m}_O are the integrated mass fluxes of fuel and oxidizer, ν_F and ν_O their stoichiometric coefficients (adjusted, if necessary, for the fact that either stream may contain a nonzero amount of inert), and M_F and M_O their molecular masses.

Under the assumption that all state variables of the flow are functions of f , solution of a source-free transport equation for f describes the complete thermodynamic state of the mixture. However, because of the underlying turbulence, it is unreasonable to assume that $f(\mathbf{x})$ is a deterministic function, and it is typically modeled as a random function governed by some Favre probability density function $\tilde{P}(f)$. Therefore, any state variable or function thereof (such as temperature or viscosity) is derivable as a probability integral over the domain of allowable values of f :

$$\bar{\phi} = \int_0^1 \phi(f) \tilde{P}(f) df$$

The density is the lone exception to this formula, because of the density-weighted averaging employed. The appropriate formula is instead:

$$\frac{1}{\bar{\rho}} = \int_0^1 \frac{1}{\rho(f)} \tilde{P}(f) df$$

Evaluation of $\tilde{P}(f)$ typically requires a set of moments of f . The simplest schemes involve only one higher moment, the Favre covariance, denoted g and defined by:

$$g = (\tilde{f''})^2$$

where $f'' = f - \bar{f}$. The specific choice of \tilde{P} enters only into a free-standing module bundled with AXIJET-T, which in turn affects the main AXIJET-T code only through a data file giving the state functions necessary to advance the calculation in terms of \bar{f} and g .

The Favre-averaged mixture fraction satisfies the following homogeneous equation:
Mixture Fraction:

$$\frac{\partial}{\partial z} (\bar{\rho} \tilde{u} \bar{f}) + \frac{1}{r} \frac{\partial}{\partial r} (r \bar{\rho} \tilde{v} \bar{f}) - \frac{\partial}{\partial z} \left(\frac{\mu_e}{\sigma_f} \frac{\partial \bar{f}}{\partial z} \right) - \frac{1}{r} \frac{\partial}{\partial r} \left(r \frac{\mu_e}{\sigma_f} \frac{\partial \bar{f}}{\partial r} \right) = 0$$

The mixture fraction covariance satisfies a modeled equation similar in structure to the ϵ equation:

Covariance of Mixture Fraction ("Unmixedness"):

$$\frac{\partial}{\partial z} (\bar{\rho} \tilde{u} g) + \frac{1}{r} \frac{\partial}{\partial r} (r \bar{\rho} \tilde{v} g) - \frac{\partial}{\partial z} \left(\frac{\mu_e}{\sigma_g} \frac{\partial g}{\partial z} \right) - \frac{1}{r} \frac{\partial}{\partial r} \left(r \frac{\mu_e}{\sigma_g} \frac{\partial g}{\partial r} \right) = C_{g1} \Phi_g - C_{g2} \frac{\bar{\rho} g \epsilon}{k}$$

As with the $k - \epsilon$ pair, modeling constants are required, two "Prandtl numbers":

$$\sigma_f = 0.6$$

$$\sigma_g = 0.6$$

and source and sink term coefficients, for which we employ the fits:

$$C_{g1} = 2.8$$

$$C_{g2} = 2.0$$

The source term Φ_g consists of squares of gradients of \tilde{f} , in analogy to the mean dissipation term of the $k - \epsilon$ model:

$$\Phi_g = \mu_t \left[\left(\frac{\partial \tilde{f}}{\partial r} \right)^2 + \left(\frac{\partial \tilde{f}}{\partial z} \right)^2 \right] \quad [\text{units: } ml^{-3}t^{-1}]$$

4.2.2. Transport and Chemistry Model

The transport and chemistry model consists of three independent models: a set of deterministic state functions of mixture fraction, a probability density function with which these are weighted in constructing the mean properties, and a formula for the enhanced mixing due to the turbulence in the form of μ_t .

For the first, an assumption of thermo-chemical equilibrium is often assumed in the literature, as matter of convenience in view of the ignorance of finite-rate kinetics. Though an equilibrium-based data file can be prepared for the methane-air flame demonstrated in the results section below, we employ instead a primitive laminar flamelet hypothesis, which takes advantage of our earlier work in the modeling of finite-rate methane-air flames. The laminar flamelet model is based on a picture of a turbulent flame front as a convoluted ensemble of laminar flamelets - counterflowing diffusion flames, to be precise. The local composition is taken to the composition of the corresponding diffusion flame at the same value of the mixture fraction. Refinements to the laminar flamelet model take into account variations in the local fluid rate of strain. This capability is not incorporated into the present version of AXIJET-T.

Because of the way AXIJET-T is formulated above, knowledge of most state variables is not needed to advance the calculation; only density and viscosity are needed at each intermediate iteration. Consequently, the evaluation of the temperature and mass fractions of various species can be deferred to a post-processing step.

Plots of density and viscosity as a function of mixture fraction are given in Figures 23 and 24 following and a plot showing the temperature and the two major reactants is given in Figure 25. The data comes from the Tsuji flame configuration solved in [54]. Note that for this particular flame, the stoichiometric value of f is 0.0551, and this is where the peak of the temperature profile (also the trough of the density profile) sits.

For the second model, namely the probability density function for f , "clipped Gaussians" or Incomplete Beta functions are often used. The latter is built into the AXIJET preprocessor. Its definition is

$$P(f) = \frac{f^{a-1}(1-f)^{b-1}}{\int_0^1 f^{a-1}(1-f)^{b-1} df}, \quad (4.92)$$

where the exponential parameters are derived from the Favre mean and covariance:

$$a = \tilde{f} \left[\frac{\tilde{f}(1 - \tilde{f})}{g} - 1 \right], \quad b = (1 - \tilde{f}) \left[\frac{\tilde{f}(1 - \tilde{f})}{g} - 1 \right]. \quad (4.93)$$

It is readily verified for $a > 0$ and $b > 0$ that \tilde{P} satisfies the basic properties of a probability density function over the interval $(0, 1)$: it is non-negative and has a unit integral over the complete interval. Note that g must be confined to the range $0 < g < \tilde{f}(1 - \tilde{f})$ for this to be true. Very small values of g lead to delta-function-like peaked distributions at the endpoints, and $g = 0$ represents certainty that the flow is in the state characterized by \tilde{f} . Large values of g lead to Gaussian-like distributions about \tilde{f} . Some sample plots of \tilde{P} for different \tilde{f} and g are contained in Appendix A. Appendix A also addresses some fine points in the numerical quadrature of integrals containing β -functions.

We follow standard practice in adopting for our third model an isotropic turbulent viscosity coefficient

Turbulent Viscosity:

$$\mu_t = C_\mu \bar{\rho} k^2 / \epsilon \quad [\text{units: } ml^{-1}t^{-1}]$$

which contains another fitted parameter:

$$C_\mu = 0.09$$

4.2.3. Boundary Conditions and Wall Functions

Discussion in this section is patterned after the geometry that is presently hard-coded into the release copy of AXIJET-T, namely that of a two-fluid jet with a coaxial coplanar inlet boundary upstream, adiabatic no-slip bounding walls, and an outflow boundary. (Figure 26 applies equally well in this section.) An (z, r) coordinate system is adopted with its origin at the center of the inlet plane and key dimensions as follows. The radius of the cylindrical fuel jet is r_{in} and the outer radius (which is the same as that of the annular oxidizer jet) is r_{out} . The outflow is at z_{out} . In describing phenomena in the wall region, a local coordinate system is also adopted at wall boundaries in which y is a normal coordinate with its origin at the wall itself, and u_\perp and u_\parallel are the local normal and tangential velocities, respectively.

Due to radial symmetry, only half of an (z, r) plane need be considered. Thus four types of boundaries are discussed in conjunction with the particular geometry currently in AXIJET-T: inflow, outflow, symmetry and wall. These are the same types likely to be required in most future applications of AXIJET-T, except possibly for permeable wall boundaries (along which $u_\parallel = 0$, but $u_\perp \neq 0$) and nonadiabatic wall boundaries. We begin with wall boundaries, because they are both key and problematic features in turbulence modeling, and because results from the wall boundaries are subsequently used at inlet boundaries as well. From this subsection onward, all tilde notation of the Favre averaging is dropped but implicitly understood.

4.2.3.1. Wall Boundaries

Wall boundary conditions along an impermeable no-slip surface are straightforward, namely $u_{\parallel} = u_{\perp} = 0$, whence $k = \epsilon = 0$. If the wall is adiabatic, we also have that $\frac{\partial f}{\partial n} = 0$ and $g = 0$. In the history of the numerical simulation of high Reynolds number turbulent flows it has often been difficult for economic reasons to resolve the wall boundary layer sufficiently well for these straightforward boundary conditions to be applied without severely contaminating the accuracy of the solution outside of the layer. Furthermore, the process of resolving the wall region accurately enough to capture the normal gradients, inevitably introduces large numbers of points in the low Reynolds number region near the wall, which increases the volume of computational work required. Furthermore, in the low Reynolds number regions, the $k - \epsilon$ model, and the resulting estimate for μ_t are invalid, and must be replaced with additional local assumptions anyway.

Therefore, it is customary to look to empirical fits of experimental data to interpolate between the bulk high Reynolds number turbulent flow and the no-slip wall. This practice is complicated by the fact that the bulk flow depends on the field variables at the outer edge of the wall function region, and the parameters of the wall functions are defined in terms of the bulk flow – the patching process must be implicitly handled. (This requirement for implicitness is no different a situation than that encountered in enforcing a system of elliptic PDEs without wall functions all the way to the wall, but it complicates the coding in that a *transition region* in which both sets of formulae apply must be determined in order for the solution process to go forward.)

The most convenient links by which the patching process is mediated are the shear stress at the wall, denoted herein by τ_w , and the “friction velocity”, denoted U_τ and defined in terms of τ_w by $U_\tau = \sqrt{\tau_w/\rho_w}$. These are used to define a host of nondimensional quantities as follows:

$$\begin{aligned} y^+ &\equiv \frac{yU_\tau}{\nu_w} \\ u^+ &\equiv \frac{u_{\parallel}}{U_\tau} \\ k^+ &\equiv \frac{k}{U_\tau^2} \\ \epsilon^+ &\equiv \frac{\epsilon\nu_w}{U_\tau^4} \end{aligned}$$

The first of these quantities, y^+ , is used to divide the domain into three layers, according to classical turbulent flow taxonomy (the transitions between these layers are approximate.) The laminar (or Couette) layer is $0 < y^+ < 12$; the log layer is $12 < y^+ < 300$; and the outer layer is $y^+ > 300$. The values of k and ϵ at grid points at and near the wall will depend on the location of the grid points in terms of y^+ . (We note that the physical locations (in y) a fixed y^+ change as the flow evolves, since y^+ depends on the local shear stress at the wall, which varies with bulk flow conditions.) The “law”

$$u^+ = \frac{\ln y^+}{\kappa} + B,$$

in which $\kappa = 0.42$ and $B = 5.5$, holds in the log layer and constitutes a transcendental equation for U_r , which may be solved by iteration at any point in the layer. Having determined the dimensionless normal distance, we are able to complete the following scheme:
Parallel Velocity:

$$u^+ = \begin{cases} y^+, & \text{if } y^+ \leq 12 \\ \ln y^+ / \kappa + B, & \text{if } y^+ \geq 12 \end{cases} \quad (4.94)$$

Specific Turbulent Kinetic Energy:

$$k^+ = \begin{cases} 0.05(y^+)^2, & \text{if } y^+ \leq 5 \\ 1.25 + 0.325(y^+ - 5), & \text{if } 5 < y^+ \leq 15 \\ 4.5 - (y^+ - 15)/37.5, & \text{if } 15 < y^+ \leq 60 \\ 3.3, & \text{if } 60 < y^+ \leq 200 \end{cases} \quad (4.95)$$

Specific Dissipation Rate of Turbulent Kinetic Energy:

$$\epsilon^+ = \begin{cases} 0.1 + y^+ / 120, & \text{if } y^+ \leq 12 \\ 1 / (\kappa y^+), & \text{if } y^+ > 12 \end{cases} \quad (4.96)$$

The log law is illustrated in Figure 27 and these fits for k^+ and ϵ^+ in Figures 28 and 29.

One final feature of the wall function technique is the Van Driest formula for μ_t within the log layer:

Wall Region Turbulent Viscosity:

$$\mu_t = \frac{\mu}{2} (\sqrt{1 + 4a^2} - 1) \quad (4.97)$$

where

$$a = \kappa y^+ (1 - e^{-y^+ / A^+}),$$

in which $A^+ = 26.7$.

4.2.3.2. Inflow Boundaries

Generally, normal and tangential mean velocities, as well as density are available at inflow boundaries. In multicomponent problems, the mixture fraction f is often known with precision in inlet streams, in which case its covariance, g , is zero. In the absence of measured data, specific turbulence kinetic energy can be hypothesized to be a fraction of the specific mean kinetic energy, $k = c(u_{\parallel}^2 + u_{\perp}^2)$ (c is dimensionless). Again, in the absence of superior information, a constant turbulence length scale hypothesis yields $\epsilon = k^{3/2} / l$ (l has dimensions of length). We use these formulae towards the middle of the inlets, as described below, assuming that the inlet profiles are themselves well developed. We choose the constants by grafting them onto boundary layer formula at the inlet edges. Hence, all inflow data are Dirichlet.

In the case at hand, the inlets are $z = 0$, $0 < r < r_{in}$ (cylindrical fuel inlet, subscript F) and $z = 0$, $r_{in} < r < r_{out}$ (annular oxidizer inlet, subscript O).

For fully-developed turbulent flow, we have, away from the wall regions:

Velocities:

$$v_r = 0$$

$$v_z = v_{F,max} \left(\frac{r_{in} - r}{r_{in}} \right)^{1/7}, \quad 0 < r < r_{in}$$

$$v_z = v_{O,max} \left(\frac{r - r_{in}}{\lambda r_{out} - r_{in}} \right)^{1/7}, \quad r_{in} < r < \lambda r_{out}$$

$$v_z = v_{O,max} \left(\frac{r_{out} - r}{r_{out} - \lambda r_{out}} \right)^{1/7}, \quad \lambda r_{out} < r < r_{out}$$

where the maxima at $r = 0$ and $r = \lambda r_{out}$ are given by

$$v_{F,max} = \left(\frac{60}{49} \right) v_F$$

$$v_{O,max} = \left(\frac{60}{49} \right) \frac{1}{1 + \lambda / (7(1 + r_{in}/r_{out}))} v_O$$

where v_F and v_O are the fuel and oxidizer mass fluxes divided by the inlet densities and areas, and $\lambda = \sqrt{\frac{1 - (r_{in}/r_{out})^2}{2 \ln(r_{out}/r_{in})}}$.

By equating these expressions for the parallel velocity components away from the inlet walls with log law velocity profiles at a given matching value of y^+ , we may deduce the local friction velocity U_τ at each of the three inlet walls, r slightly less than r_{in} in the fuel jet, r slightly greater than r_{in} in the oxidizer jet, and r slightly less than r_{out} in the oxidizer jet. From these values of U_τ , the axial velocity profiles can be corrected near the wall through (4.94). A value of about 200 for y^+ is reasonable for this matching. Because of the wall correction to the $1/7^{\text{th}}$ power law velocity distribution, the mass flux through each inlet will be slightly reduced from the design mass fluxes, from which $v_{O,max}$ and $v_{F,max}$ are initially calculated under the assumption of a full profile. It is therefore advisable to renormalize the velocity distribution once it is in final shape. (In typical applications, this effect is 2% or less, and the process is not iterated.)

Since U_τ is known, k , ϵ and μ_t can be set in each wall inlet layer by means of (4.95) through (4.97). This process provides three sets of values of k and ϵ at $y^+ = 200$ which can then be used to determine the constants c and l in the sets of formulae
Specific Turbulent Kinetic Energy:

$$k = cv_x^2$$

Specific Rate of Dissipation of Turbulent Kinetic Energy:

$$\epsilon = \frac{k^{3/2}}{l}$$

Of course, since the annular inlet provides a matching at both sides, the constants c and l may be slightly different when fit independently from either side. In practice, this discrepancy should be modest but it is, in any event, dispensed with by calculating the k and ϵ distributions from both ends and blending them linearly in the middle.

Finally we have the inlet conditions for the $f - g$ submodel:
Mixture Fraction:

$$f = \begin{cases} 1, & \text{if } 0 < r < r_{in} \\ f_{St}, & \text{if } r = r_{in} \\ 0, & \text{if } r_{in} < r < r_{out} \end{cases} \quad (4.98)$$

Covariance of Mixture Fraction:

$$g = 0$$

4.2.3.3. Outflow Boundaries

The outflow boundary is assumed to be far enough downstream that zero gradient conditions can be imposed on the radial momentum, and all other field variables except the axial momentum. The flow is overconstrained by a zero gradient condition on the axial momentum which translates through the continuity equation and the lateral boundary conditions to a statement that $v_r = 0$. Therefore, the axial momentum is required to satisfy the less stringent condition of zero curvature. In the case at hand, the outlet is $z = z_{out}$, $0 < r < r_{out}$. We have:

Velocities:

$$\frac{\partial(\rho v_r)}{\partial z} = 0$$

$$\frac{\partial^2(\rho v_z)}{\partial z^2} = 0$$

All other variables ϕ :

$$\frac{\partial \phi}{\partial z} = 0$$

4.2.3.4. Symmetry Boundaries

On a symmetry boundary the fields satisfy zero-normal gradient conditions. In addition, the velocity normal to the symmetry boundary must be zero by continuity. We have:

Normal velocity, v_r :

$$v_r = 0$$

All other variables ϕ :

$$\frac{\partial \phi}{\partial r} = 0$$

4.2.4. Initial Conditions

It is useful to calculate outflow parameters based on the assumption of fully developed turbulent outflow profiles, since this provides information which can be used in constructing an initial iterate by axial interpolation of inlet and outlet streams. For this purpose, we assume a fully developed outflow and construct an axial velocity in direct geometric analogy to the fuel inlet, except that the radius is different and the mass flux is, of course, the sum of that of both inlet streams. As at the inlet, we assume that $g = 0$, and we set $f = f_{exit}$ at all r . All fields except for k and ϵ are then linearly interpolated in z between inlet and exit. Consulting the state relationship of $\rho(f)$ provides a global estimate for the density. It is then possible to construct an estimate for the axial momentum ρv_z at all points, and thereby of the integrated axial mass flux at each station. Since these mass fluxes by station must match the sum of the inlet fluxes, the velocity profiles are normalized by the ratio of fluxes in an approximate attempt to begin the calculation with a flow field which is axially non-divergent.

The turbulence parameters are set at their lower bounds everywhere except at the inlets in the initial estimate, so that the flow effectively begins as a laminar one. Linear interpolation between assumed turbulence profiles at the inlet and outlet stations was attempted and found highly unsatisfactory because in typical applications turbulent "hot spots" tend to be localized in the axial coordinate, are thus poorly approximated by a monotonic interpolation between the inlets. Furthermore, their appearance in several "guessed" source/sink terms pulls the flow in several directions at the outset, which confuses the solution algorithm in its initial pressure equilibration progress.

4.2.5. Computational Approach

AXIJET-T is basically a SIMPLER (Semi-Implicit Method for Pressure-Linked Equations - Revised) algorithm after Patankar [55] based on a staggered-grid Finite Analytic discretization of the governing equations after Chen and Chen [56] (see also [57] for a turbulent flow application). The major refinement over a conventional SIMPLER implementation is the use of a direct solver, YSMP (Yale Sparse Matrix Package [58]) to handle the pressure and pressure correction equations without iteration. We repeat that all tilde notation of the Favre averaging is dropped, since the algorithm applies equally well to any physical formulation which fits into the generic five-point transport operator on a staggered grid.

As applied to the extended system of field equations (for $u(=v_x)$, $v(=v_r)$, p , k , ϵ , f , and g), and algebraic relationships (for ρ , μ , and μ_t), the SIMPLER algorithm has the following form (consult [55] for the well-documented details). The roles of the linearized velocity components u and v at each iteration are played by two sets of fields: "pseudo-velocities" (\hat{u} and \hat{v}) which satisfy the discrete momentum equations without the pressure gradient terms, and "true" velocities which satisfy the full momentum equations, albeit based on a provisional pressure. Similarly, the pressure is decomposed into two fields: a provisional pressure (p^*) which satisfies the Poisson equation obtained by taking the divergence of the momentum equations with the source term computed based on the pseudo-velocities only, and a pressure correction (p') based on the same discrete Poisson operator, but with the "true" velocities used in computing the source term. As implemented in AXIJET-T, it takes the following form:

The "SIMPLER" Algorithm

- (0) Specify $u^k, v^k, (p^*)^k$, etc., at iteration index $k = 0$
 - (1) Solve linearized momentum eqns. for temporary velocities u^*, v^*
 - (2) Solve pressure-correction eqn. for $(p')^{k+1}$
 - (3) Solve velocity-correction eqns. for u^{k+1}, v^{k+1} , using $(p')^{k+1}$
 - (4) Solve pressure-free momentum eqns. for \hat{u}, \hat{v}
 - (5) Solve for provisional pressure $(p^*)^{k+1}$
 - (6) Solve linearized conservation eqns. for other fields
 - (7) Update state and transport properties
 - (8) If converged, STOP
 - (9) $k \leftarrow k + 1$; go to (1)
-

The cycle (1-9) is ordered differently from the original version of SIMPLER in two ways. In the original, Steps (6) and (7) immediately follow step (3). The two orderings are nearly equivalent, however, since the only fields modified between steps (3) and (6) are the pseudo-velocities and the pressure, on which none of the other field variables depend, and the dependence of the coefficients of the equations used in steps (4) and (5) upon the other fields may be suppressed anyway, to avoid recomputation. Apart from the unimportant difference in the cyclic order, the cycle begins at a different stage in the original, namely at our step (4).

Each of stages (1) through (6) involves solving large sparse linear systems of algebraic equations for the discrete unknowns. The equations arising in (2) and (4) are solved by direct Gauss elimination, which incurs a large storage overhead, but should be regarded as a minimum step in the direction of implicitness for SIMPLE-type algorithms on large grids, over which relaxation methods are too inefficient to be worth the storage savings. The other systems are solved by block line Gauss-Seidel, sweeping in the convective direction. Sweeps are repeated until the residuals of the linearized discrete equations for each field in turn satisfy an absolute convergence criterion. This criterion is set stringently in the release version of AXIJET, since typically only a handful of sweeps are necessary in combination with the below-mentioned implicit time-stepping. Introduced for nonlinear stability, it has the side-effect of providing diagonal dominance which enhances the efficiency of the relaxation sweeps.

In an effort to control the notorious instability of the SIMPLER class of algorithms in the presence of a variable density $k - \epsilon$ model, AXIJET incorporates sink-term-linearization in the k, ϵ and g equations, and implicit time-stepping in all equations except for the Poisson pressure equation. In addition, "filtering" is performed, if necessary, once each cycle through the SIMPLER loop to: (a) bound the k and ϵ fields away from zero or negative values, by clipping them into the interval $[10^{-10}, \infty)$ (b) clip the f and g fields into their doubly bounded intervals of $[0, 1]$ and $[0, f(1 - f)]$, respectively. While doing

the filtering, the code checks that the outflow boundary is truly an outflow (i.e., that $v_z(z_{out}) > 0$). (A warning message is printed if this condition fails, but no corrective action is taken, since it is likely a symptom of invalid placement of an outflow boundary if it persists.)

Dirichlet boundary conditions are explicitly incorporated into the governing equation set, while the Neumann symmetry conditions are handled by solving a discrete form of the governing equations on the axis itself, by means of defining a row of auxiliary boundary cells "below" the symmetry axis. Neumann outflow conditions are incorporated by solving discrete equations up to the penultimate station and extrapolating the unknowns of the final station.

The wall functions are enforced in a region near $r = r_{out}$, $0 < z < z_{out}$ by explicitly overwriting the k , ϵ , μ_t and v_z fields in the last few discrete rows. (The exact number of rows is a user-specifiable parameter). The transcendental equation for U_r is solved by a Newton-Raphson iteration at each station at each iteration. The transverse extent of the "swept" region solved by the block-line Gauss-Seidel algorithm is truncated away from the wall region for the k and ϵ fields, since the governing equations from which the discretizations are derived are not valid in this low Reynolds number region.

Discretization of the governing partial differential equations is performed with the Finite Analytic method, which may be thought of, as far as the structure of its discrete operator is concerned, as an interpolated-upwinding Finite-Difference scheme. Like a lowest-order primitive variable Finite-Difference scheme for this set of governing equations, it makes use of a five-point stencil. However, instead of using Finite-Difference formulae, the Finite Analytic method solves *exactly* the piecewise constant coefficient problems associated with each cell of the domain over which the governing equation is defined. The relations between neighboring degrees of freedom are, in effect, matching conditions for the solutions continuously defined over each cell.

The system of governing equations described throughout this section for use in modeling the turbulent reactor could be solved, after transformation to streamfunction-vorticity form to eliminate the continuity equation, by exactly the same type of fully-implicit modified Newton solver employed in AXIJET-L. The wall function formalism is slightly different under this transformation in that the solution of the transcendental equation for the wall shear stress (or equivalently, for the friction velocity) involves integral evaluations when expressed in terms of streamfunction. It was originally intended that AXIJET-L and AXIJET-T employ the same solver, and simply have different residual evaluation routines. However, this uniformity was not preserved in the final product in favor of a more conservative scheme (in terms of resemblance to other state of the art codes) for AXIJET-T. Apart from the minor convenience of handling the turbulence wall functions in primitive variables, the main reasons for delivering a field-by-field decoupled primitive variable version were: difficulties with the k and ϵ equations inside of the Newton loop, the strongly convection dominated character of turbulent flows (as opposed to the more elliptic character of lower Reynolds number laminar flows), which makes the decoupling penalty less significant in this regime, and the inconvenience of the special conditionals required to handle the upper-bounded fields of f and g in the Jacobian matrix evaluation routine of the AXIJET-L solver. The nonlinear source terms of the k and ϵ equations are

not in and of themselves worse than the Arrhenius-type source terms successfully handled by a damped-modified Newton method in AXIJET-L. However, the mean-flow dissipation terms (represented by Φ) represent a new spatial coupling between the mean momentum and turbulence equations which is likely at least part of the difficulty, especially since the required velocity gradients strongly involve the "corner points" of the nine-point discrete stencil. In practice, Newton's method was forced to proceed along such tiny time-steps when given a "reasonably" constructable initial estimate for the solution iterate that the SIMPLER-type scheme was superior in some tests of non-reacting flows. Ultimately, for large numbers of species per gridpoint, Newton's implicit advantages must prevail over segregated algorithms, and may yet prevail even at modest numbers of species such as the current AXIJET-T, but this is left to future research.

One advancement of the state of the art in primitive variable solvers is available which is not included in the current version of AXIJET-T: namely fully implicit velocity-pressure coupling, as advocated by, *e.g.*, Vanka [59]. We have successfully tested a fully implicit velocity-pressure algorithm employing a direct solver and Newton's method on a laminar non-reacting flow problem, but this is not yet incorporated into the $u - v - p$ portion of AXIJET-T. We do, however, overcome one of the prime inefficiencies of the semi-implicit velocity-pressure coupling of the SIMPLER algorithm, in that we do employ a direct (sparse) solver for the pressure and pressure-correction equations.

4.2.6. Computational Results

We show in this section results from three problems run using AXIJET-T which are small enough to run on a microVAX: a non-reacting flow in the design configuration of two coaxial jets, a reacting flow in the same configuration, and a reacting flow in an alternate configuration with one axial and one radial inlet.

The former illustrates the example in the AXIJET-T User's Guide, a typical laboratory configuration comprised of a higher-speed narrow methane fuel jet ($v_F = 8.23$ m/s, $r_{in} = 1.0$ cm, $T = 332$ K) and a low-speed wide oxidizer stream of standard atmospheric composition ($v_O = 0.67$ m/s, $r_{in} = 10$ cm, $T = 283$ K). The inlet conditions were chosen to be in stoichiometric balance and to produce an exit Reynolds number based on the diameter of 10^4 , which implies for these dimensions and inlet conditions a fuel inlet Reynolds number of 7,779 and an oxidizer inlet Reynolds number of 9,328. The exit is at $z_{out} = 1.5$ m, or 15 radii, downstream.

A little less than 1 hr of MicroVAX time was required to obtain the solution depicted in Figures 30 through 33 on a fairly coarse grid (30×25), using a more conservative (and thus less efficient) than necessary time-step strategy in which an initial step of 10^{-3} was increased in steps to 10^{-1} . The solution is not yet grid-independent at this resolution, but the problem provides an adequate test of the algorithmic working of the code. The second, on the same grid, is under-resolved like the first, given the sharp density differences of hydrocarbon combustion, but is included as a companion test problem involving the non-monotonic-with- f state relationship characteristic of hydrocarbon-air flames. Its solution (also requiring under an hour of MicroVAX time, under the same time-stepping strategy) is represented in Figures 34 through 36. The same exit Reynolds number of 10^4 requires a greater inlet mass fluxes due to the high viscosity and low density of the hot burned mixture. The inlet velocities are $v_F = 30.94$ m/s and $v_O = 2.53$ m/s, leading to Reynolds

numbers of 29,231 for the fuel and 35,051 for the oxidizer.

Reference to a third problem is included briefly in the report, but not in the User's Guide because it represents a *custom* application of AXIJET-T to a very difficult problem in the oxidation of a metallic chloride in heated air. The extreme density ratio in the problem is about 15.6, which is roughly twice the ratio of atmospheric methane-air flames, and there is a large recirculation region tucked out of the way of two cross-jets. A streamline and temperature plot are given in Figures 37 and 38. The resolution of the solutions pictured is 90×60 , which has been shown to provide grid-independence for all functionals of engineering interest.

TABLE 1

Reaction Mechanism Rate Coefficients In The Form $k_f = AT^\beta \exp(-E_0/RT)$.
Units are moles, cubic centimeters, seconds, Kelvins and calories/mole.

	REACTION	A	β	E
1.	$CH_4 + M \rightleftharpoons CH_3 + H + M$	1.00E+17	0.000	86000.
2.	$CH_4 + O_2 \rightleftharpoons CH_3 + HO_2$	7.90E+13	0.000	56000.
3.	$CH_4 + H \rightleftharpoons CH_3 + H_2$	2.20E+04	3.000	8750.
4.	$CH_4 + O \rightleftharpoons CH_3 + OH$	1.60E+06	2.360	7400.
5.	$CH_4 + OH \rightleftharpoons CH_3 + H_2O$	1.60E+06	2.100	2460.
6.	$CH_2O + OH \rightleftharpoons HCO + H_2O$	7.53E+12	0.000	167.
7.	$CH_2O + H \rightleftharpoons HCO + H_2$	3.31E+14	0.000	10500.
8.	$CH_2O + M \rightleftharpoons HCO + H + M$	3.31E+16	0.000	81000.
9.	$CH_2O + O \rightleftharpoons HCO + OH$	1.81E+13	0.000	3082.
10.	$HCO + OH \rightleftharpoons CO + H_2O$	5.00E+12	0.000	0.
11.	$HCO + M \rightleftharpoons H + CO + M$	1.60E+14	0.000	14700.
12.	$HCO + H \rightleftharpoons CO + H_2$	4.00E+13	0.000	0.
13.	$HCO + O \rightleftharpoons OH + CO$	1.00E+13	0.000	0.
14.	$HCO + O_2 \rightleftharpoons HO_2 + CO$	3.00E+12	0.000	0.
15.	$CO + O + M \rightleftharpoons CO_2 + M$	3.20E+13	0.000	-4200.
16.	$CO + OH \rightleftharpoons CO_2 + H$	1.51E+07	1.300	-758.
17.	$CO + O_2 \rightleftharpoons CO_2 + O$	1.60E+13	0.000	41000.
18.	$CH_3 + O_2 \rightleftharpoons CH_3O + O$	7.00E+12	0.000	25652.
19.	$CH_3O + M \rightleftharpoons CH_2O + H + M$	2.40E+13	0.000	28812.
20.	$CH_3O + H \rightleftharpoons CH_2O + H_2$	2.00E+13	0.000	0.
21.	$CH_3O + OH \rightleftharpoons CH_2O + H_2O$	1.00E+13	0.000	0.
22.	$CH_3O + O \rightleftharpoons CH_2O + OH$	1.00E+13	0.000	0.
23.	$CH_3O + O_2 \rightleftharpoons CH_2O + HO_2$	6.30E+10	0.000	2600.
24.	$CH_3 + O_2 \rightleftharpoons CH_2O + OH$	5.20E+13	0.000	34574.
25.	$CH_3 + O \rightleftharpoons CH_2O + H$	6.80E+13	0.000	0.
26.	$CH_3 + OH \rightleftharpoons CH_2O + H_2$	7.50E+12	0.000	0.
27.	$HO_2 + CO \rightleftharpoons CO_2 + OH$	5.80E+13	0.000	22934.
28.	$H_2 + O_2 \rightleftharpoons 2OH$	1.70E+13	0.000	47780.
29.	$OH + H_2 \rightleftharpoons H_2O + H$	1.17E+09	1.300	3626.
30.	$H + O_2 \rightleftharpoons OH + O$	2.20E+14	0.000	16800.

TABLE 1 (continued)

Reaction Mechanism Rate Coefficients In The Form $k_f = AT^\beta \exp(-E_0/RT)$.
Units are moles, cubic centimeters, seconds, Kelvins and calories/mole.

	REACTION	A	β	E
31.	$O + H_2 \rightleftharpoons OH + H$	1.80E+10	1.000	8826.
32.	$H + O_2 + M \rightleftharpoons HO_2 + M^a$	2.10E+18	-1.000	0.
33.	$H + O_2 + O_2 \rightleftharpoons HO_2 + O_2$	6.70E+19	-1.420	0.
34.	$H + O_2 + N_2 \rightleftharpoons HO_2 + N_2$	6.70E+19	-1.420	0.
35.	$OH + HO_2 \rightleftharpoons H_2O + O_2$	5.00E+13	0.000	1000.
36.	$H + HO_2 \rightleftharpoons 2OH$	2.50E+14	0.000	1900.
37.	$O + HO_2 \rightleftharpoons O_2 + OH$	4.80E+13	0.000	1000.
38.	$2OH \rightleftharpoons O + H_2O$	6.00E+08	1.300	0.
39.	$H_2 + M \rightleftharpoons H + H + M^b$	2.23E+12	0.500	92600.
40.	$O_2 + M \rightleftharpoons O + O + M$	1.85E+11	0.500	95560.
41.	$H + OH + M \rightleftharpoons H_2O + M^c$	7.50E+23	-2.600	0.
42.	$H + HO_2 \rightleftharpoons H_2 + O_2$	2.50E+13	0.000	700.

^a Third body efficiencies: $k_{32}(H_2O) = 21k_{32}(Ar)$, $k_{32}(H_2) = 3.3k_{32}(Ar)$,
 $k_{32}(N_2) = k_{32}(O_2) = 0$.

^b Third body efficiencies: $k_{39}(H_2O) = 6k_{39}(Ar)$, $k_{39}(H) = 2k_{39}(Ar)$, $k_{39}(H_2) = 3k_{39}(Ar)$.

^c Third body efficiency: $k_{41}(H_2O) = 20k_{41}(Ar)$.

TABLE 2

0.0000E+00	0.1242E-02	0.1788E-03	1
0.4721E-05	0.1240E-02	0.1790E-03	2
0.2993E-04	0.1231E-02	0.1799E-03	3
0.5602E-04	0.1222E-02	0.1809E-03	4
0.1143E-03	0.1201E-02	0.1831E-03	5
0.2398E-03	0.1162E-02	0.1875E-03	6
0.4946E-03	0.1092E-02	0.1959E-03	7
0.9725E-03	0.9865E-03	0.2103E-03	8
0.1784E-02	0.8524E-03	0.2327E-03	9
0.3027E-02	0.7106E-03	0.2632E-03	10
0.4765E-02	0.5817E-03	0.3007E-03	11
0.7030E-02	0.4754E-03	0.3432E-03	12
0.8389E-02	0.4311E-03	0.3656E-03	13
0.9899E-02	0.3923E-03	0.3885E-03	14
0.1156E-01	0.3586E-03	0.4114E-03	15
0.1337E-01	0.3295E-03	0.4341E-03	16
0.1742E-01	0.2832E-03	0.4776E-03	17
0.1968E-01	0.2650E-03	0.4977E-03	18
0.2208E-01	0.2495E-03	0.5167E-03	19
0.2464E-01	0.2361E-03	0.5345E-03	20
0.2735E-01	0.2246E-03	0.5510E-03	21
0.3022E-01	0.2147E-03	0.5662E-03	22
0.3323E-01	0.2061E-03	0.5802E-03	23
0.3640E-01	0.1986E-03	0.5931E-03	24
0.3970E-01	0.1919E-03	0.6048E-03	25
0.4314E-01	0.1861E-03	0.6156E-03	26
0.4670E-01	0.1808E-03	0.6254E-03	27
0.5036E-01	0.1761E-03	0.6344E-03	28
0.5410E-01	0.1717E-03	0.6427E-03	29
0.5866E-01	0.1672E-03	0.6514E-03	30
0.6099E-01	0.1653E-03	0.6546E-03	31
0.6337E-01	0.1639E-03	0.6566E-03	32
0.6666E-01	0.1628E-03	0.6572E-03	33
0.7014E-01	0.1625E-03	0.6555E-03	34
0.7773E-01	0.1635E-03	0.6475E-03	35
0.8615E-01	0.1654E-03	0.6371E-03	36
0.9539E-01	0.1678E-03	0.6252E-03	37
0.1055E+00	0.1704E-03	0.6124E-03	38
0.1167E+00	0.1734E-03	0.5987E-03	39
0.1320E+00	0.1775E-03	0.5805E-03	40
0.1492E+00	0.1821E-03	0.5611E-03	41
0.1684E+00	0.1872E-03	0.5406E-03	42
0.1898E+00	0.1929E-03	0.5190E-03	43
0.2137E+00	0.1993E-03	0.4964E-03	44
0.2403E+00	0.2063E-03	0.4730E-03	45
0.2699E+00	0.2142E-03	0.4487E-03	46
0.3028E+00	0.2230E-03	0.4238E-03	47
0.3393E+00	0.2329E-03	0.3984E-03	48
0.3795E+00	0.2439E-03	0.3727E-03	49
0.4236E+00	0.2563E-03	0.3470E-03	50
0.4718E+00	0.2703E-03	0.3214E-03	51
0.5237E+00	0.2862E-03	0.2962E-03	52
0.5787E+00	0.3041E-03	0.2718E-03	53
0.6359E+00	0.3246E-03	0.2485E-03	54
0.6939E+00	0.3480E-03	0.2265E-03	55
0.7507E+00	0.3746E-03	0.2062E-03	56
0.8043E+00	0.4045E-03	0.1877E-03	57
0.8524E+00	0.4375E-03	0.1715E-03	58
0.8933E+00	0.4724E-03	0.1575E-03	59
0.9262E+00	0.5073E-03	0.1460E-03	60
0.9511E+00	0.5400E-03	0.1369E-03	61
0.9689E+00	0.5683E-03	0.1301E-03	62
0.9755E+00	0.5803E-03	0.1275E-03	63
0.1000E+01	0.5886E-03	0.1246E-03	64
-1.0	0.	0.	
F	DENSITY	VISCOSITY	

 (end of input)

This file contains the state functions of density and viscosity to be read by program BETPDF. These data are from the Tsuji counterflow quoted from Keyes & Smooke, J. Comp. Phys., v.73, pp.267-288 (1987). The card beginning with "-1.0" is the sentinel required by BETPDF.

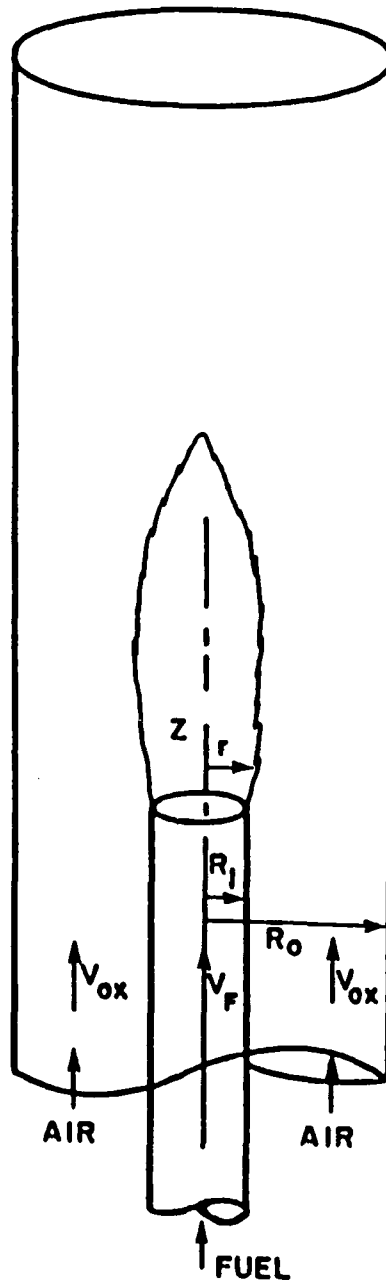


Figure 1: Schematic of a confined axisymmetric laminar diffusion flame.

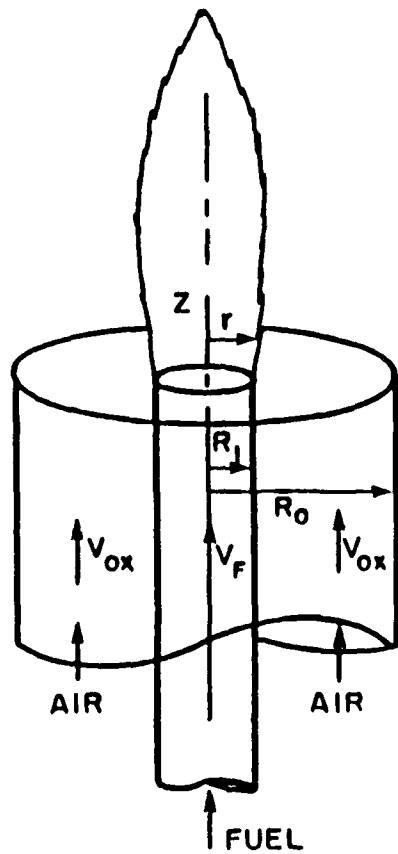


Figure 2: Schematic of an unconfined axisymmetric laminar diffusion flame.

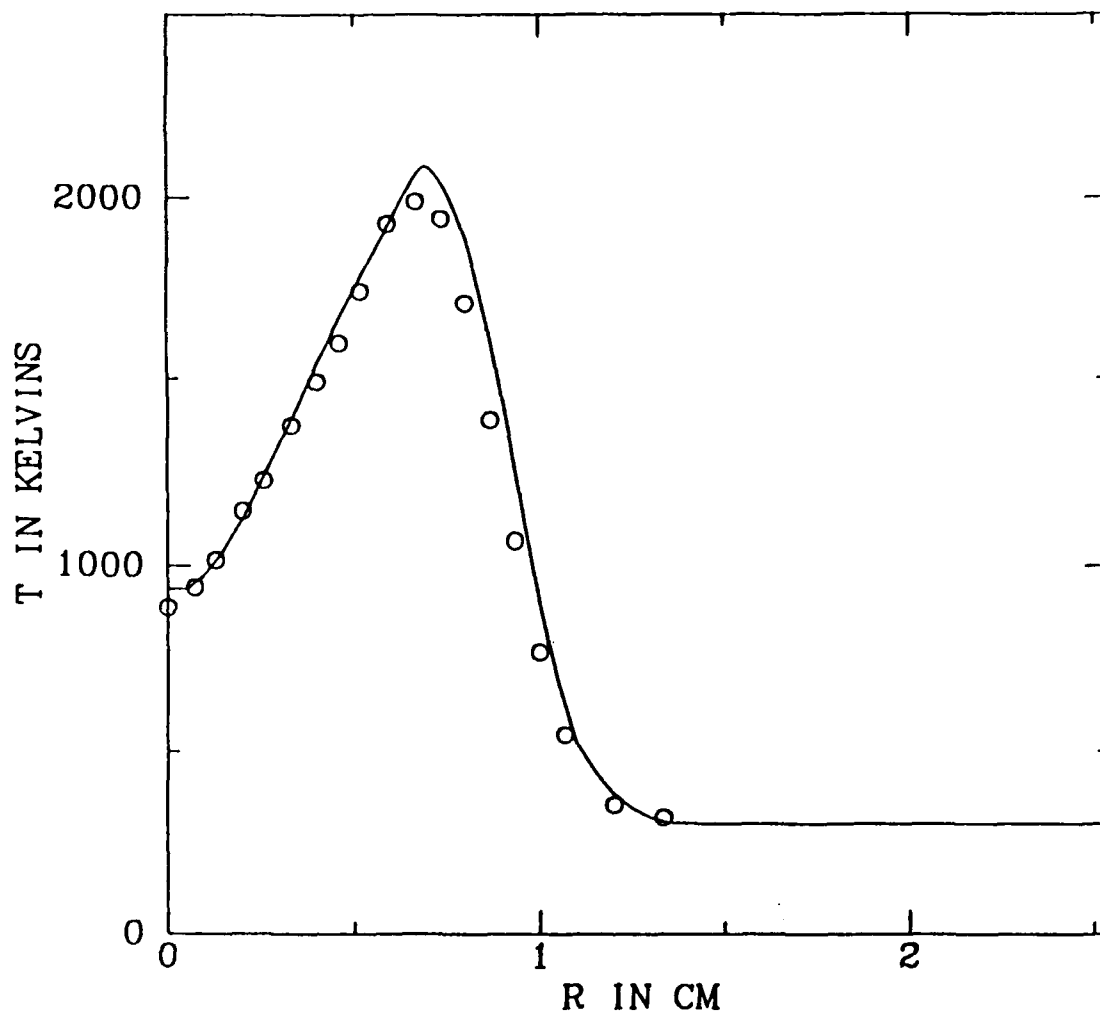


Figure 3: Experimental (o) and computational (solid line) temperature profiles for the confined methane-air laminar diffusion flame at a height of 1.2 cm above the burner inlet.

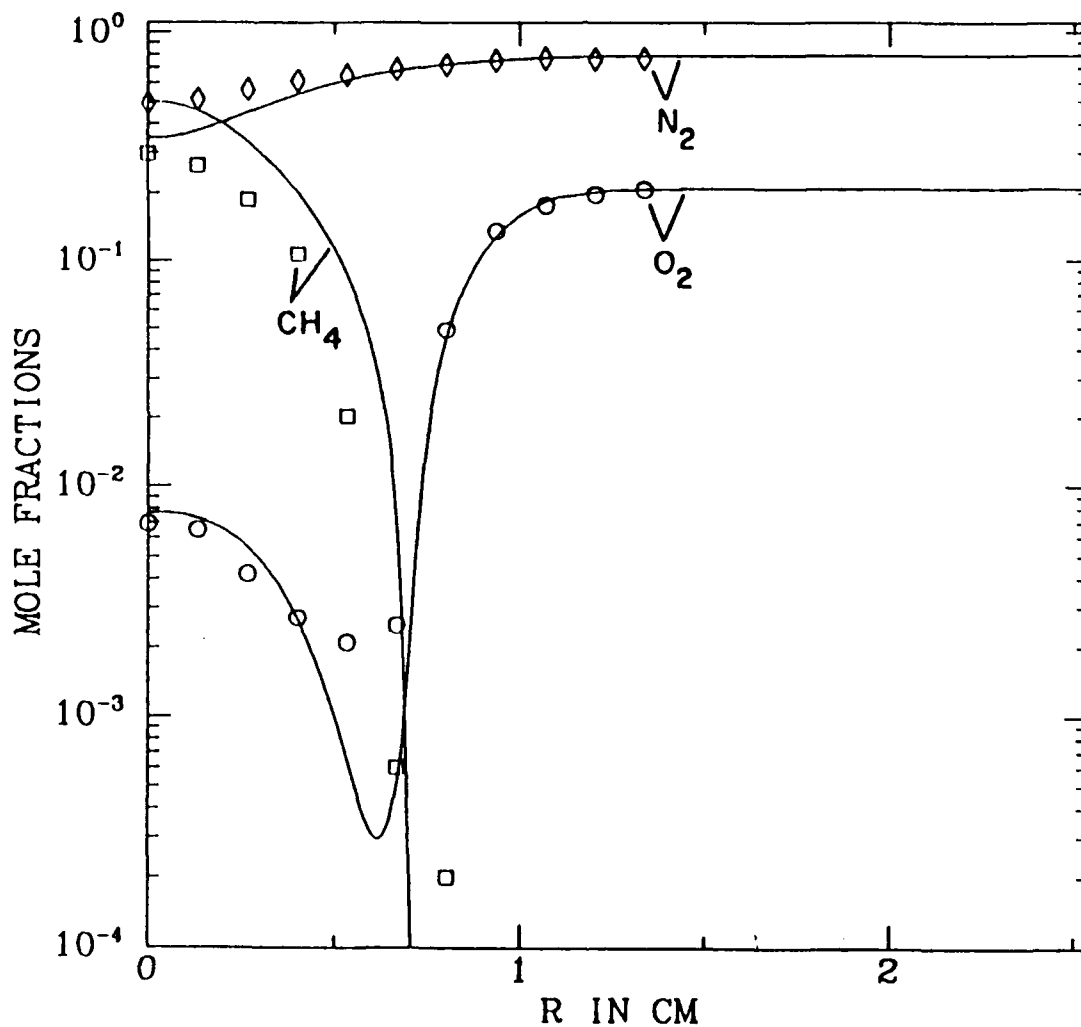


Figure 4: Comparison between measured CH_4 (\square), O_2 , (\circ) and N_2 (\diamond) profiles and corresponding computational values (solid line) at a height of 1.2 cm above the burner inlet.

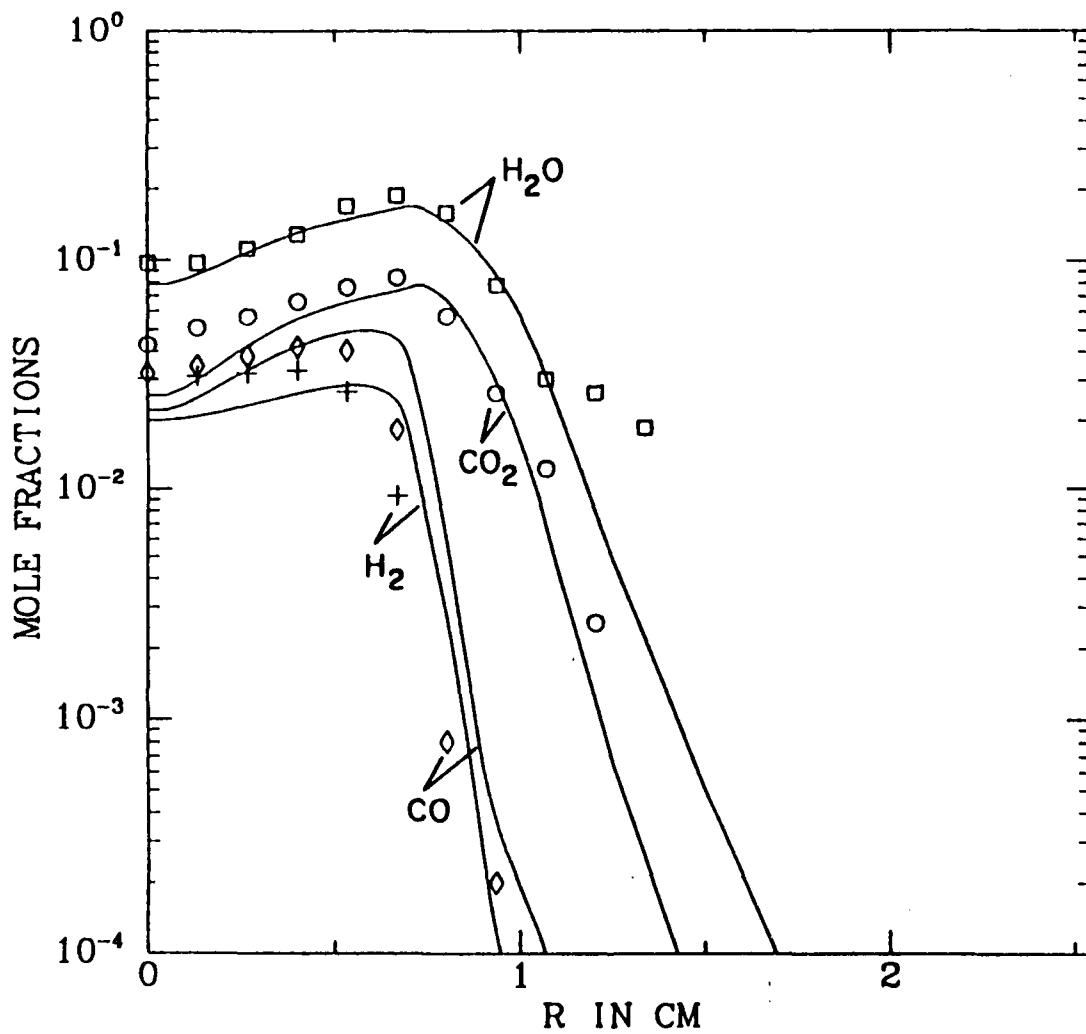


Figure 5: Comparison between measured H_2O (\square), CO_2 (\circ), CO (\diamond) and H_2 ($+$) profiles and corresponding computational values (solid line) at a height of 1.2 cm above the burner inlet.

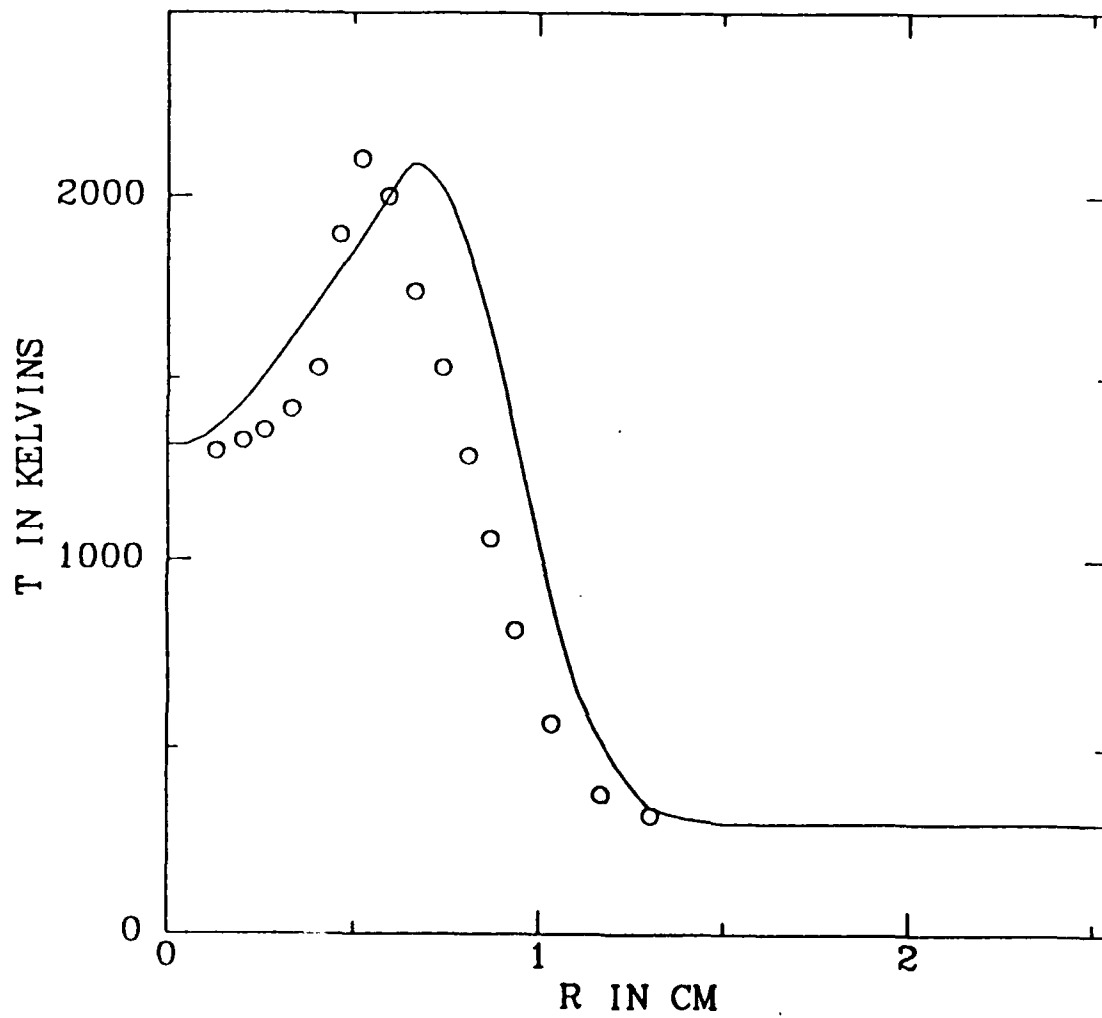


Figure 6: Experimental (o) and computational (solid line) temperature profiles for the confined methane-air laminar diffusion flame at a height of 2.4 cm above the burner inlet.

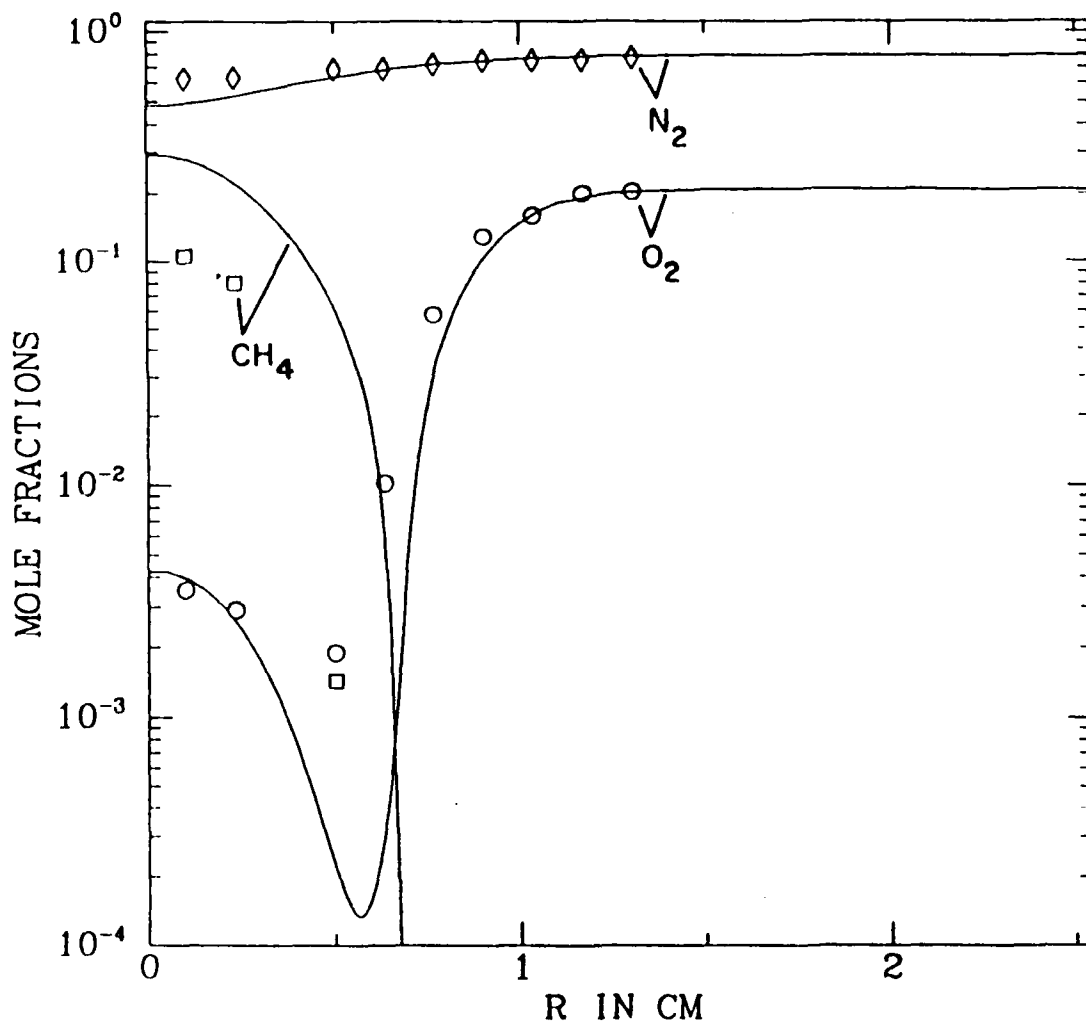


Figure 7: Comparison between measured CH_4 (\square), O_2 , (\circ) and N_2 (\diamond) profiles and corresponding computational values (solid line) at a height of 2.4 cm above the burner inlet.

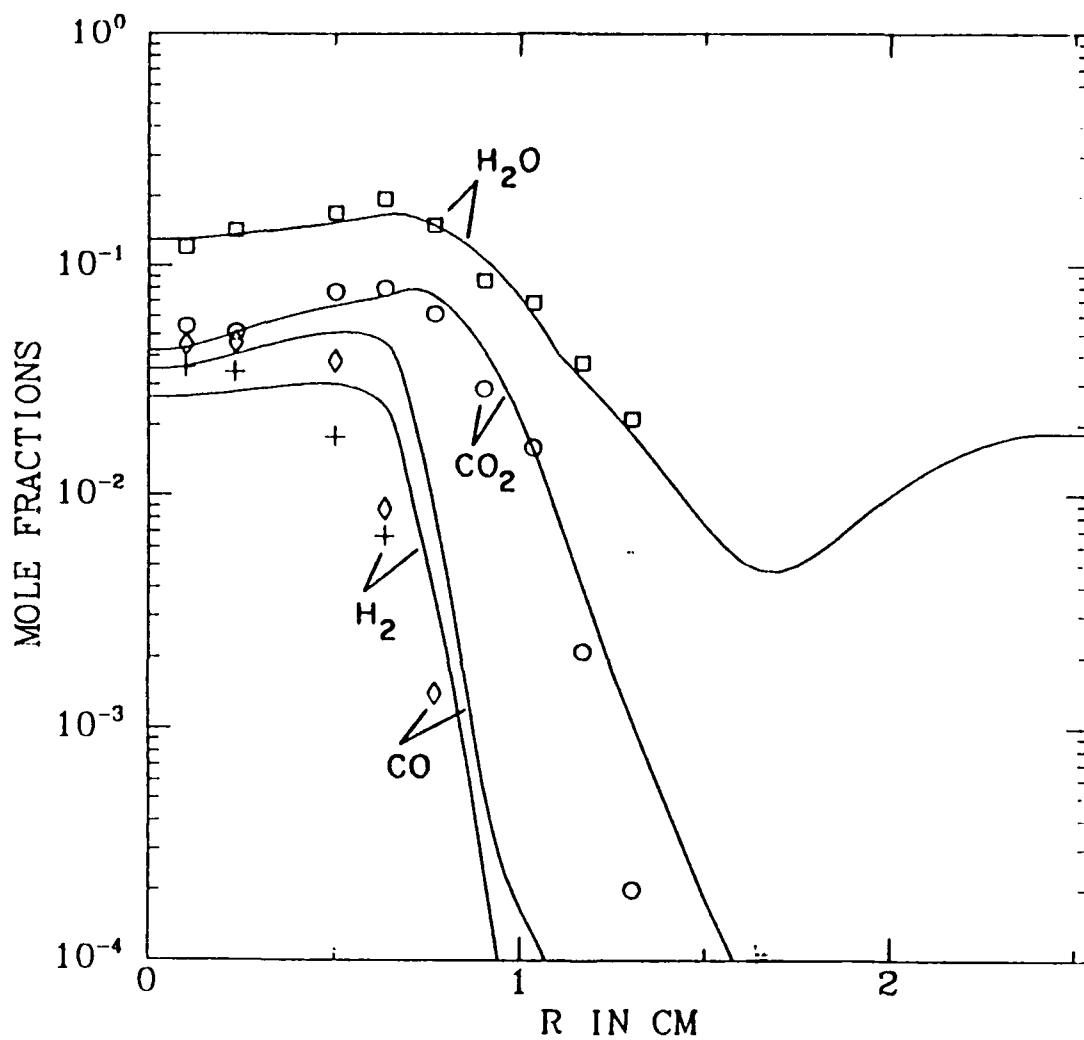


Figure 8: Comparison between measured H_2O (\square), CO_2 (\circ), CO (\diamond) and H_2 ($+$) profiles and corresponding computational values (solid line) at a height of 2.4 cm above the burner inlet.

Temperature

(K)

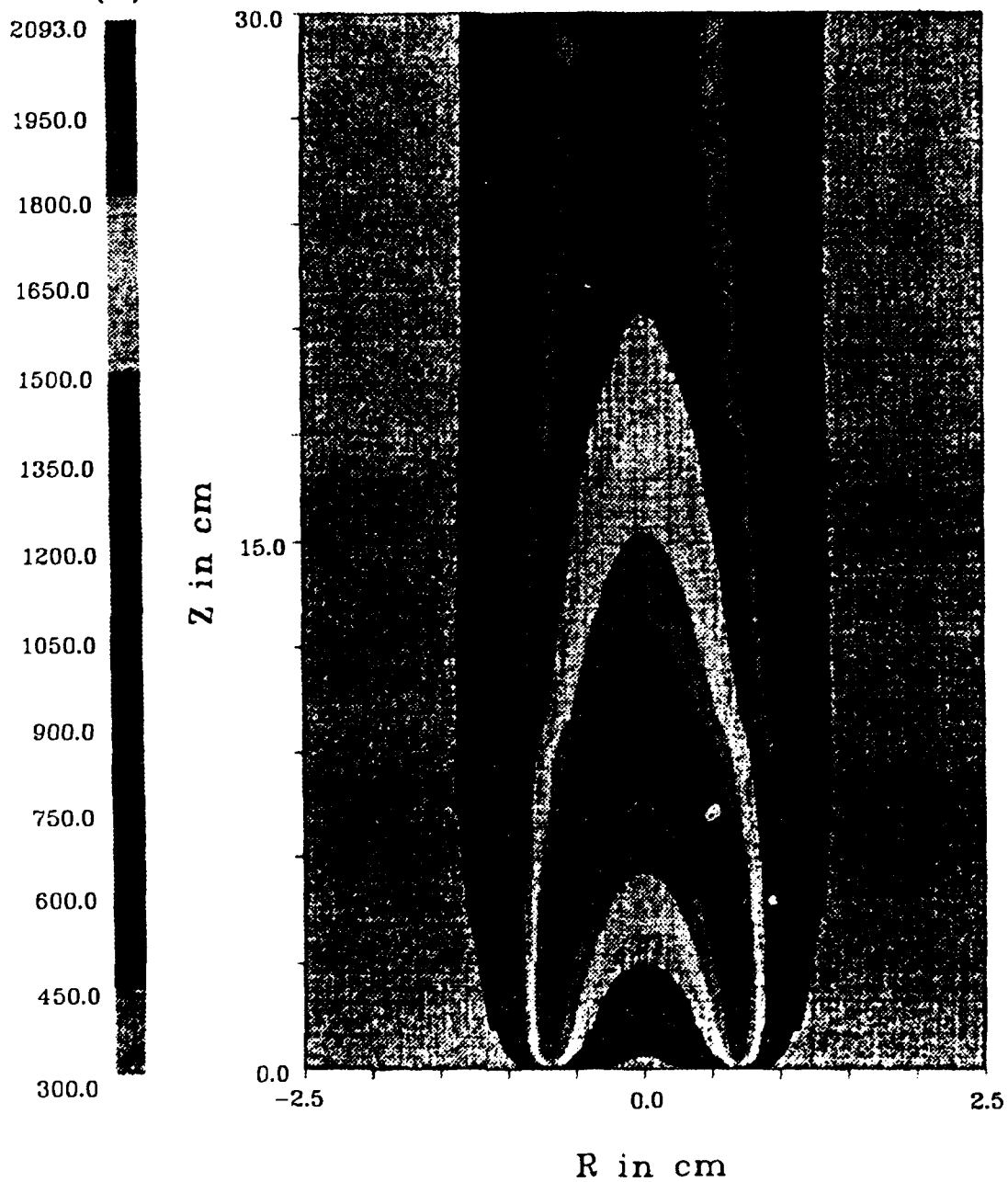


Figure 9: Temperature isotherms for the confined methane-air laminar diffusion flame.

Mass Fraction

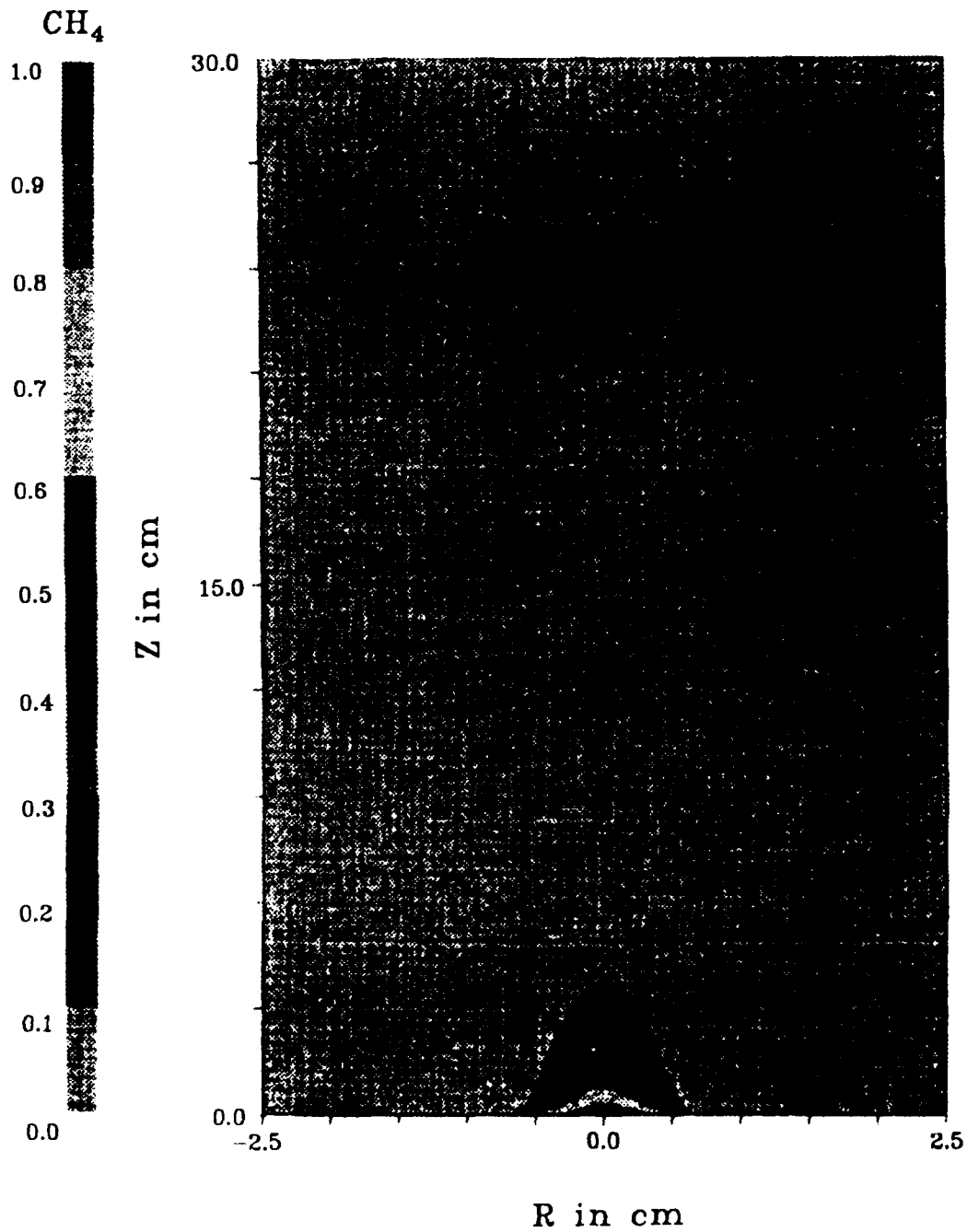


Figure 10: Methane (CH₄) isopleths for the confined methane-air laminar diffusion flame.

Mass Fraction

O_2

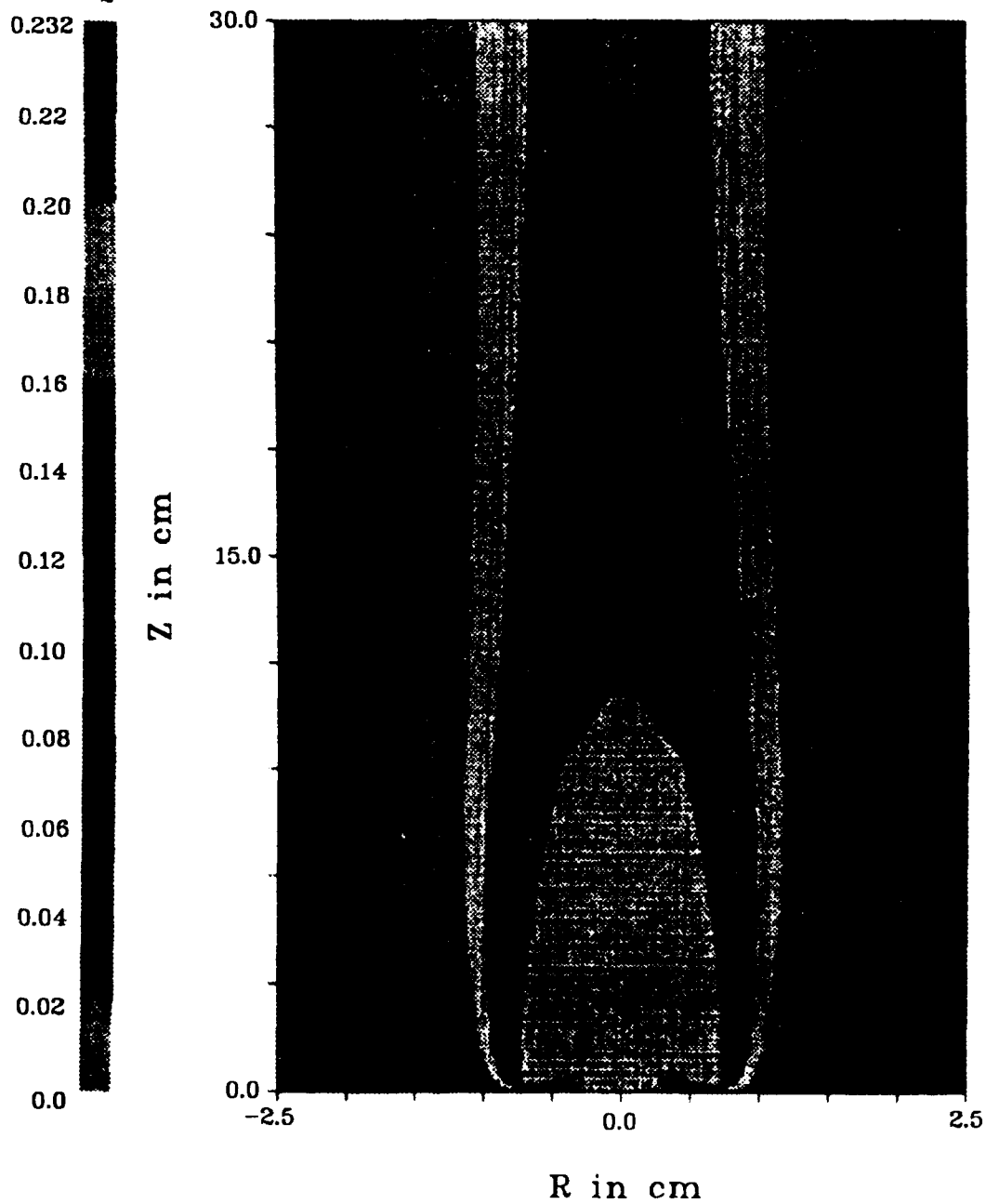


Figure 11: Oxygen (O_2) isopleths for the confined methane-air laminar diffusion flame.

Mass Fraction

H_2O

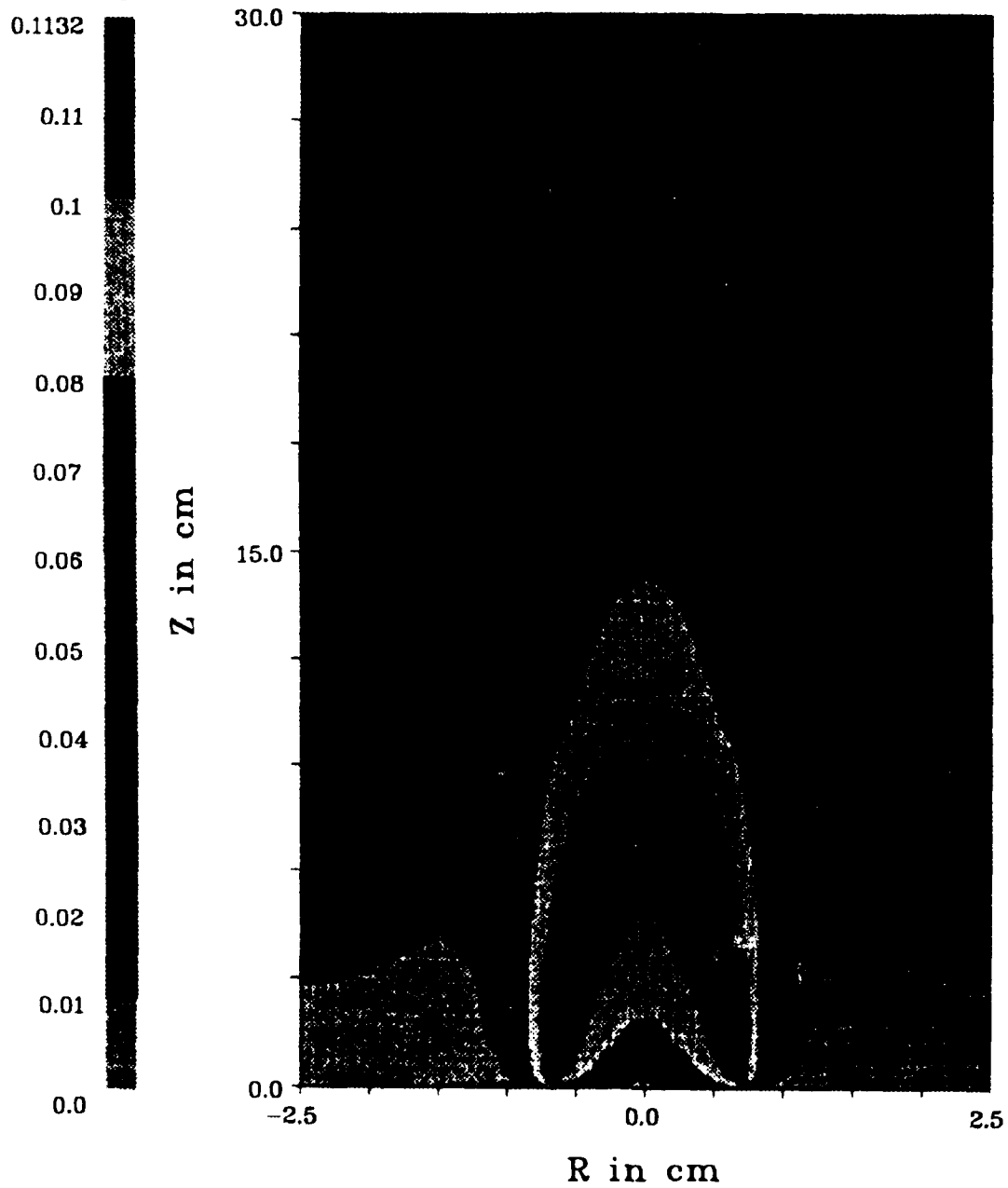


Figure 12: Water (H_2O) isopleths for the confined methane-air laminar diffusion flame.

Mass Fraction

CO

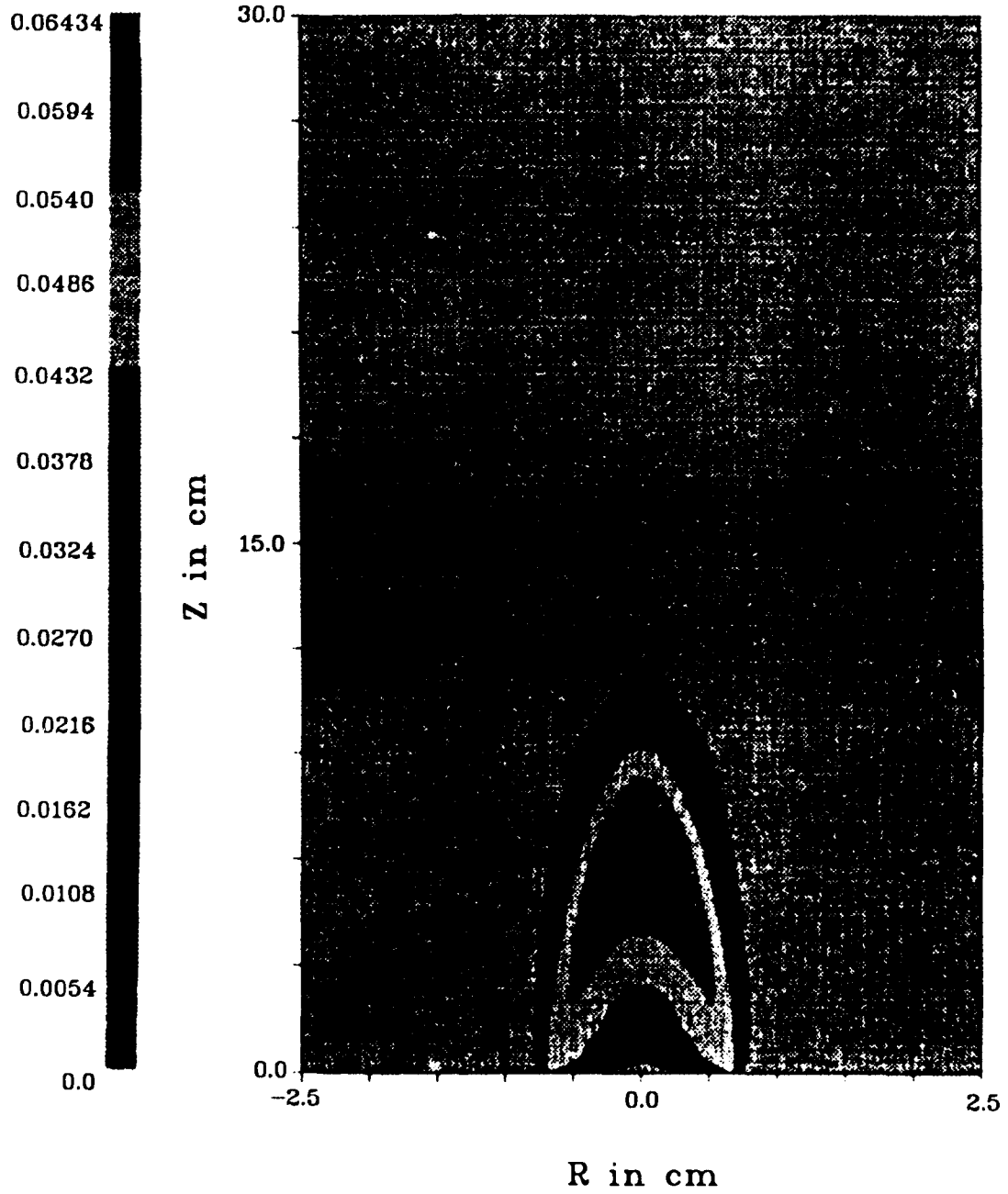


Figure 13: Carbon Monoxide (CO) isopleths for the confined methane-air laminar diffusion flame.

Mass Fraction

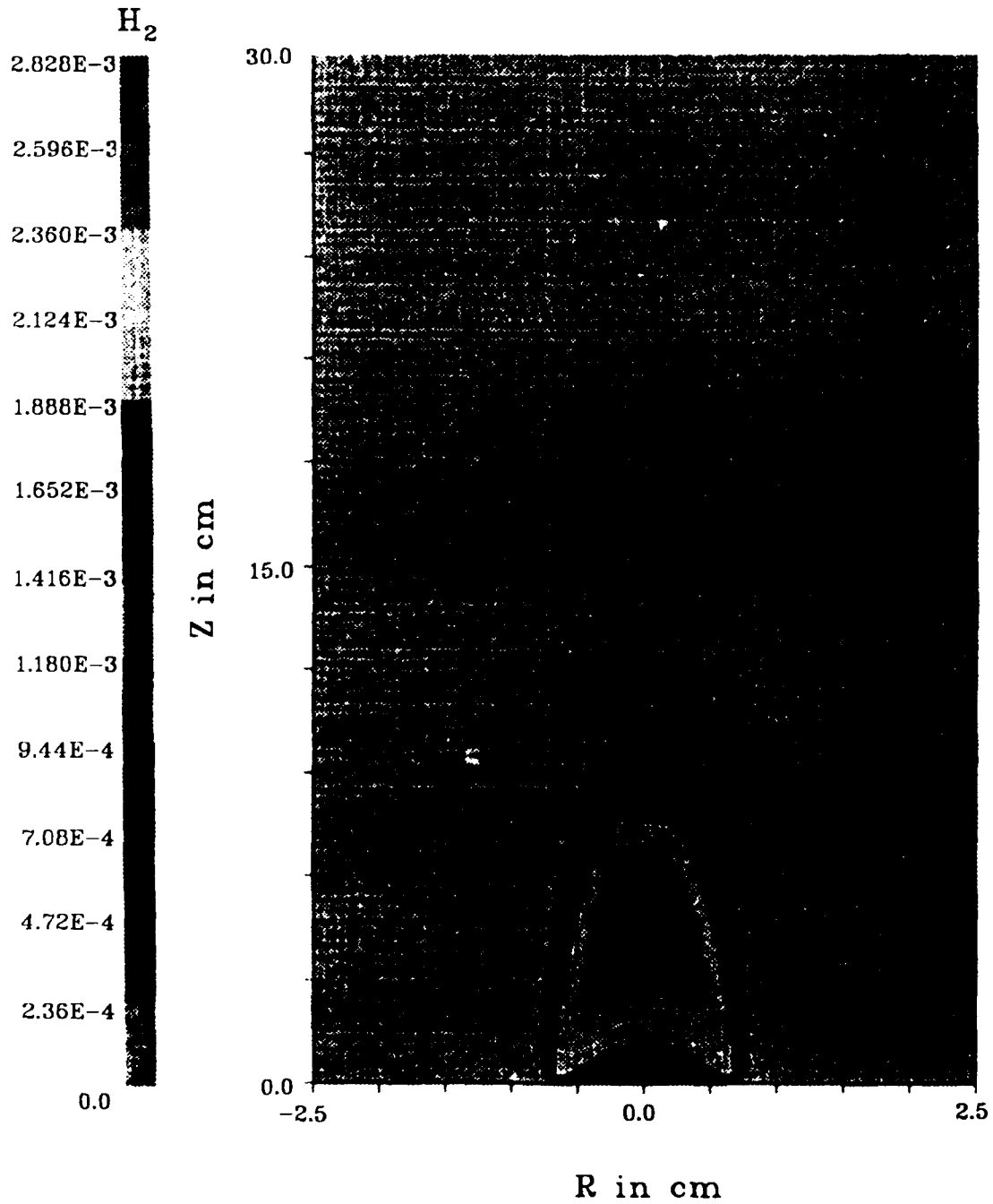


Figure 14: Molecular hydrogen (H_2) isopleths for the confined methane-air laminar diffusion flame.

Mass Fraction

CO₂

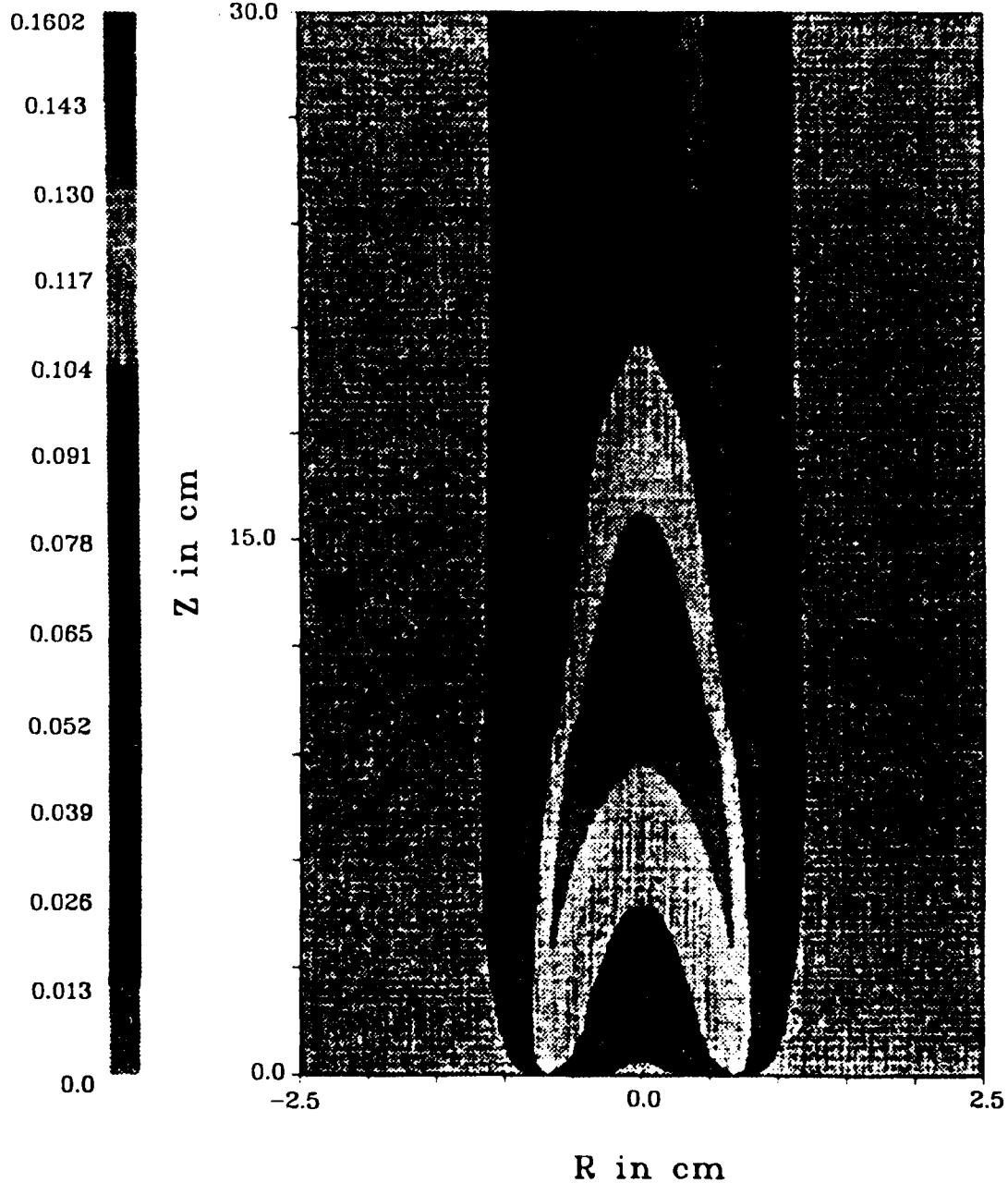


Figure 15: Carbon Dioxide (CO₂) isopleths for the confined methane-air laminar diffusion flame.

Mass Fraction

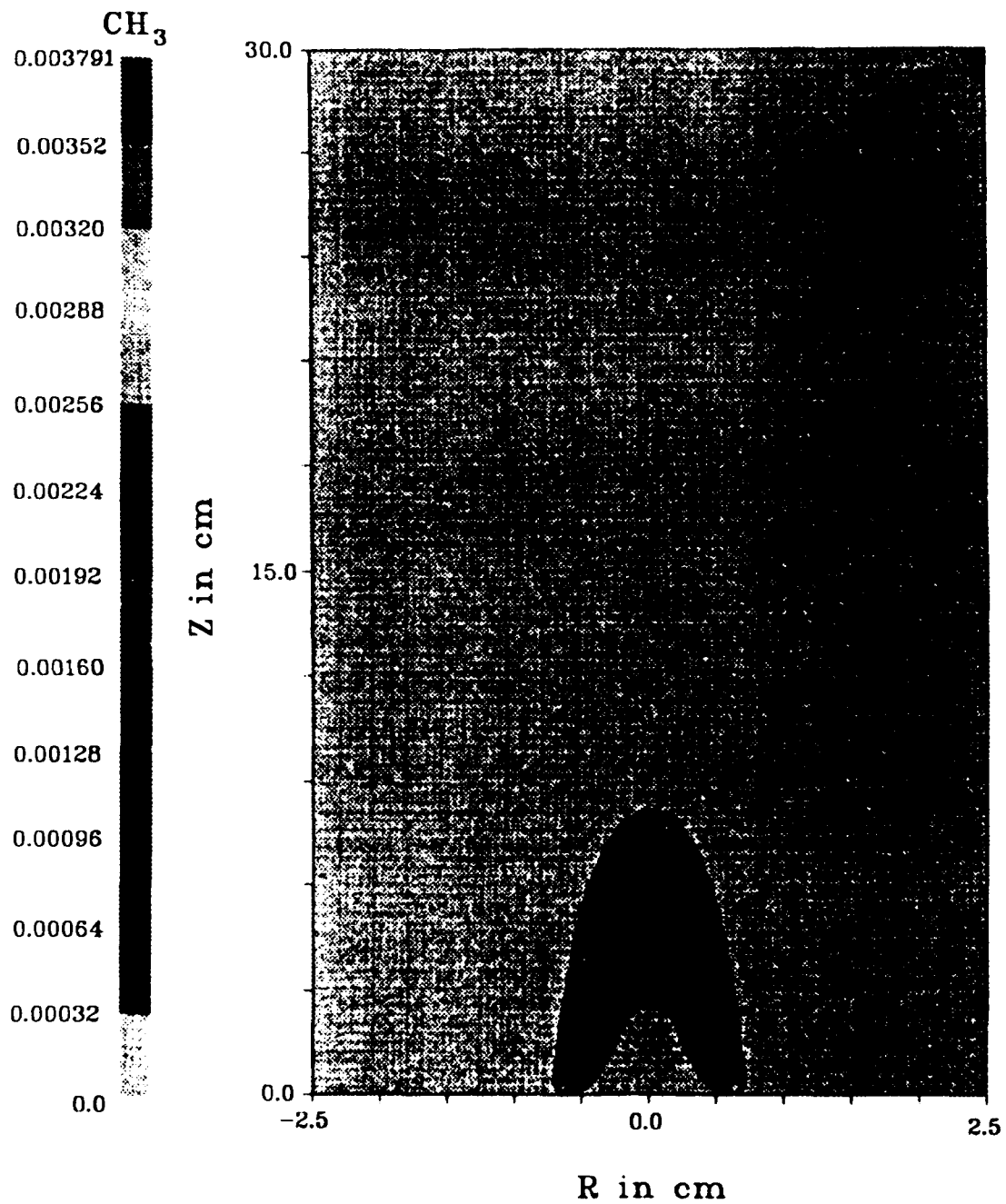


Figure 16: Methyl radical (CH₃) isopleths for the confined methane-air laminar diffusion flame.

Mass Fraction
OH

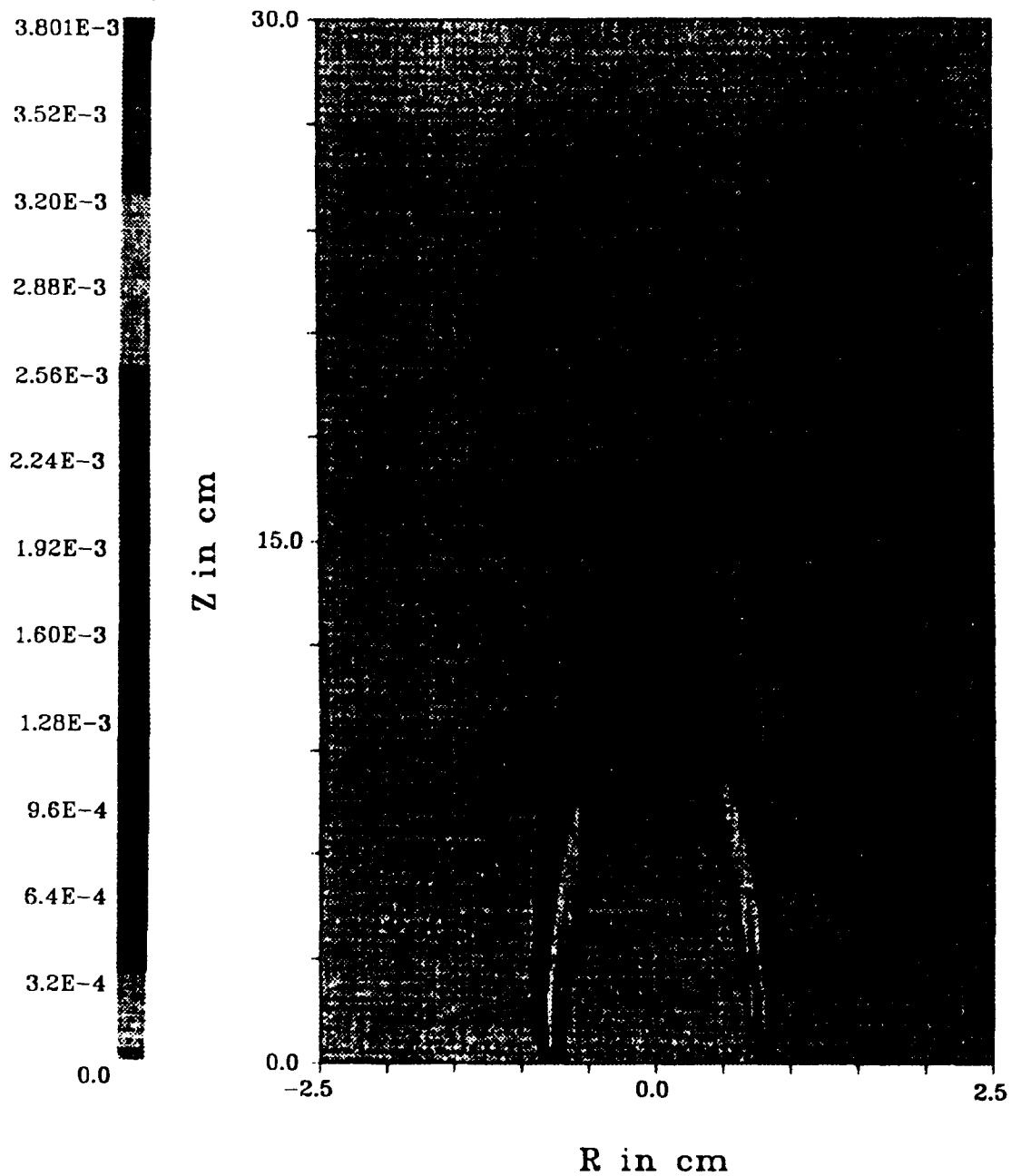


Figure 17: Hydroxyl radical (OH) isopleths for the confined methane-air laminar diffusion flame.

Mass Fraction

CH_2O

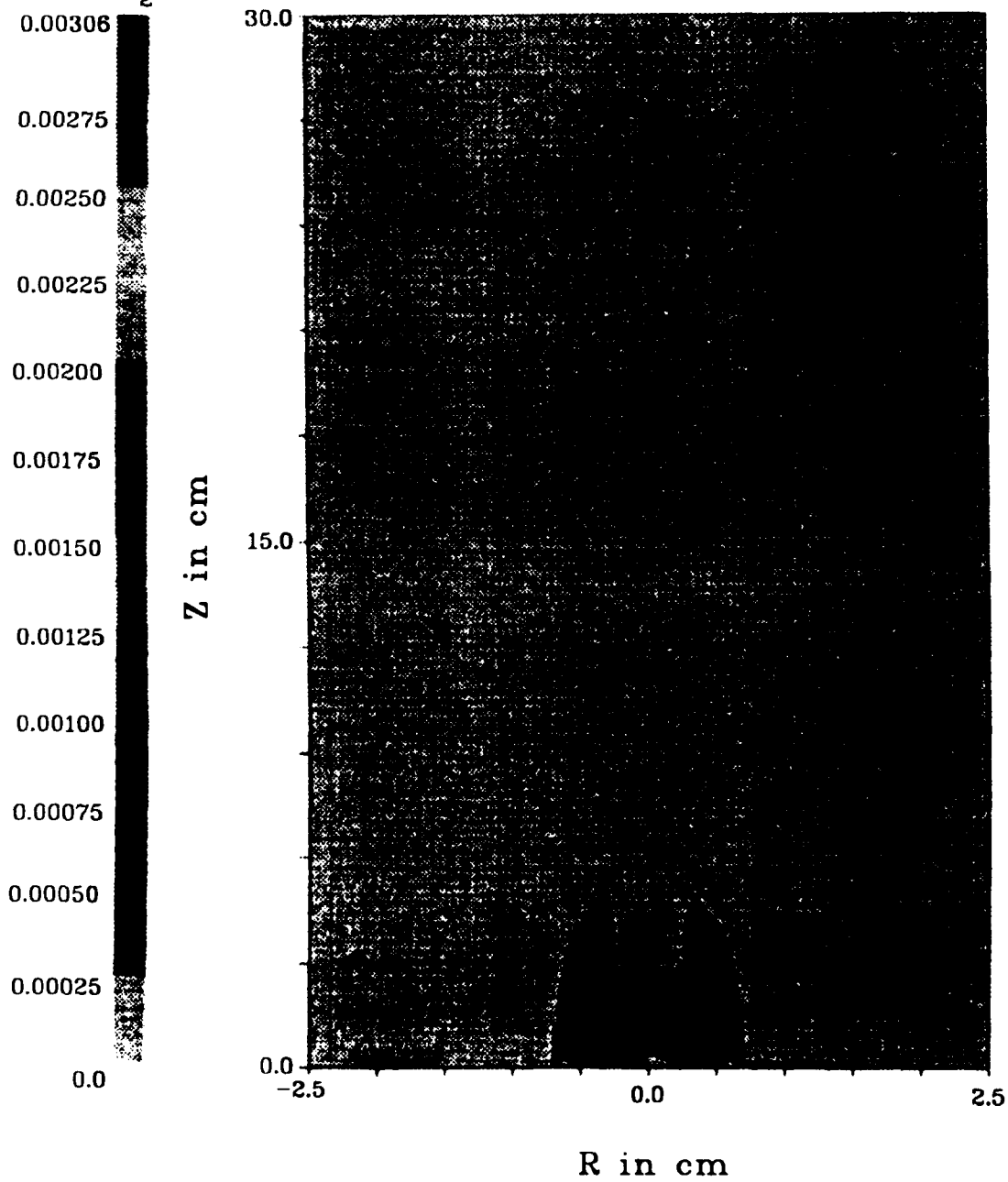


Figure 18: Formaldehyde (CH_2O) isopleths for the confined methane-air laminar diffusion flame.

Streamlines

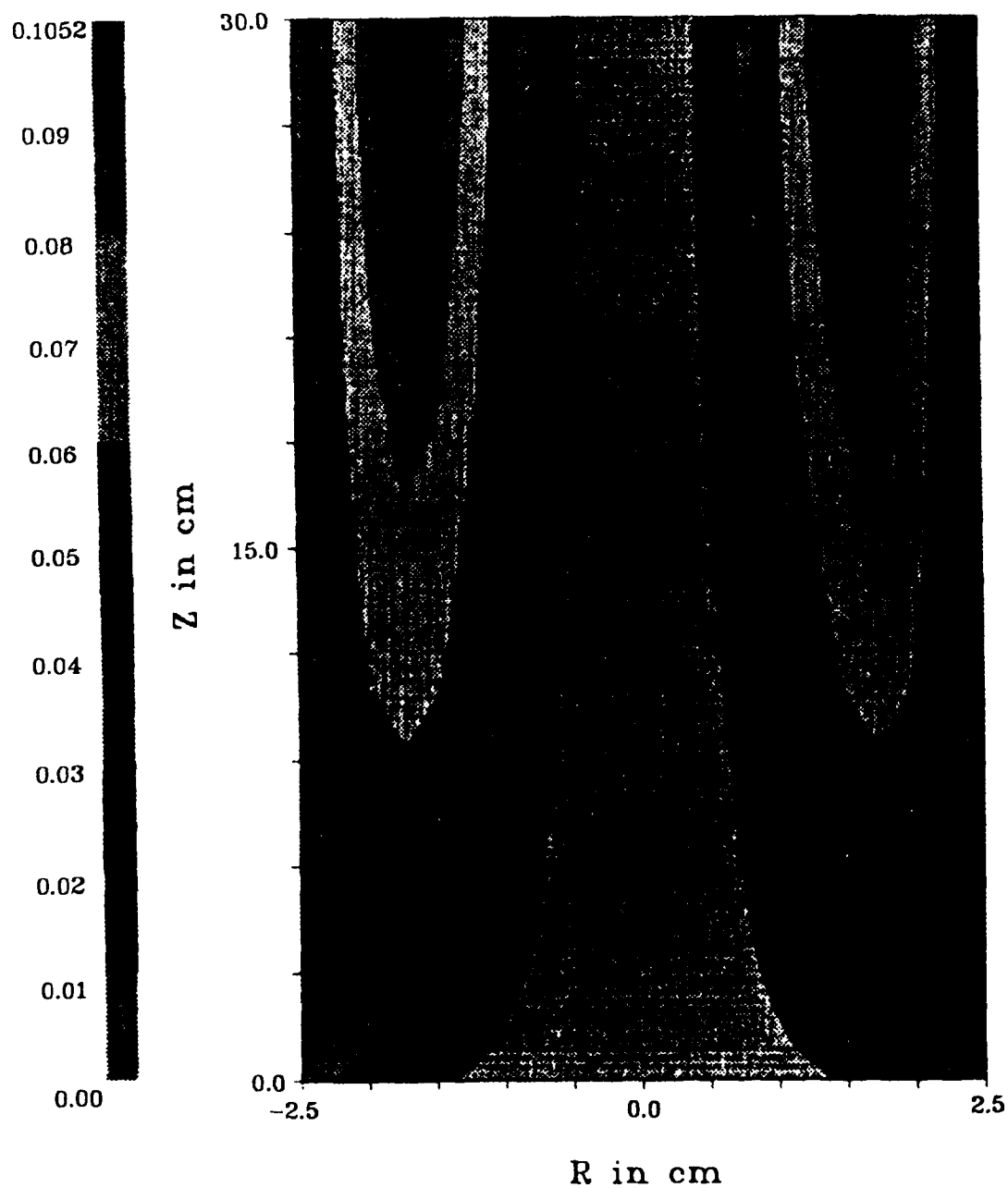


Figure 19: Stream function isopleths for the confined methane-air laminar diffusion flame.

Temperature
(K)

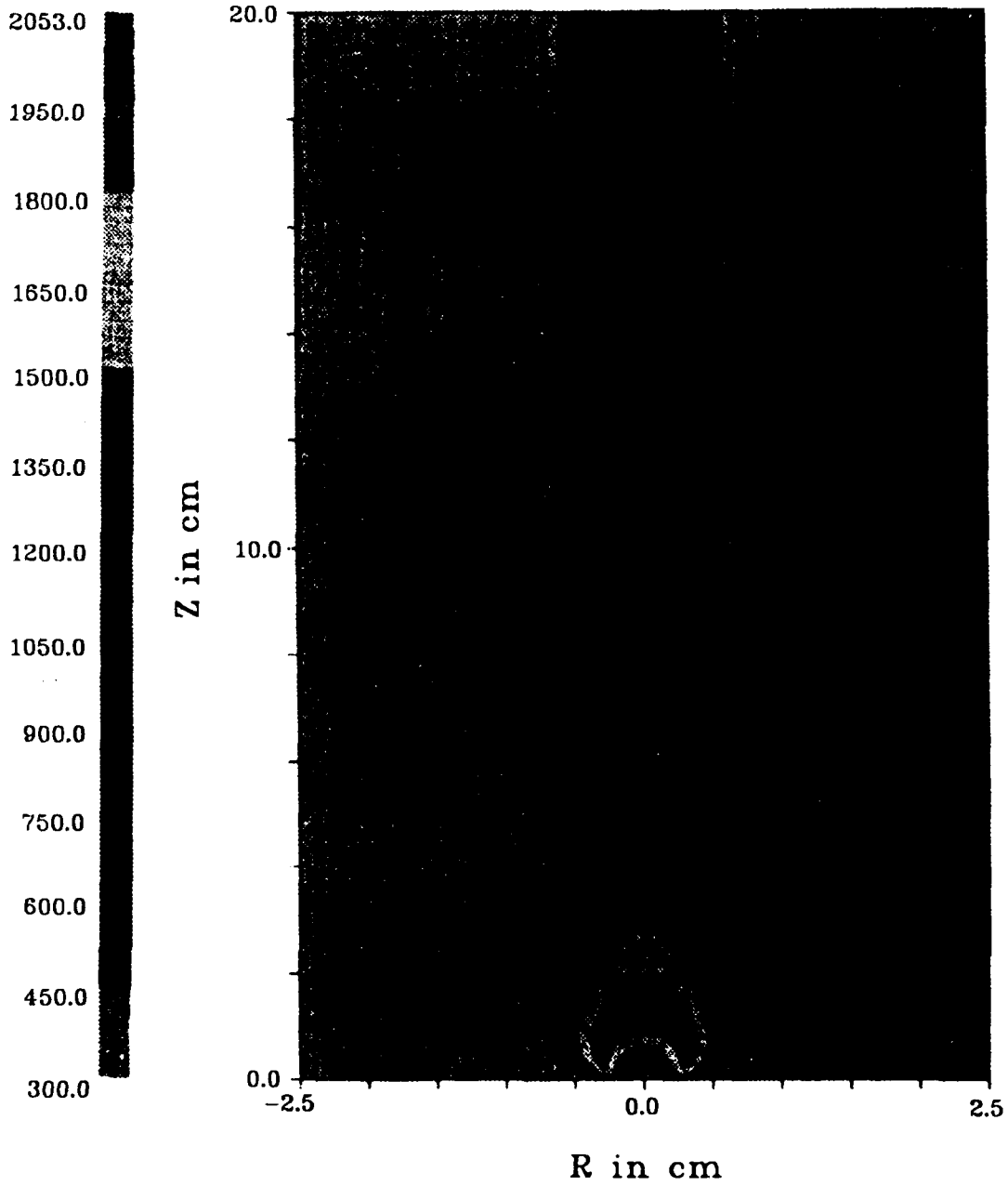


Figure 20: Temperature isotherms for the unconfined methane-air laminar diffusion flame.

Streamlines

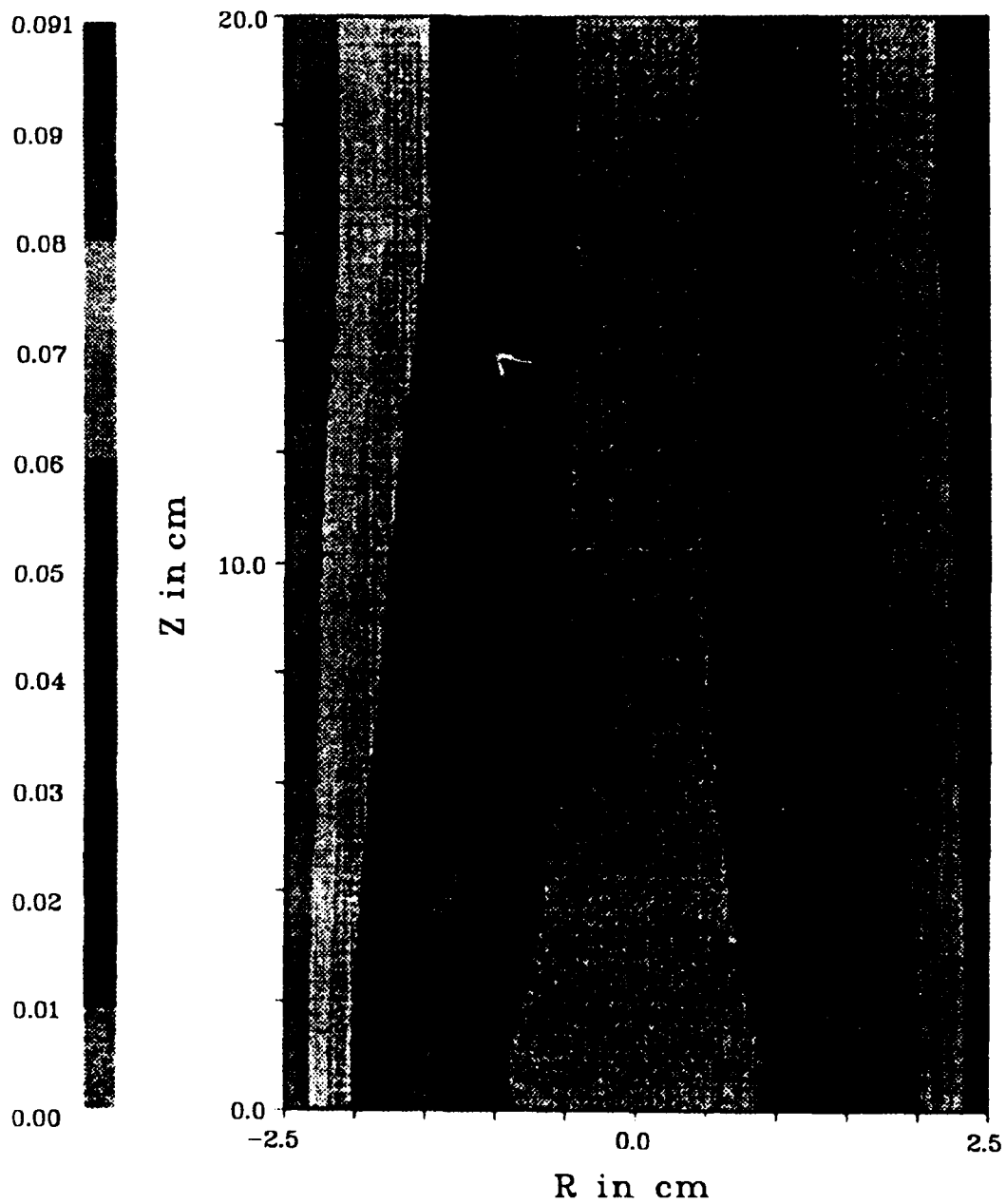


Figure 21: Stream function isopleths for the unconfined methane-air laminar diffusion flame.

Vorticity

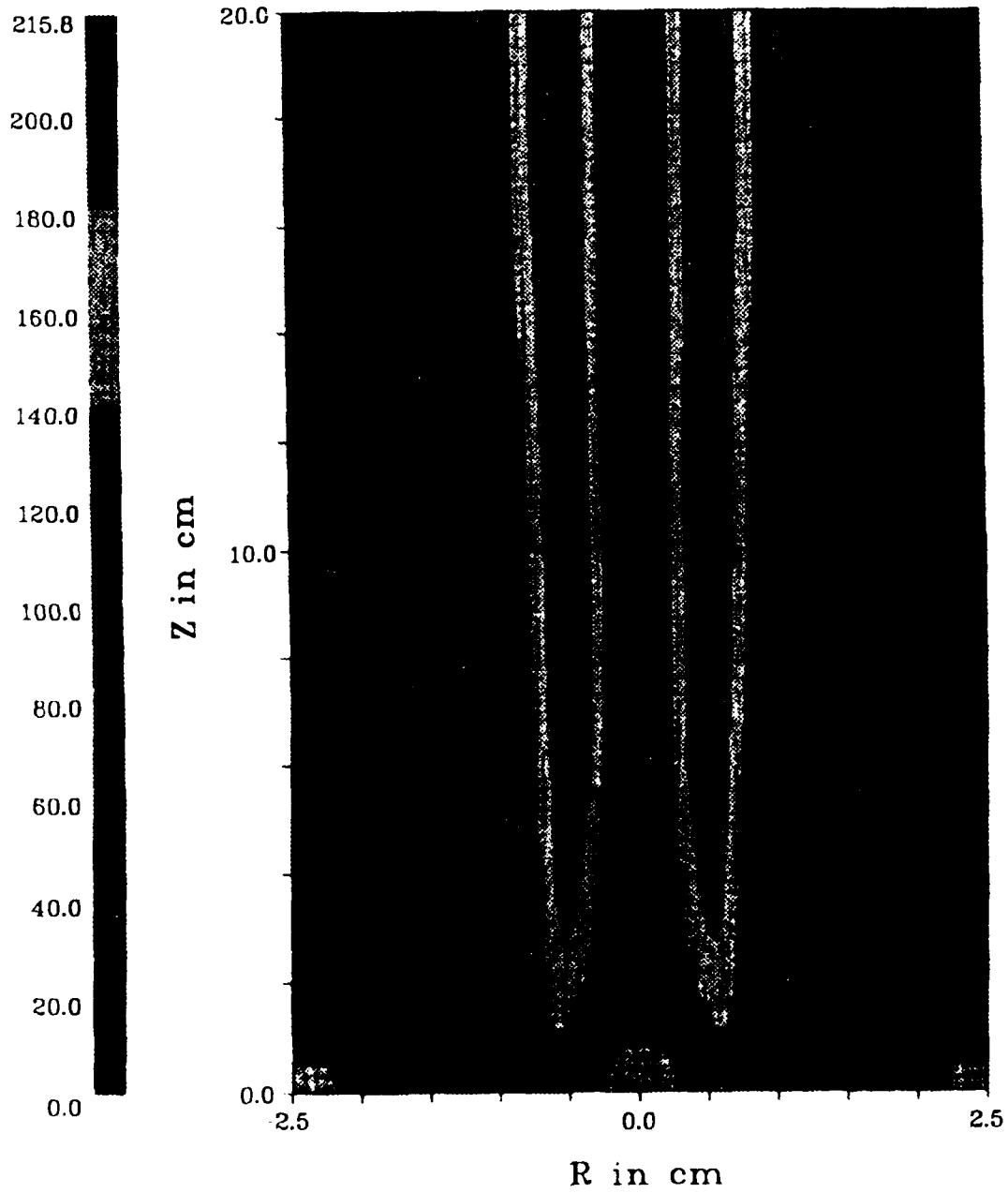


Figure 22: Vorticity isopleths for the unconfined methane-air laminar diffusion flame.

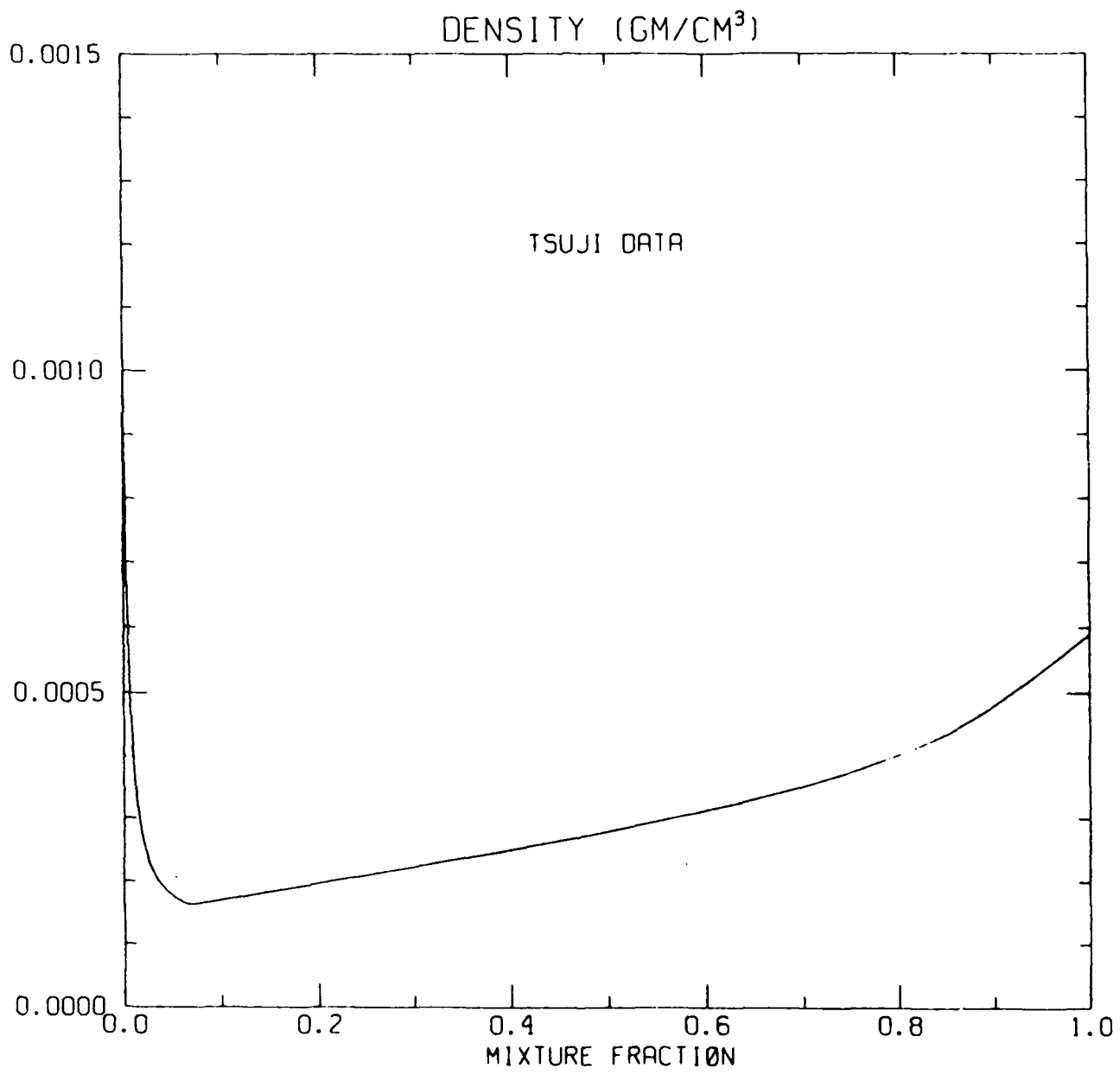


Figure 23: Density versus mixture fraction for the Tsuji counterflow flame.

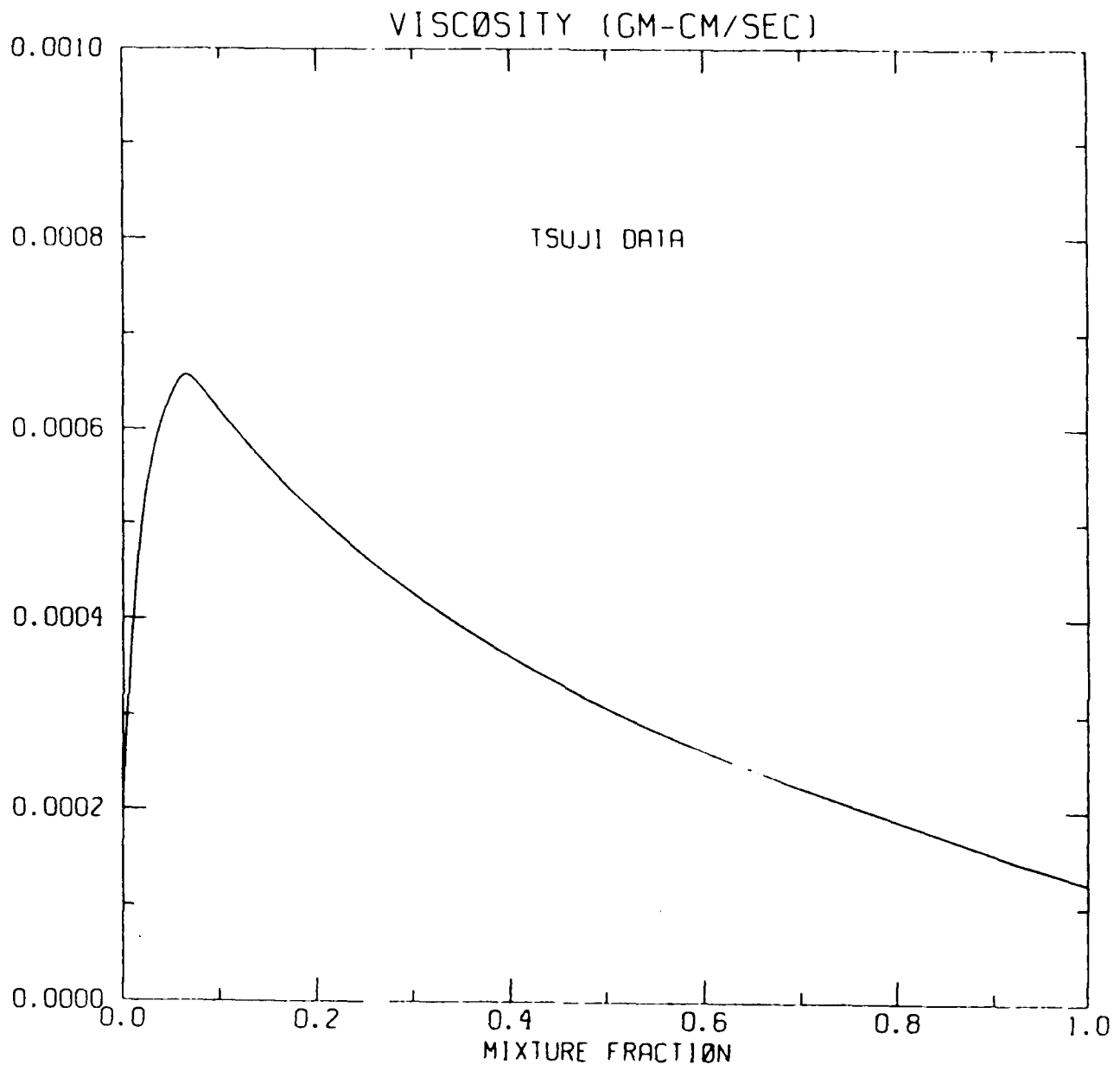


Figure 24: Viscosity versus mixture fraction for the Tsuji counterflow flame.

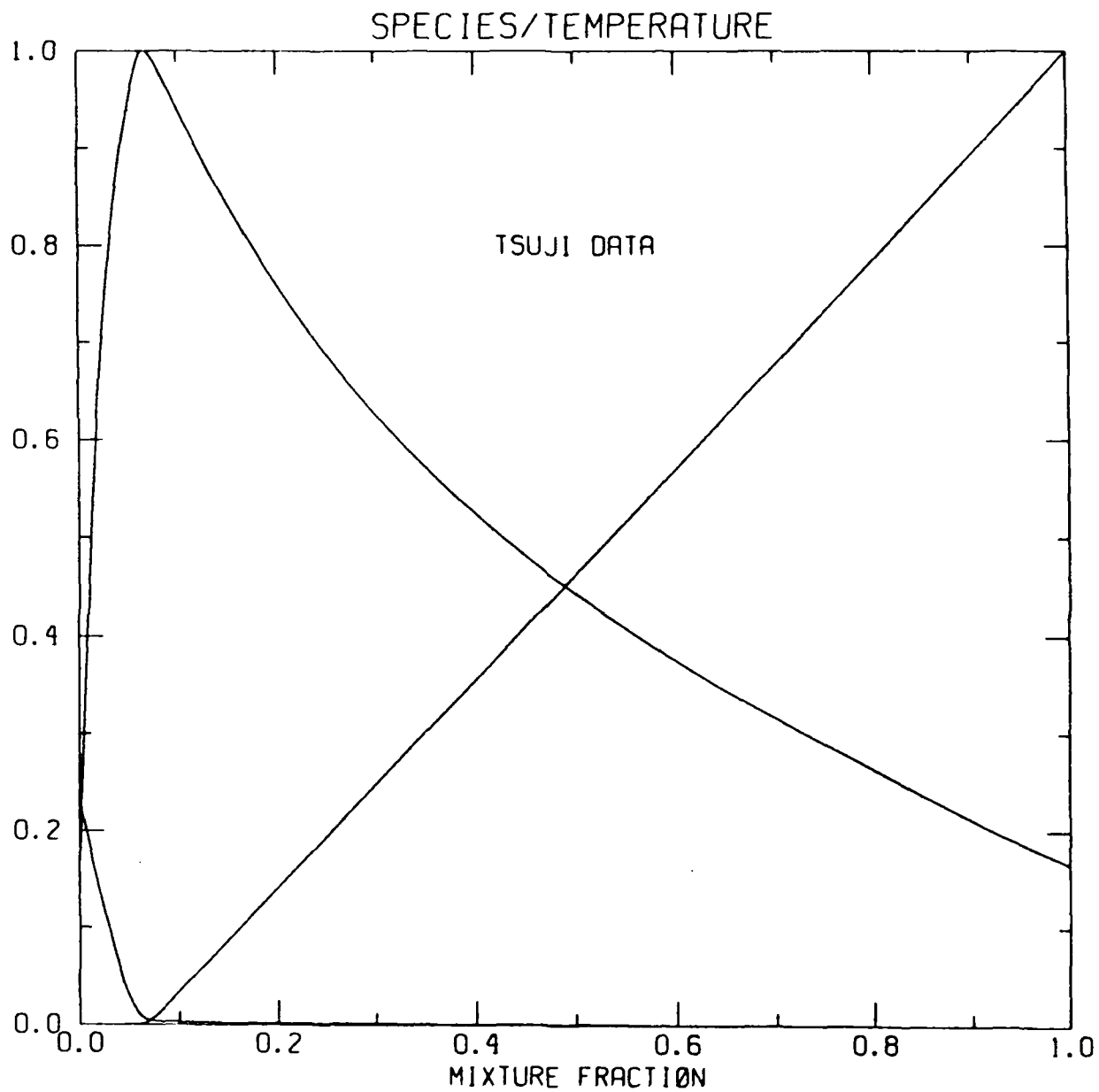


Figure 25: Fuel mass fraction (peaking at $f = 1$), oxygen mass fraction (peaking at $f = 0$), and temperature (peaking near $f = f_{st}$) for the Tsuji counterflow.

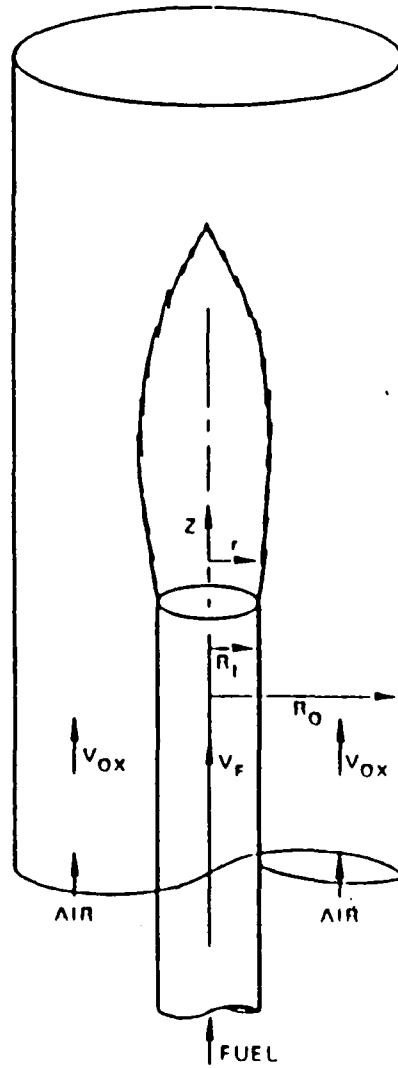


Figure 26: Schematic of confined coaxial configuration solved by AXIJET-T.

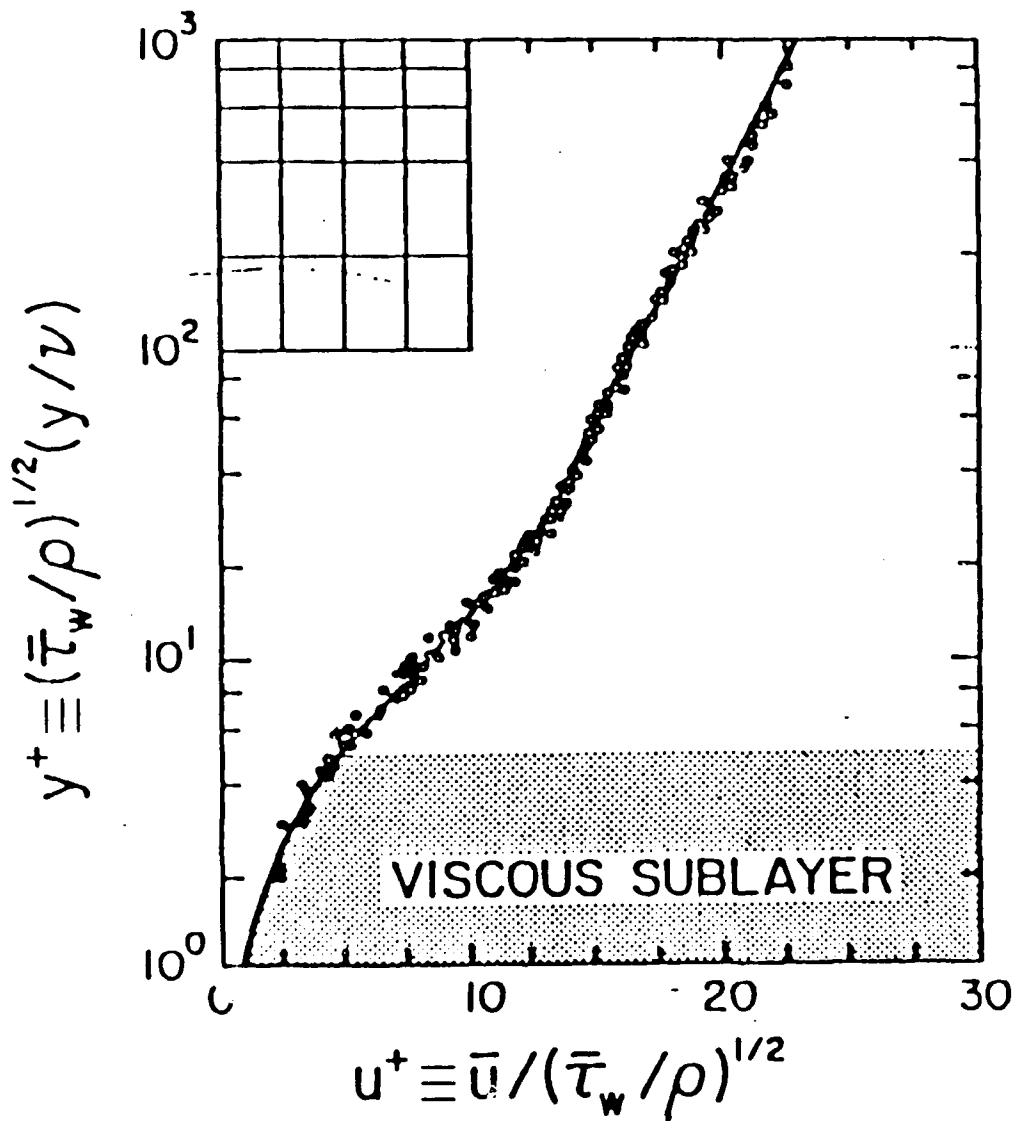


Figure 27: y^+ versus u^+ on a linear-log plot, illustrating the log law.

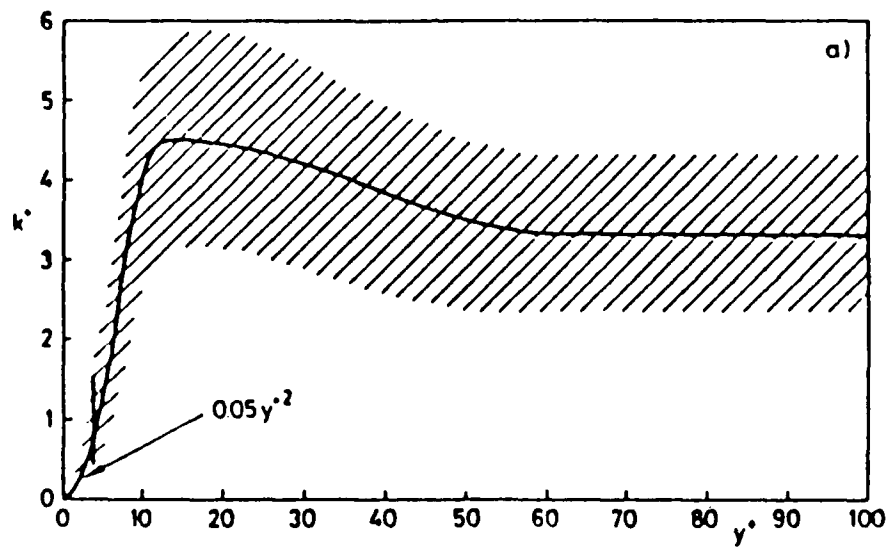


Figure 28: k^+ versus y^+ , illustrating the wall law for k .

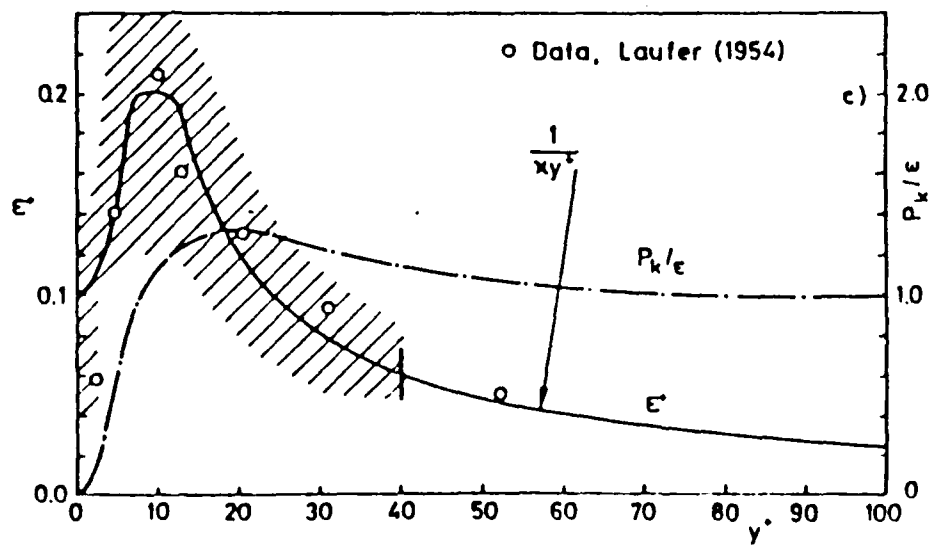


Figure 29: ϵ^+ versus y^+ , illustrating the wall law for ϵ .

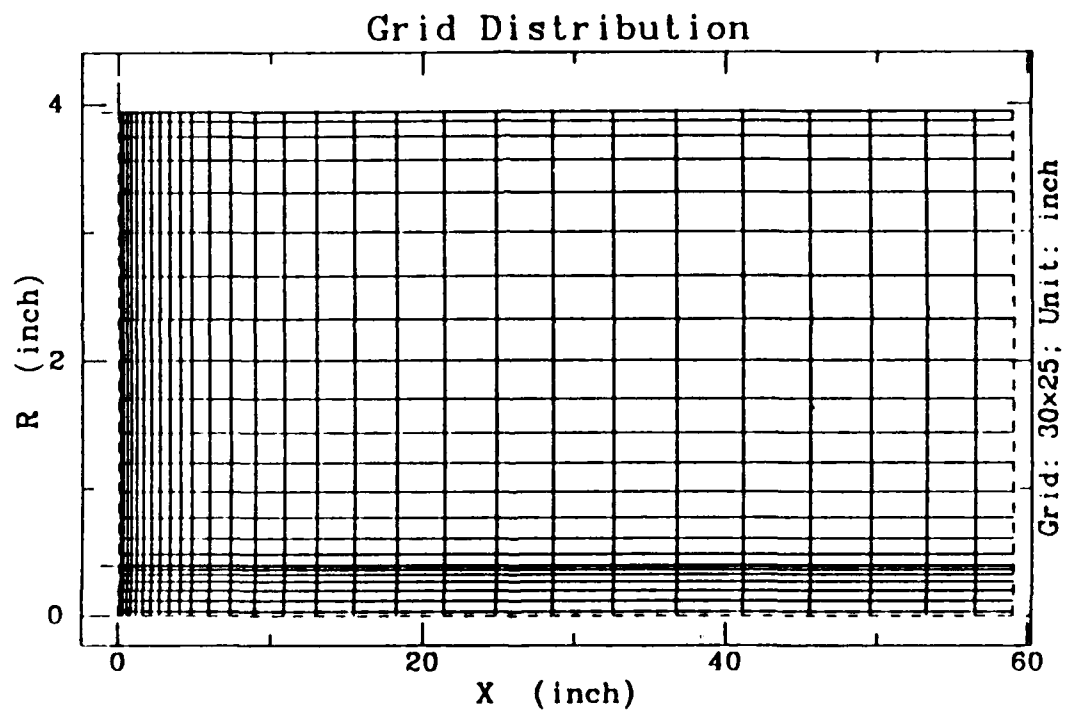
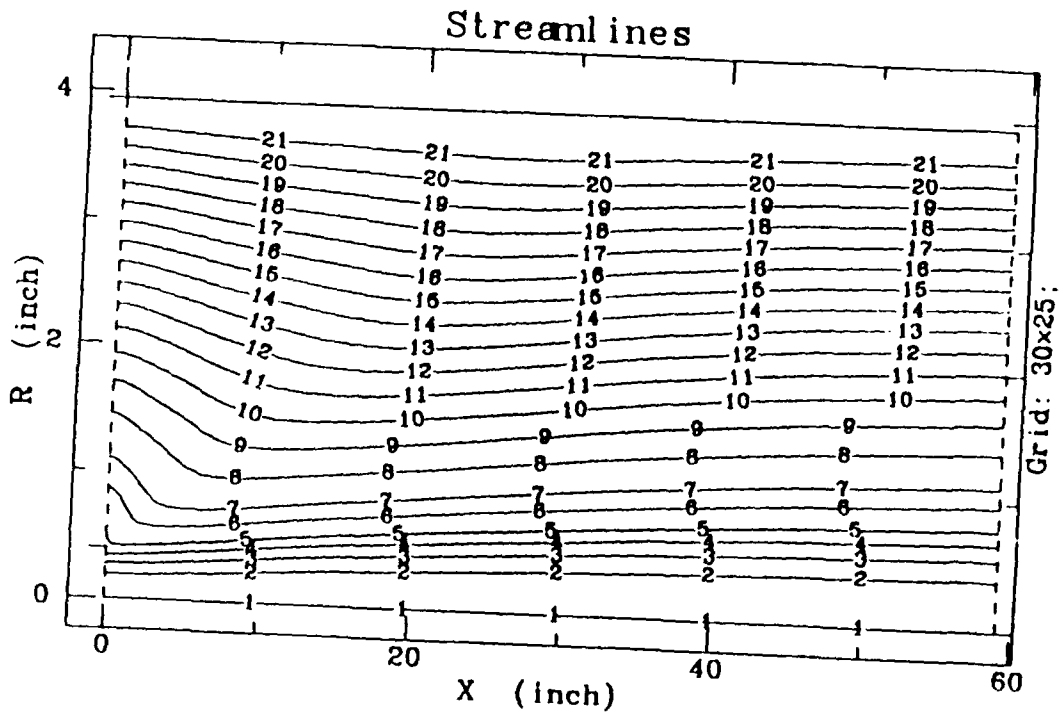


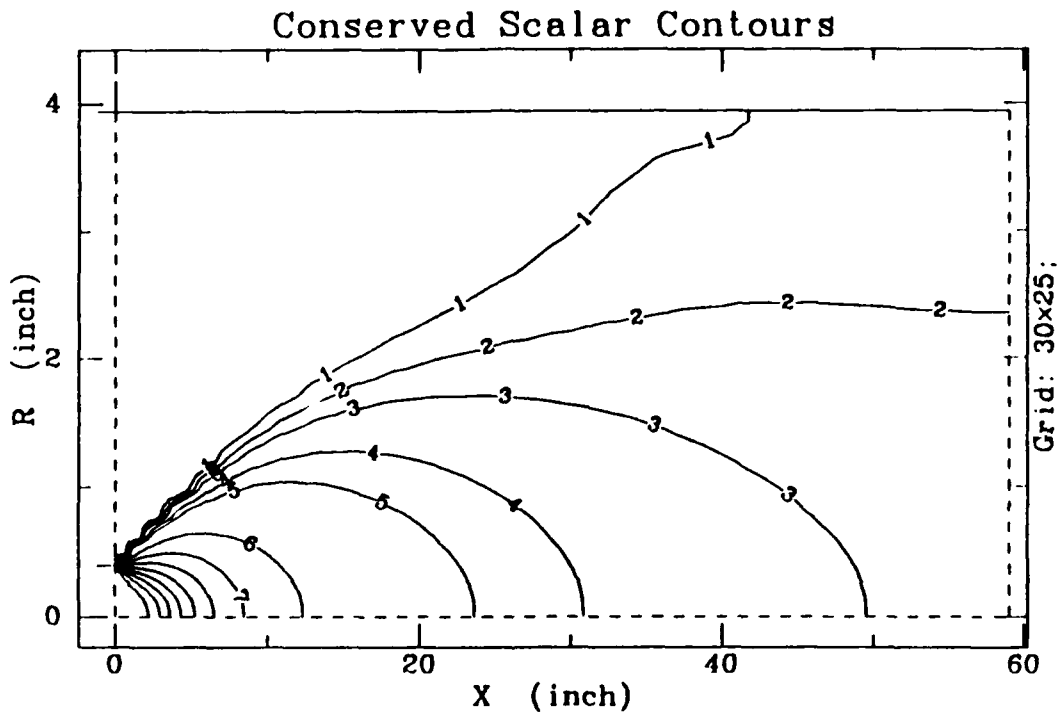
Figure 30: Grid distribution for the cold mixing problem.



Contour values: (Min. = 0.0000E+00 Max. = 0.1698E+02)

1:0.000E+00	2:0.250E+00	3:0.500E+00	4:0.750E+00	5:0.100E+01
6:0.150E+01	7:0.200E+01	8:0.300E+01	9:0.400E+01	10:0.500E+01
11:0.600E+01	12:0.700E+01	13:0.800E+01	14:0.900E+01	15:0.100E+02
16:0.110E+02	17:0.120E+02	18:0.130E+02	19:0.140E+02	20:0.150E+02
21:0.160E+02				

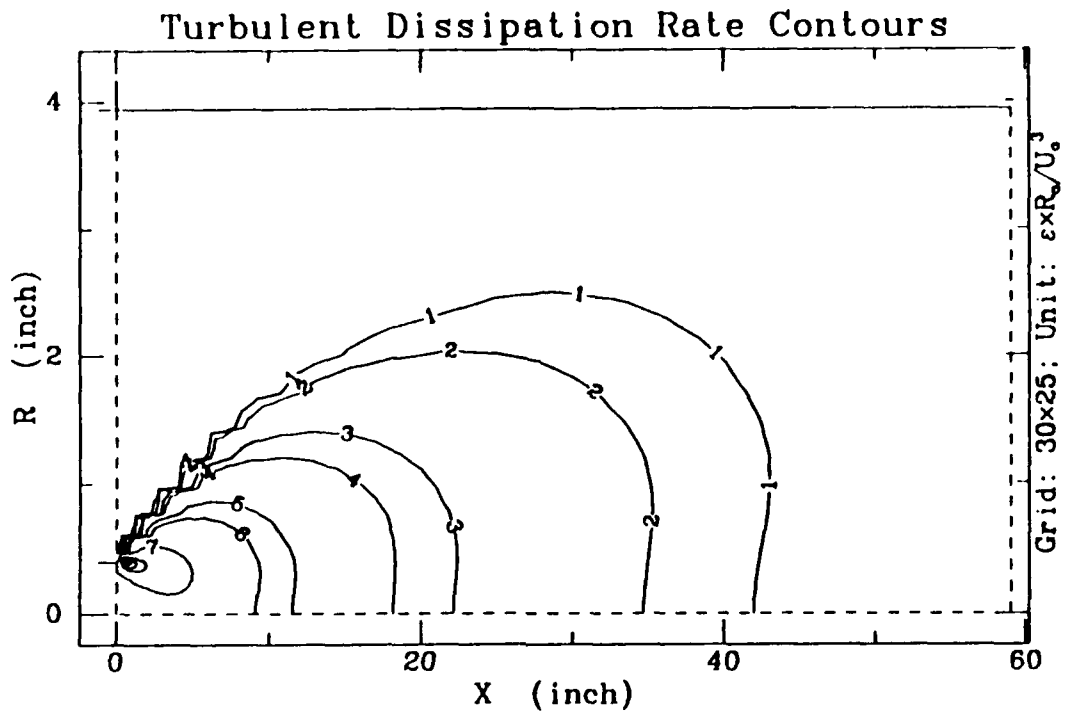
Figure 31: Streamfunction contours for the methane-air mixing problem



Contour values: (Min. = 0.0000E+00 Max. = 0.1000E+01)

1:0.250E-01	2:0.375E-01	3:0.500E-01	4:0.750E-01	5:0.100E+00
6:0.200E+00	7:0.300E+00	8:0.400E+00	9:0.500E+00	10:0.600E+00
11:0.700E+00	12:0.800E+00	13:0.900E+00		

Figure 32: Mixture fraction contours for the methane-air mixing problem.



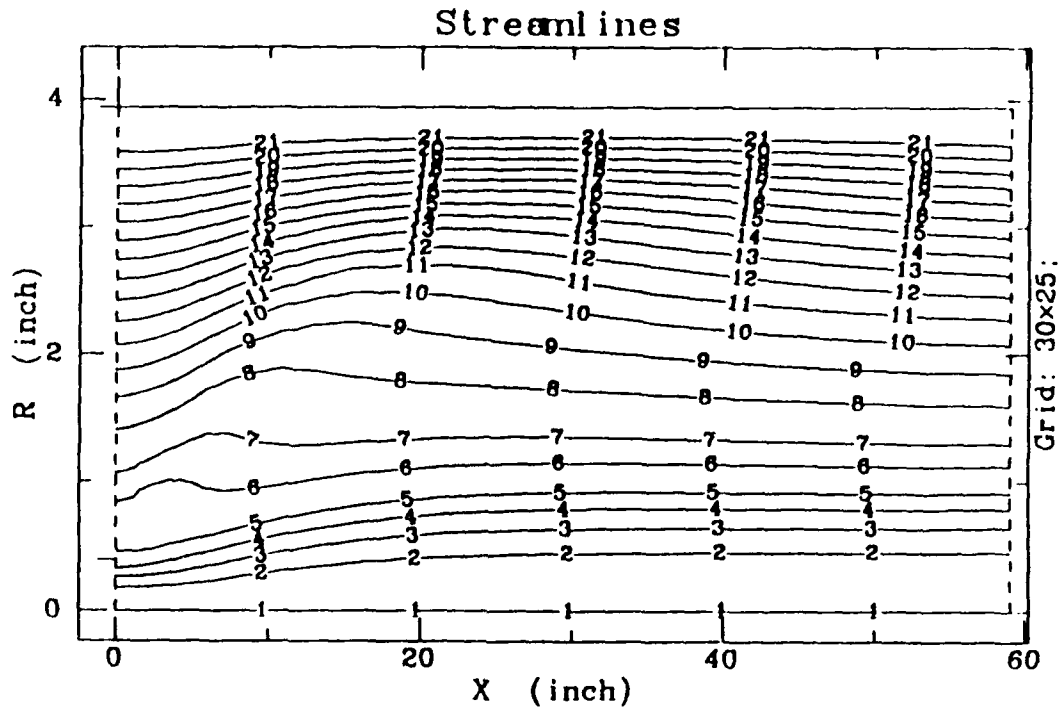
Contour values: (Min. = 0.8406E-03 Max. = 0.3004E+03)

1:0.500E-01 2:0.100E+00 3:0.500E+00 4:0.100E+01 5:0.500E+01

6:0.100E+02 7:0.500E+02 8:0.150E+03 9:0.200E+03 10:0.250E+03

11:0.300E+03

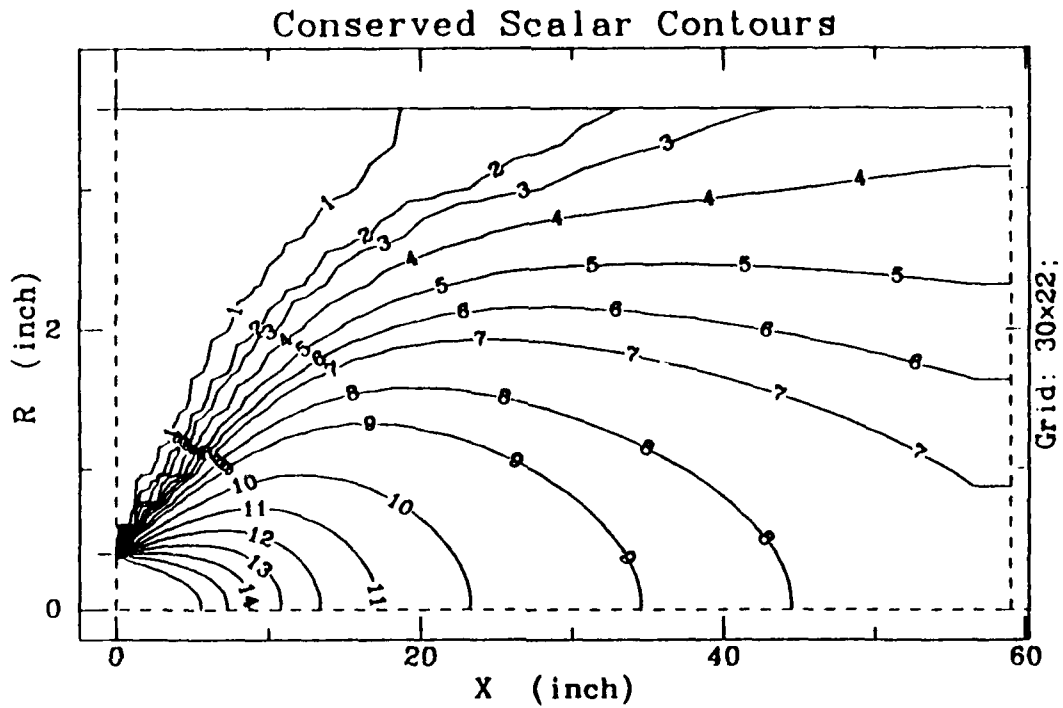
Figure 33: Turbulent kinetic energy dissipation rate contours for the methane-air mixing problem.



Contour values: (Min. = 0.0000E+00 Max. = 0.1823E+02)

1:0.000E+00	2:0.250E+00	3:0.500E+00	4:0.750E+00	5:0.100E+01
6:0.150E+01	7:0.200E+01	8:0.300E+01	9:0.400E+01	10:0.500E+01
11:0.600E+01	12:0.700E+01	13:0.800E+01	14:0.900E+01	15:0.100E+02
16:0.110E+02	17:0.120E+02	18:0.130E+02	19:0.140E+02	20:0.150E+02
21:0.160E+02				

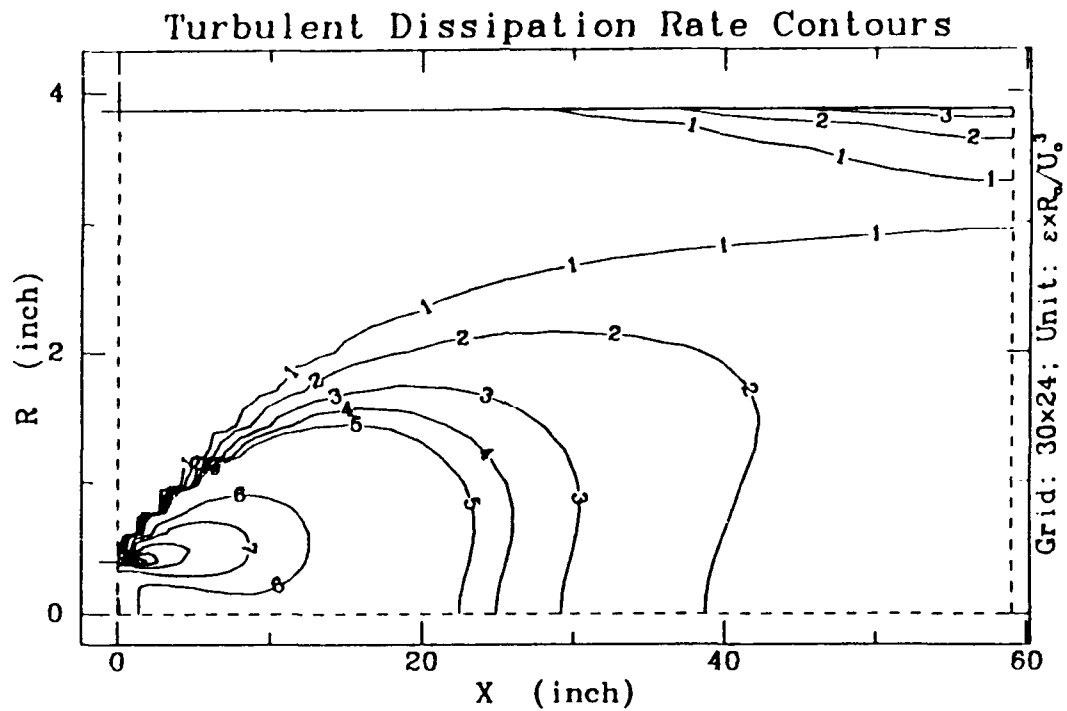
Figure 34: Streamfunction contours for the methane-air flame



Contour values: (Min. = 0.0000E+00 Max. = 0.1000E+01)

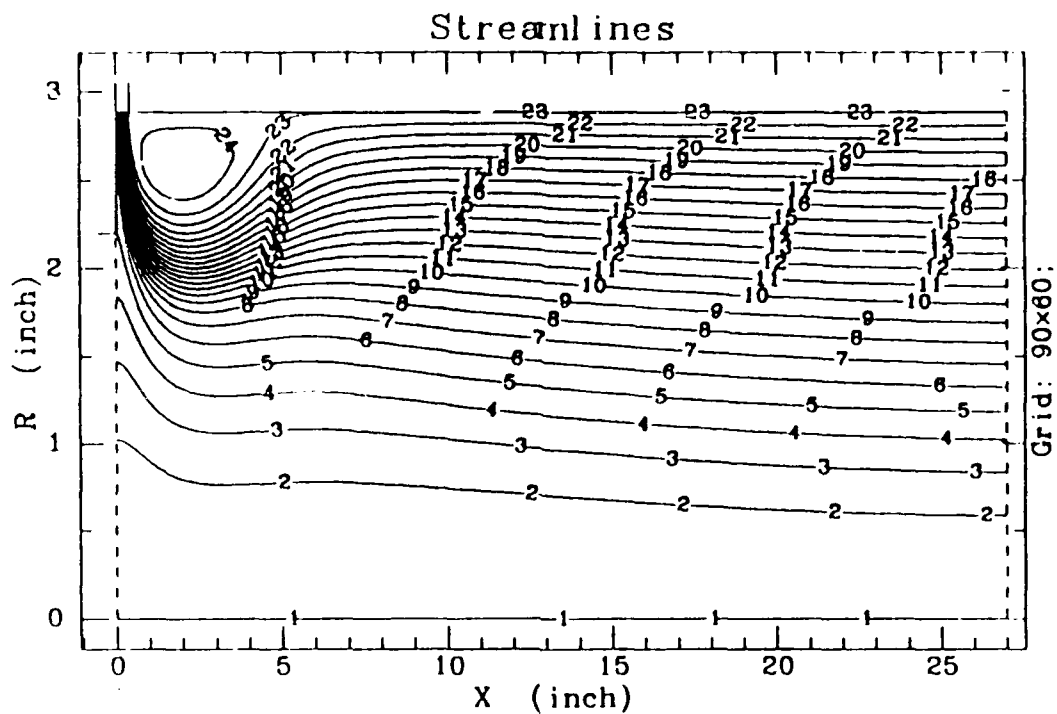
1:0.100E-02	2:0.500E-02	3:0.100E-01	4:0.250E-01	5:0.500E-01
6:0.750E-01	7:0.100E+00	8:0.150E+00	9:0.200E+00	10:0.300E+00
11:0.400E+00	12:0.500E+00	13:0.600E+00	14:0.700E+00	15:0.800E+00
16:0.900E+00				

Figure 35: Mixture fraction contours for the methane-air flame.



Contour values: (Min. = 0.4893E-05 Max. = 0.5812E+00)
 1:0.100E-02 2:0.250E-02 3:0.500E-02 4:0.750E-02 5:0.100E-01
 6:0.500E-01 7:0.100E+00 8:0.200E+00 9:0.300E+00 10:0.400E+00
 11:0.500E+00

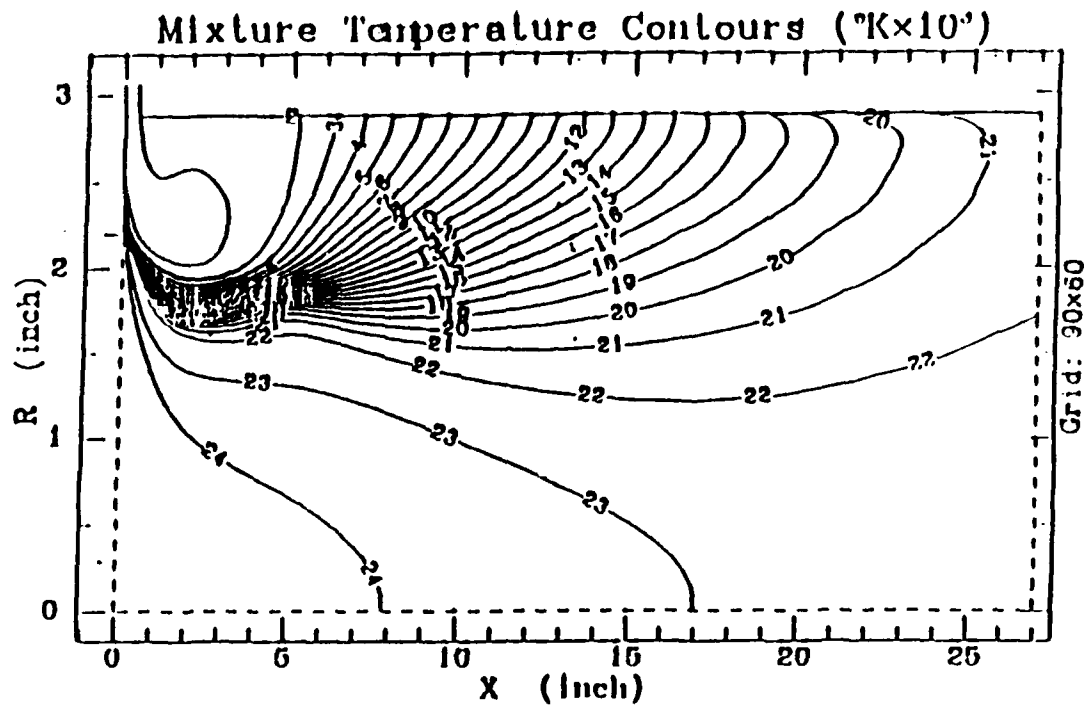
Figure 36: Turbulent kinetic energy dissipation rate contours for the methane-air flame.



Contour values: (Min. = 0.0000E+00 Max. = 0.5964E+01)

1:0.000E+00	2:0.250E+00	3:0.500E+00	4:0.750E+00	5:0.100E+01
6:0.125E+01	7:0.150E+01	8:0.175E+01	9:0.200E+01	10:0.225E+01
11:0.250E+01	12:0.275E+01	13:0.300E+01	14:0.325E+01	15:0.350E+01
16:0.375E+01	17:0.400E+01	18:0.425E+01	19:0.450E+01	20:0.475E+01
21:0.500E+01	22:0.525E+01	23:0.550E+01	24:0.575E+01	25:0.600E+01

Figure 37: Streamline contours for a custom AXIJET-T application with cross jets, and large density ratio, on a 90 by 60 grid.



Contour values: (Min. = 0.6091E+00 Max. = 0.1059E+01)

1: 0.700000	2: 0.750000	3: 0.800000	4: 0.850000	5: 0.900000
6: 0.950000	7: 1.000000	8: 1.050000	9: 1.100000	10: 1.150000
11: 1.200000	12: 1.250000	13: 1.300000	14: 1.350000	15: 1.400000
16: 1.450000	17: 1.500000	18: 1.550000	19: 1.600000	20: 1.650000
21: 1.700000	22: 1.750000	23: 1.790000	24: 1.850000	

Figure 38: Temperature contours for a custom AXIJET-T application with cross jets, and large density ratio, on a 90 by 60 grid.

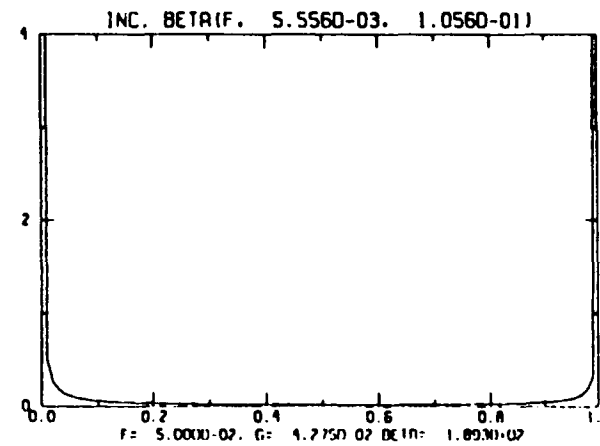
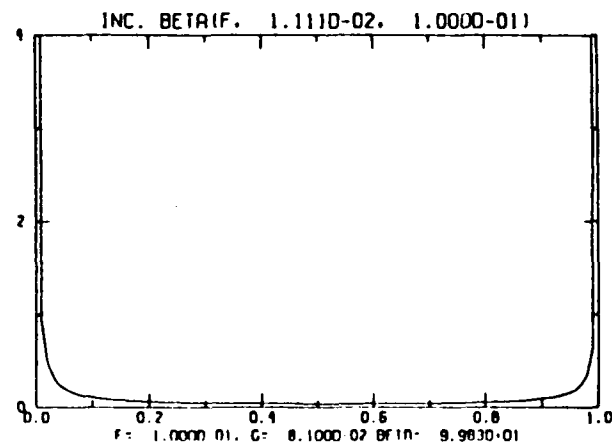
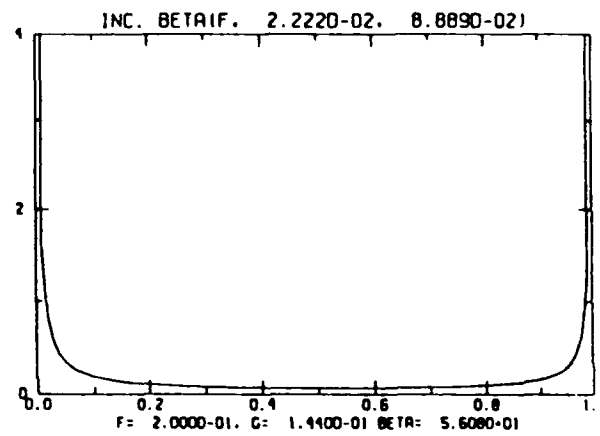
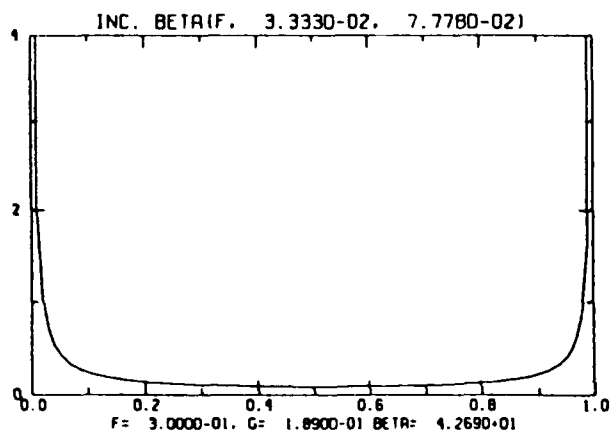
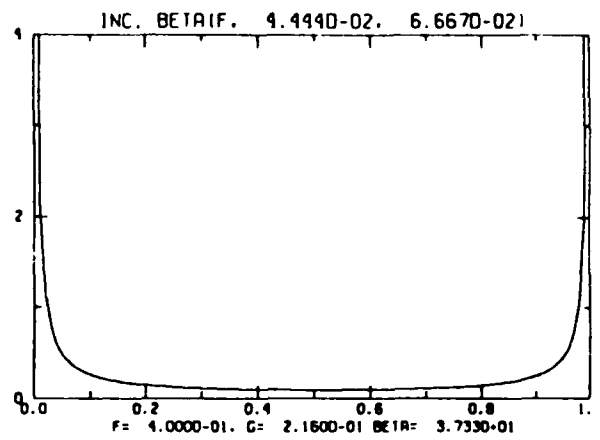
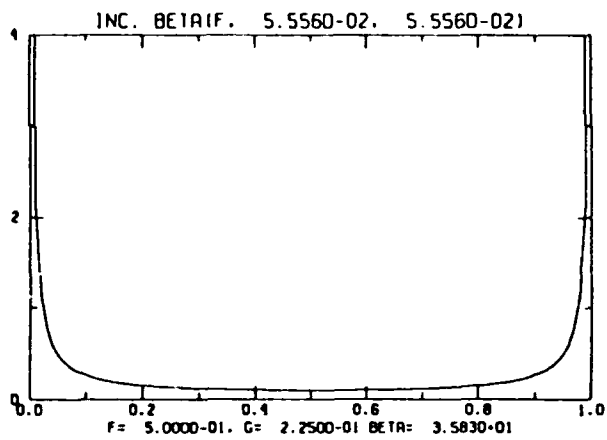


Figure 39: Sample beta function probability distributions at small mixture fraction covariance.

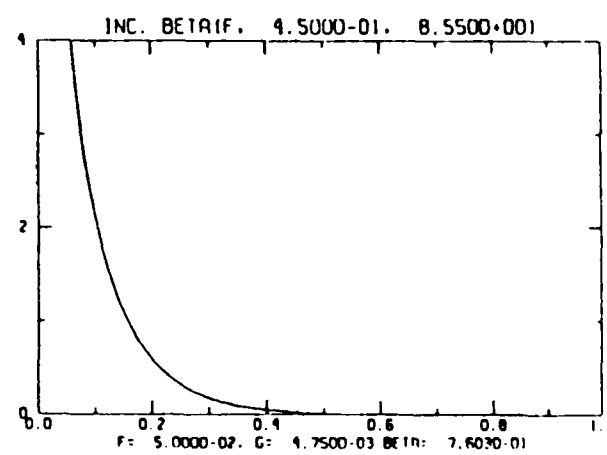
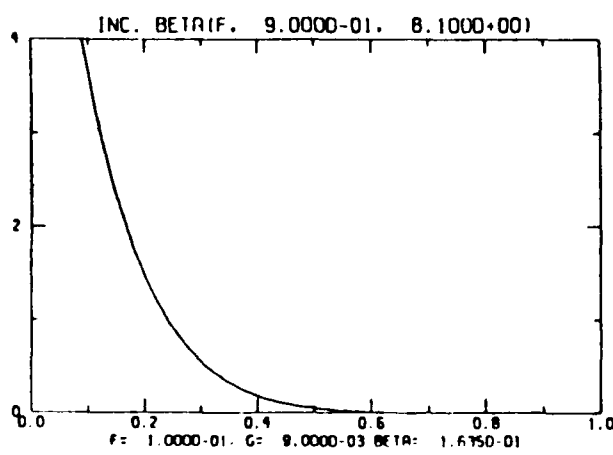
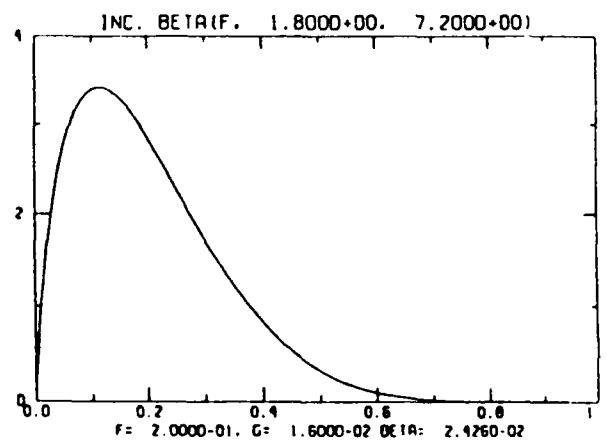
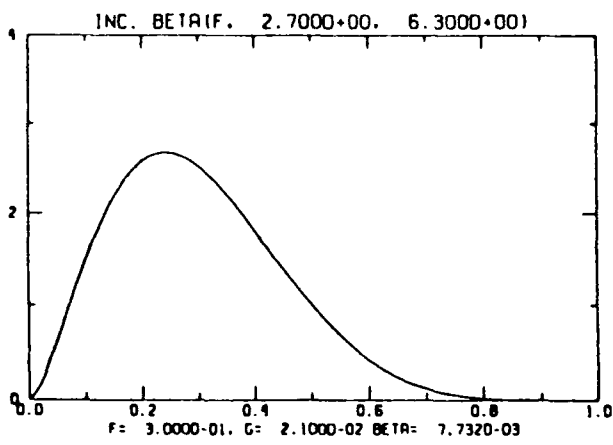
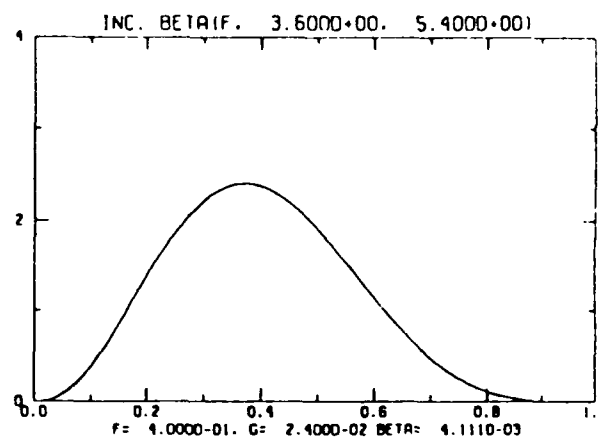
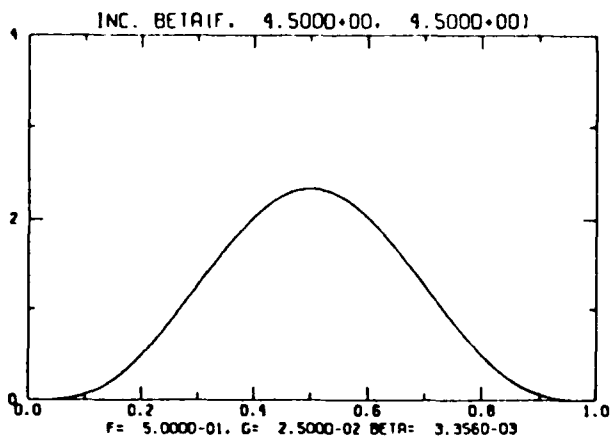


Figure 40: Sample beta function probability distributions at large mixture fraction covariance.

5.1. Introduction

In practical calculations of turbulent reacting flows, Favre-averaged values of the mixture properties are often evaluated through the introduction of a probability density function (pdf) for a single conserved scalar, f . The Favre average is a density-weighted time average of a fluctuating quantity, and is customarily denoted by means of a tilde to distinguish it from the overbar employed in ordinary time-averaging. For a fluctuating field ϕ ,

$$\tilde{\phi} \equiv \overline{\rho\phi}/\bar{\rho}. \quad (5.1)$$

The pdf $P(f, \mathbf{x})$ when multiplied by a differential df gives the probability finding the instantaneous value of the conserved scalar in a range df about f at the point \mathbf{x} . The total range of the conserved scalar is $0 < f < 1$. Thus, the Favre average of any quantity ϕ depending solely on f , such as a species concentration under an equilibrium kinetics assumption, for instance, is given at a point \mathbf{x} by

$$\tilde{\phi}(\mathbf{x}) = \int_0^1 \phi(f) P(f, \mathbf{x}) df. \quad (5.2)$$

In this expression $\phi(f)$ is the equilibrium value of the quantity ϕ corresponding to the instantaneous f .

The pdf $P(f, \mathbf{x})$ is assumed to embody all aspects of the local turbulent-chemistry interaction. Under the chemical equilibrium hypothesis, as well as under other hypotheses not illustrated herein, a useful conserved scalar is the mixture fraction, defined as

$$f = \frac{Z - Z_F}{Z_O - Z_F}, \quad (5.3)$$

where Z is any conserved function of the reaction (such as a stoichiometrically weighted linear combination of fuel and oxidant), and where subscripts F and O denote its values in the fuel and oxidant streams, respectively. The form of an incomplete beta function is often adopted for the pdf. Its form was given in equations (4.92) and (4.93).

The Favre averages \tilde{f} and \tilde{g} at the point \mathbf{x} are obtained by solving modeled partial differential equations of transport type as part of the main computational procedure, which often includes a $k - \epsilon$ turbulence model. The resulting formalism is sometimes referred to as the $k - \epsilon - g$ model. A thermochemical package is needed to provide $\phi(f)$ for each species concentration, viscosity, temperature, etc. Substitution of (4.92) into (5.2) gives

$$\bar{\phi} = \frac{1}{\beta(a, b)} \int_0^1 \phi(f) f^{a-1} (1-f)^{b-1} df, \quad (5.4)$$

where the complete beta function is defined by the definite integral

$$\beta(a, b) = \int_0^1 f^{a-1} (1-f)^{b-1} df.$$

The formula for the gas density is of a slightly different type since the time-averaged density is included in the Favre-averaged definition of all other fields. The appropriate relationship using the same pdf (4.92) is

$$(\bar{\rho})^{-1} = \frac{1}{\beta(a, b)} \int_0^1 (\rho(f))^{-1} f^{a-1} (1-f)^{b-1} df, \quad (5.5)$$

Equations (5.4) and (5.5) are both of the type

$$\bar{\phi} = \frac{\int_0^1 \phi(x) x^{a-1} (1-x)^{b-1} dx}{\int_0^1 x^{a-1} (1-x)^{b-1} dx}. \quad (5.6)$$

Since the variance g is constrained to lie in the interval $0 < g < \bar{f}(1-\bar{f})$, a and b are both greater than zero from (4.93), and thus the numerator and denominator of (5.6) are integrable for all physically reasonable ϕ . The results of the integration are best tabulated once for repeated "lookup" during the governing equations solution phase. A few considerations appropriate to this tabulation are:

- When a and b attain large values, numerical quadrature of the integrals in (5.6) can lead to underflow, since ϕ is bounded, and at least one factor of each integrand tends to zero in this limit. Even in the absence of underflow, a modestly large absolute error tolerance in the quadratures could result in an unacceptably inaccurate $\bar{\phi}$ being formed from the ratio.
- When a or b is less than one, the integrals become improper, since their integrands tend to infinity at at least one endpoint.
- An efficient arrangement of the table is needed to minimize the CPU time spent searching the table during the main computation.

We recommend in the next section an efficient and robust procedure for dealing with these potential problems.

5.2. Numerical Evaluation of Turbulent State Relations

In most cases of practical interest, the relationship $\phi(x)$ between the mixture property and the instantaneous conserved scalar is given in the form of tabulated data, that is, $\phi(x)$ is known only at a set of $n + 1$ points $\{x_i\}$, $0 = x_0 < x_1 < \dots < x_{n-1} < x_n = 1$, which partition the unit interval into n subintervals. On each subinterval, $\phi(x)$ may conveniently be approximated by a polynomial of degree k whose coefficients depend on the values $\phi(x_i)$ at some neighboring set of $k + 1$ indices. For piecewise linear interpolation in $x_{i-1} < x < x_i$,

$$\phi(x) = \phi(x_{i-1}) + \frac{x - x_{i-1}}{x_i - x_{i-1}} (\phi(x_i) - \phi(x_{i-1})),$$

or

$$\phi(x) = c_i x + d_i, \quad (5.7)$$

Only the piecewise linear case will be explicitly treated in the sequel; however, generalization to any finite-order polynomial can be straightforwardly accommodated in the following development by the inclusion of additional terms whose integrands contain higher powers of x . No cases requiring special treatment occur for powers beyond the zeroth and first.

Employing the interpolation (5.7) in the numerator of (5.6) gives

$$\begin{aligned} \int_0^1 \phi(x) x^{a-1} (1-x)^{b-1} dx &= \sum_{i=1}^n \left[c_i \int_{x_{i-1}}^{x_i} x^a (1-x)^{b-1} dx + d_i \int_{x_{i-1}}^{x_i} x^{a-1} (1-x)^{b-1} dx \right] \\ &= \sum_{i=1}^n [c_i (\beta(a+1, b, x_i) - \beta(a+1, b, x_{i-1})) + d_i (\beta(a, b, x_i) - \beta(a, b, x_{i-1}))], \end{aligned}$$

where

$$\beta(a, b, x) = \int_0^x x^{a-1} (1-x)^{b-1} dx$$

is the unnormalized incomplete beta function. (Note that in this triple-argument notation $\beta(a, b, 1)$ is simply the complete beta function.) The denominator of (5.6) can be handled in exactly the same manner, with $c_i = 0$ and $d_i = 1$ for $i = 1, \dots, n$.

Equation (5.6) can also be written as

$$\int_0^1 \phi(x) x^{a-1} (1-x)^{b-1} dx = \sum_{i=1}^n [c_i I_i + d_i J_i], \quad (5.8)$$

where

$$I_i = I(a + 1, b, x_i) - I(a + 1, b, x_{i-1}), \quad J_i = I(a, b, x_i) - I(a, b, x_{i-1}),$$

where, in turn,

$$I(a, b, x) = \frac{1}{\beta(a, b)} \int_0^x x^{a-1} (1-x)^{b-1} dx \quad (5.9)$$

is the standard notation for the normalized incomplete beta function.

Since the I_i and J_i are independent of $\phi(x)$, they may be calculated once at each (a, b) required in the state function tables. The state function tables for each field are then produced by summing over the appropriate set of c_i and d_i .

The quadratures can be done by either of two convenient methods. If accurate sub-routines for the evaluation of (5.9) are available, they may be employed directly. If not, adaptive quadrature using a Richardson-extrapolated Simpson's formula on successively refined meshes will work in subintervals 2 through $n - 1$. In the BETPDF program, this is embodied in the *FORTRAN* routine QSIMP.

As noted in the introduction section, there are two regimes of the exponential parameters of the beta function which demand special numerical treatment.

- The case of a and b sufficiently large to cause underflow occurs only if g is very small. Physically, this implies that the variances of the fluctuating state variables about their means is negligible. In this limit, the pdf $P(f)$ may be represented by a Dirac delta function centered at \bar{f} . Hence, $\tilde{\phi} = \phi(\bar{f})$ directly, and numerical integration is unnecessary.
- If either a or b is less than unity, the left- or right-most subintervals, respectively, require a preliminary integration by parts to remove the negative power of x^{a-1} or $(1-x)^{b-1}$, respectively. Thus, one obtains the special formulae:

$$J_1 = \frac{1}{a} (x_1)^a (1-x_1)^{b-1} + \frac{b-1}{a} \int_0^{x_1} x^a (1-x)^{b-2} dx, \quad \text{when } 0 < a < 1,$$

$$I_n = \frac{1}{b} (x_{n-1})^a (1-x_{n-1})^b + \frac{a}{b} \int_{x_{n-1}}^{x_n} x^{a-1} (1-x)^b dx, \quad \text{when } 0 < b < 1,$$

$$J_n = \frac{1}{b} (x_{n-1})^{a-1} (1-x_{n-1})^b + \frac{a-1}{b} \int_{x_{n-1}}^{x_n} x^{a-2} (1-x)^b dx \quad \text{when } 0 < b < 1.$$

(Note that no special formula is needed for J_1 regardless of the magnitude of a .)

- As further noted in the introduction, the state function routines will be called repetitively at each grid point at each iteration during the main computational procedure which solves the governing Favre-averaged partial differential equations. Thus, the table searches need to be very efficient in terms of operation count. The domain $0 < \tilde{f} < 1$, $0 < g < \tilde{f}(1 - \tilde{f})$ has a parabolic bounding arc. This implies that a tabulation of state data over a uniform tensor product mesh in the circumscribing rectangle of (\tilde{f}, g) -space, implemented as a two-dimensional FORTRAN array, is wasteful of points. Any other type of mesh requires an iterative search in g followed by a bilinear interpolation procedure in a nonrectangular region. However, the transformation to (\tilde{f}, η) coordinates, where

$$\eta = \frac{g}{\tilde{f}(1 - \tilde{f})}$$

and $0 < \tilde{f} < 1$, $0 < \eta < 1$ makes the state space a square. In terms of η ,

$$a = \tilde{f}\left(\frac{1}{\eta} - 1\right), \quad b = (1 - \tilde{f})\left(\frac{1}{\eta} - 1\right).$$

Tabulation of the state variables at (\tilde{f}_i, η_j) , where $\tilde{f}_i = i/N_f$, $i = 0, \dots, N_f$ and where $\eta_j = j/N_\eta$, $j = 0, \dots, N_\eta$ provides that $\phi(\tilde{f}, \eta)$ may be bilinearly interpolated in exactly eight scalar multiply-adds and one scalar division.

5.3. Example and Discussion

The calculation of the Favre-averaged viscosity and density in terms of \tilde{f} and η is presented as an example. The equilibrium data for density and viscosity is listed in Table II. Figures 23 and 24 display three-dimensional views of pdf-averaged density and viscosity on the (\tilde{f}, η) plane, respectively. ($\tilde{f} = 0$ corresponds to the oxidizer stream and $\tilde{f} = 1$ to the fuel.)

The striking features of these figures are the non-monotonic relationships between the state variables and the mixture fraction at small η and the asymptotic approach of the viscosity curve to a straight line between the fuel and oxidant reservoir values when $\eta \rightarrow 1$. The first feature is not necessarily characteristic of all fuel-oxidizer combinations and inlet temperatures. (Hydrocarbon-air mixtures are notorious for the nearly vertical tangents of the density at small values of f , where f passes through its stoichiometric value, and this fact needs to be taken into account in adaptively refining the resolution of discrete methods in such regions. Failure to do so will nullify the accuracy of any calculation in which density differences play a role.) The second (highly appropriate) feature is generic to all beta-function generated models, can be verified mathematically as follows.

In the limit of $\eta \rightarrow 1$, we may write $\eta = 1 - \epsilon$ and consider instead the limit $\epsilon \rightarrow 0$ (through positive values). From a Taylor expansion with second- and higher-order terms neglected, we then have $a \approx \eta\tilde{f}$ and $b \approx \eta(1 - \tilde{f})$. From the alternative integral definition of the complete beta function,

$$\beta(a, b) = \int_0^1 (1 + s)^{-a-b} (s^{a-1} + s^{b-1}) ds,$$

we easily obtain to leading order that $\beta(a, b) \approx 1/\epsilon$ in this limit. Thus, the denominator of (5.6) becomes unbounded. Let the numerator be written

$$\int_0^\delta \phi(x) x^{a-1} (1-x)^{b-1} dx + \int_\delta^{1-\delta} \phi(x) x^{a-1} (1-x)^{b-1} dx + \int_{1-\delta}^1 \phi(x) x^{a-1} (1-x)^{b-1} dx,$$

where δ is some fixed positive constant less than unity which is chosen sufficiently small that $\phi(x)$ can be represented to adequate accuracy by simply the constant term in its Taylor series about the extreme endpoints in the first and third integrals. (Since the rest of each integrand has delta function-like behavior at each endpoint as $\epsilon \rightarrow 0$, this is always possible.) Then the first and third terms of the numerator become, respectively,

$$\phi(0) \frac{\delta^{\epsilon \tilde{f}}}{\epsilon \tilde{f}} + \phi(1) \frac{\delta^{\epsilon(1-\tilde{f})}}{\epsilon(1-\tilde{f})}$$

The middle term of the numerator can be bounded independently of ϵ by

$$\left[\max_{x \in (\delta, 1-\delta)} \phi(x) \right] \frac{1-2\delta}{\delta^2}$$

Multiplying both numerator and denominator by ϵ and letting $\epsilon \rightarrow 0$ gives the result that

$$\tilde{\phi} \rightarrow \tilde{f} \phi(0) + (1 - \tilde{f}) \phi(1),$$

as was to be shown.

Evaluation of Favre-averaged properties of a turbulent reacting flowfield using a beta function formalism is mathematically straightforward but requires some care in implementation in finite precision arithmetic, especially considering the strong nonlinear couplings in which the state variables are involved in the system of governing equations. In the technique described above for the accurate evaluation of these properties, the improper integrals occurring in the beta function integrals are removed by partial integration before numerical quadrature is employed. All of the mixture properties can be evaluated from

one set of evaluations of the beta-function integrals. The searching of the data table is simplified by means of a transformation which makes the domain of the independent variables a square.

References

- [1] R.J. Kee, J.A. Miller and T.H. Jefferson, *CHEMKIN: A General-Purpose, Transportable, Fortran Chemical Kinetics Code Package*, Technical Report SAND80-8003, Sandia National Laboratories Report, 1980.
- [2] R.E. Mitchell, *Nitrogen Oxide Formation in Laminar Methane-Air Diffusion Flames*, Ph.D. Thesis, MIT, 1975.
- [3] C.F. Curtiss, J.O. Hirschfelder, *Transport Properties of Multicomponent Gas Mixtures*, J. Chem. Phys., 17 (1949), pp. 550.
- [4] J.O. Hirschfelder, C.F. Curtiss and R.B. Bird, *Molecular Theory of Gases and Liquids*, John Wiley and Sons, Inc., New York, 1954.
- [5] S. Mathur, P.K. Tondon and S.C. Saxena, *Thermal Conductivities of Binary, Ternary and Quaternary Mixtures of Rare Gases*, Mol. Phys., 12 (1967), pp. 567.
- [6] J. Warnatz, *Influence of Transport Models and Boundary Conditions on Flame Propagation*, *Numerical Methods in Flame Structure*, Friedr. Vieweg and Sohn, Wiesbaden, 1982.
- [7] J.G. Parker, *Rotational and Vibrational Relaxation in Diatomic Gases*, Phys. of Fluids, 2 (1959), pp. 449.
- [8] C.C. Brau and R.M. Jonkman, *Classical Theory of Rotational Relaxation in Diatomic Gases*, J. Chem. Phys., 52 (1970), pp. 447.
- [9] J.A. Miller, R.E. Mitchell, M.D. Smooke and R.J. Kee, *Toward a Comprehensive Chemical Kinetic Mechanism for the Oxidation of Acetylene: Comparison of Model Predictions with Results from Flame and Shock Tube Experiments*, *Nineteenth Symposium (International) on Combustion*, Reinhold, New York, 1982, pp. 181.
- [10] J.A. Miller, M.D. Smooke, R.M. Green and R.J. Kee, *Kinetic Modeling of the Oxidation of Ammonia in Flames*, Comb. Sci and Tech., 34 (1983), pp. 149.
- [11] M.D. Smooke, *Solution of Burner Stabilized Premixed Laminar Flames by Boundary Value Methods*, J. Comb. Phys., 48 (1982), pp. 72.
- [12] M.D. Smooke, J.A. Miller, R.J. Kee, *Determination of Adiabatic Flame Speeds by Boundary Value Methods*, Comb. Sci. and Tech., 34 (1983), pp. 79.
- [13] S.P. Burke and T.E.W. Schumann, *Diffusion Flames*, Industrial Engineering Chemistry, 29 (1928), pp. 998.
- [14] R.E. Mitchell, A.F. Sarofim, L.A. Clomburg, *Experimental and Numerical Investigation and Confined Laminar Diffusion Flames*, Comb. and Flame, 37 (1980), pp. 227.
- [15] M.D. Smooke, R.E. Mitchell and J.F. Grcar, *Numerical Solution of a Confined Laminar Diffusion Flame*, *Elliptic Problem Solvers II*, Academic Press, New York, 1984, pp. 557.

- [16] D.E. Keyes and M.D. Smooke, *Flame Sheet Starting Estimates for Counterflow Diffusion Flame Problems*, J. Comp. Phys., 73 (1987), pp. 267.
- [17] A.M. Kanury, *Combustion Phenomena*, Gordon and Breach, New York, 1982.
- [18] D.B. Spalding, *The Theory of Flame Phenomena with a Chain Reaction*, Phil. Trans. Roy. Soc. London, 249A (1956), pp. 1.
- [19] G.K. Adams and G.B. Cook, *The Effect of Pressure on the Mechanism and Speed of the Hydrazine Decomposition Flame*, Comb. and Flame, 4 (1960), pp. 9.
- [20] G. Dixon-Lewis, *Flame Structure and Flame Reaction Kinetics I, Solution of Conservation Equations and Application to Rich Hydrogen-Oxygen Flames*, Proc. Roy. Soc., London, 1967, pp. 298A,p.495.
- [21] G. Dixon-Lewis, *Kinetic Mechanism, Structure, and Properties of Premixed Flames in Hydrogen-Oxygen-Nitrogen Mixtures*, Phil. Trans. of the Royal Soc. London, 292 (1979), pp. 45.
- [22] D.B. Spalding, D.L. Stephenson and R.G. Taylor, *A Calculation Procedure for the Prediction of Laminar Flame Speeds*, Comb. and Flame, 17 (1971), pp. 55.
- [23] K.A. Wilde, *Boundary-Value Solutions of the One-Dimensional Laminar Flame Propagation Equations*, Comb. and Flame, 18 (1972), pp. 43.
- [24] L. Bledjian, *Computation of Time-Dependent Laminar Flame Structure*, Comb. and Flame, 20 (1973), pp. 5.
- [25] S.B. Margolis, *Time-Dependent Solution of a Premixed Laminar Flame*, J. Comp. Phys., 27 (1978), pp. 410.
- [26] J. Warnatz, *Calculation of the Structure of Laminar Flat Flames I - Flame Velocity of Freely Propagating Ozone Decomposition Flames*, Ber. Bunsenges. Phys. Chem., 82 (1978), pp. 193.
- [27] ———, *Calculation of the Structure of Laminar Flat Flames II - Flame Velocity of Structure of Freely Propagating Hydrogen-Oxygen and Hydrogen-Air-Flames*, Ber. Bunsenges. Phys. Chem., 82 (1978), pp. 643.
- [28] ———, *Calculation of the Structure of Laminar Flat Flames III - Structure of Burner-Stabilized Hydrogen-Oxygen and Hydrogen-Flourine Flames*, Ber. Bunsenges. Phys. Chem., 82 (1978), pp. 834.
- [29] C.K. Westbrook and F.L. Dryer, *A Comprehensive Mechanism for Methanol Oxidation*, Combust. Sci. and Tech., 20 (1979), pp. 125.
- [30] ———, *Prediction of Laminar Flame Properties of Methanol Air Mixtures*, Comb. and Flame, 37 (1980), pp. 171.
- [31] T.P. Coffee and J.M. Heimerl, *The Detailed Modeling of Premixed, Laminar Steady-State-Flames. I. Ozone*, Comb. and Flame, 39 (1980), pp. 301.
- [32] ———, *Transport Algorithms for Premixed, Laminar Steady-State-Flames*, Comb. and Flame, 43 (1981), pp. 273.
- [33] J.A. Miller, R.J. Kee, M.D. Smooke, J.F. Grcar, *The Computation of the Structure and Extinction Limit of a Methane-Air Stagnation Point Diffusion Flame*, Technical Report WSS/C1-84-10, Western States Section of the Combustion Institute, 1984.

- [34] M.D. Smooke, J.A. Miller, R.J. Kee, On the Use of Adaptive Grids in Numerically Calculating Adiabatic Flame Speeds, *Numerical Methods in Laminar Flame Propagation*, Friedr. Vieweg and Sohn, Wiesbaden, 1982.
- [35] M.D. Smooke, J.A. Miller and R.J. Kee, Solution of Premixed and Counterflow Diffusion Flame Problems by Adaptive Boundary Value Methods, *Numerical Boundary Value ODEs*, Birkhauser, Boston, 1985, pp. 303.
- [36] M.D. Smooke, I.K. Puri and K. Seshadri, A Comparison Between Numerical Calculations and Experimental Measurements of the Structure of a Counterflow Diffusion Flame Burning Diluted Methane in Diluted Air, *Twenty-First Symposium (International) on Combustion*, Reinhold, New York, 1986, pp. 1783.
- [37] W.A. Hahn and J.O.L. Wendt, NO_x Formation in Flat, Laminar, Opposed Jet Methane Diffusion Flames, *Eighteenth Symposium (International) on Combustion*, Reinhold, New York, 1981, pp. 121.
- [38] J. Sato and H. Tsuji, *Extinction of Premixed Flames in a Stagnation in a Stagnation Flow Considering General Lewis Number*, *Comb. Sci. and Tech.*, 33 (1983), pp. 193.
- [39] G. Dixon-Lewis, T. David, P.H. Haskell, S. Fukutani, H. Jinno, J.A. Miller, R.J. Kee, M.D. Smooke, N. Peters, E. Effelsberg, J. Warantz and F. Behrendt, Calculation of the Structure and Extinction Limit of a Methane-Air Counterflow Diffusion Flame in the Forward Stagnation Region of a Porous Cylinder, *Twentieth Symposium (International) on Combustion*, New York, 1982, pp. 1983.
- [40] V. Giovangigli and M.D. Smooke, *Extinction of Strained Premixed Laminar Flames with Complex Chemistry*, *Comb. Sci. and Tech.*, 53 (1987), pp. 23.
- [41] P. Dueflhard, *A Modified Newton Method for the Solution of Ill-Conditioned Systems of Nonlinear Equations with Application to Multiple Shooting*, *Numer. Math.*, 22 (1974), pp. 289.
- [42] A.R. Curtis, M.J. Powell and J.K. Reid, *On the Estimation of Sparse Jacobian Matrices*, *J. Inst. Math. Appl.*, 13 (1974), pp. 117.
- [43] G.N. Newsam and J.D. Ramsdell, *Estimation of Sparse Jacobian Matrices*, Technical Report TR-17-81, Harvard University Report, 1981.
- [44] T.F. Coleman and J.J. More, *Estimation of Sparse Jacobian Matrices and Graph Coloring Problems*, Technical Report ANL-81-39, Argonne National Laboratory Report, 1981.
- [45] J. Kautsky and N.K. Nichols, *Equidistributing Meshes with Constraints*, *SIAM J. Science and Stat. Comp.*, 1 (1980), pp. 499.
- [46] R.D. Russell, Mesh Selection Methods, B. Childs, et al. eds., in *Proceedings of the Conference for Working Codes for Boundary Value Problems in ODE's*, Springer-Verlag, New York, 1979.
- [47] M.D. Smooke, *On the Use of Adaptive Grids in Premixed Combustion*, *AIChE J.*, 32 (1986), pp. 1233.

- [48] M.D. Smooke and R.M.M. Mattheij, *On the Solution of Nonlinear Two-Point Boundary Value Problems On Successively Refined Grids*, Applied Num. Math, 1 (1985), pp. 463.
- [49] L.V. Kantorovich and G.P. Akilow, *Functional Analysis in Normed Spaces*, Pergamon Press, 1964.
- [50] M.D. Smooke, *An Error Estimate for the Modified Newton Method with Applications to the Solution of Nonlinear Two-Point Boundary Value Problems*, J. Opt. Theory and Appl., 39 (1983), pp. 489.
- [51] C.K. Westbrook and F.L. Dryer, *Chemical Kinetic Modeling of Hydrocarbon Combustion*, Prog. Energy Comb. Sci., 10 (1984), pp. 1.
- [52] J. Warnatz, *The Mechanism of High Temperature Combustion of Propane and Butane*, Comb. Sci. and Tech, 34 (1983), pp. 177.
- [53] A. Favre, *Problems of Hydrodynamics and Continuum Mechanics*, SIAM, Philadelphia, 1969.
- [54] D.E. Keyes and M.D. Smooke, *Flame Sheet Starting Estimates for Counterflow Diffusion Flame Problems*, J. Comp. Phys., 73 (1987), pp. 267-288.
- [55] S.V. Patankar, *Numerical Heat Transfer and Fluid Flow*, Hemisphere, McGraw-Hill, 1980.
- [56] C.J. Chen and H.C. Chen, *Finite-Analytic Numerical Solution for Unsteady Two-Dimensional Navier-Stokes Equations*, J. Comp. Phys., 53 (1984), pp. 210-226.
- [57] V.C. Patel and H.C. Chen, *Turbulent Wake of a Flat Plate*, AIAA J, 25 (1987), pp. 1078-1085.
- [58] S. C. Eisenstat, M. C. Gursky, M. H. Schultz, and A. H. Sherman, *Yale Sparse Matrix Package. II. The Nonsymmetric Codes*, Technical Report 114, Yale University Department of Computer Science, 1977.
- [59] S.P. Vanka, *Block-implicit Calculation of Study Turbulent Recirculating Flows*, J. Heat Mass Trans., 28 (1985), pp. 2093-2103.